Bio-Inspired Compressive Sensing based on Auditory Neural Circuits for Real-time Monitoring and Control of Civil Structures using Resource Constrained Sensor Networks

by

Courtney Ann Peckens

A dissertation submitted in partial fulfillment
of the requirements for the degree of
Doctor of Philosophy
(Civil Engineering)
in The University of Michigan
2014

Doctoral Committee:

Associate Professor Jerome P. Lynch, Chair
Associate Professor Victoria Booth
Professor Victor C. Li
Assistant Professor Jason P. McCormick

DEDICATIONS

To Adam, my life-long adventure buddy

ACKNOWLEDGEMENTS

First, I would like to thank my husband Adam whose continual love and support provided me with the motivation and drive to overcome all challenges that I have faced, as well as provides infinite inspiration for the future. I would also like to thank my parents, Greg and Jeanne, who taught me at an early age the value of hard work and commitment and who have continually supported me throughout my entire academic career. Furthermore, I would like to thank my in-laws, Lynn and Linda, who have cheered me on throughout the entire PhD process. Finally, I would like to thank my siblings who have always provided the perspective and humor that I needed when I needed it most.

I would also like to express my sincere gratitude to my advisor, Dr. Jerome Lynch, for his wisdom and guidance. Professor Lynch opened my eyes to the world of bio-inspired engineering and taught me to seek out non-traditional solutions to complex engineering problems. Professor Lynch's mentoring has helped mold me into the researcher and person that I am today and without him, I would not have been able to achieve this large milestone in my life.

Next, I would like to thank the fellow members of the Laboratory for Intelligent Structural Technology (LIST) who also have helped me to grow as a researcher. In particular, I would like to thank Mr. Sean O'Connor and Mr. Michael Kane who conquered many of the peaks and valleys of the PhD process alongside of me.

I would also like to thank the many individuals at the University of Michigan and at other academic institutions who have aided me in completing the research herein. First, I would like to thank my committee members, Dr. Victor Li (Civil and Environmental Engineering), Dr. Jason McCormick (Civil and Environmental Engineering), and Dr. Victoria Booth (Mathematics) for their valuable feedback and suggestions for my thesis.

I would also like to thank Dr. Jin-Song Pei for her insight on Artificial Neural Networks which aided in the development of the content of Chapter 2. Additionally, I would like to thank Dr. Chin-Hsiung Loh for supplying the data that was used for validation of the embedded Neural Networks in Chapter 2. I would also like to thank Dr. Gwanghee Heo (Konyang University) for his help with the shaking table tests presented in Chapter 4.

Finally, I would like to acknowledge the financial support for this thesis. This thesis was funded through the generous support provided by the National Science Foundation (NSF) through grant numbers CCF-0910765 and CMMI-0846256, as well as the US Department of Commerce, National Institute of Standards and Technology (NIST) Technology Innovation Program (TIP) under Cooperative Agreement 70NANB9H9008. This research was also partially supported by the National Research Foundation of Korea Grant funded by the Korean Government (MEST) (NRF-2011-220-D00105 (2011068.0)).

TABLE OF CONTENTS

DEDICATIONS ..... **ii**

ACKNOWLEDGEMENTS ..... **iii**

LIST OF FIGURES ..... **viii**

LIST OF TABLES ..... **xiv**

ABSTRACT ..... **xvi**

CHAPTER 1. INTRODUCTION **1**

1.1. Motivation for Smart Structure Technology: Health Monitoring and Feedback Control of Civil Infrastructure **1**

1.1.1. Structural Health Monitoring *2*

1.1.2. Structural Control *3*

1.1.3. Limitations of Wired and Centralized Architectures *4*

1.2. Wireless Structural Monitoring and Control **5**

1.3. Bio-Inspired Engineering **8**

1.4. Signal Processing and Actuation in Biological Systems **11**

1.5. Artificial Neural Networks **14**

1.6. Research Objectives and Dissertation Outline **17**

CHAPTER 2. DISTRIBUTED NEURAL COMPUTATIONS IN WIRELESS SENSOR NETWORKS USING ARTIFICIAL NEURAL NETWORKS **21**

2.1. Introduction **21**

2.2. Volterra-Weiner Neural Networks (VWNN) **23**

2.3. Embedding the VWNN in a Wireless Sensor Network **29**

2.4. Experimental Validation 32

2.5. Chapter Summary 39

CHAPTER 3. UTILIZING THE COCHLEA AS A BIO-INSPIRED COMPRESSIVE SENSING TECHNIQUE 41

3.1. Introduction 41

3.2. Mechanisms of the Mammalian Cochlea 43

3.3. Representation of the Cochlea as an Engineered System 49

3.3.1. Customization of the Cochlea-Inspired Sensor System for Infrastructure Monitoring 54

3.4. Alternative Data Compression Techniques 60

3.4.1. Wavelet Compression 62

3.4.2. Compressive Sensing using Fourier Basis Functions 65

3.5. Results 67

3.6. Chapter Summary 73

CHAPTER 4. RESOURCE EFFICIENT WIRELESS SENSOR NETWORK ARCHITECTURE BASED ON BIO-MIMICRY OF SIGNAL PROCESSING IN THE CENTRAL NERVOUS SYSTEM 75

4.1. Introduction 75

4.2. Sensor Design 76

4.2.1. Base Board 79

4.2.2. Neuron Board 81

4.2.3. Radio Board 86

4.2.4. Summary of Hardware Design 87

4.3. Laboratory Study on Effects of Stochastic Communication 88

4.4. Experimental Validation with Seismic Monitoring Application 93

4.4.1. Monitoring Seismic Ground Motion 96

4.4.2. Monitoring Structural Response to Seismic Ground Motions 104

4.5. Chapter Summary 108

CHAPTER 5. REAL-TIME CONTROL OF CIVIL INFRASTRUCTURE USING WIRELESS SENSOR NETWORKS BASED ON BIO-MIMICRY OF THE BIOLOGICAL SENSORY SYSTEM 111

5.1. Introduction 111

5.2. Actuation in Biological Sensory Systems 113

5.3. Bio-Inspired Control of Civil Infrastructure using Cochlea-Inspired Sensor Node 115

5.3.1. Optimal Control Law for Bio-Inspired Control 116

5.4. Validation of Bio-Inspired Control 119

5.4.1. Experimental Test Bed 119

5.4.2. Integration with Cochlea-Inspired Sensor Node 122

5.4.3. Simulation Results 126

5.4.4. Energy Analysis 133

5.5. Chapter Summary 136

CHAPTER 6. CONCLUSIONS 138

6.1. Summary of Results 138

6.2. Contributions 141

6.3. Future Work 142

6.3.1. Short-Term Future Research 142

6.3.2. Long-Term Research Objectives 143

APPENDIX 145

REFERENCES 149

LIST OF FIGURES

Figure 1-1. Configuration of structural monitoring systems: tethered (a) versus wireless (b) (note: similar configurations exist for control applications), and schematic of components contained within a wireless sensor unit (c). 5

Figure 1-2. Schematic of neuron (a), single action potential (b), and synapse (c). 12

Figure 1-3. Utilization of biological processes for inspiration in addressing WSNs' current limitations. 15

Figure 1-4. McCulloch-Pitts perceptron. 16

Figure 1-5. Schematic representing the major topics covered in this dissertation. 18

Figure 2-1. Architecture of traditional neural network. Note that multiple hidden layers can be used. 24

Figure 2-2. VWNN architecture (adapted from Pei *et al.* (2005)). 26

Figure 2-3. Distribution of a six degree-of-freedom system's Volterra-Weinter neural network onto six wireless sensor nodes. Each floor utilizes a unique wireless sensor node termed WSU1 through 6 and dotted lines represent wireless communication. 30

Figure 2-4. *Narada* wireless sensor node with long-range radio board. 32

Figure 2-5. Six-story shear structure (a) and model (b) used for validating the embedded Volterra-Weiner neural network. 33

Figure 2-6. Parameter optimization based on RMS error for α (a), λ (b), and γ (c). 35

Figure 2-8. Absolute difference between neural network prediction and measured acceleration for both the training-on case and the training-off case when subject to the El Centro ground motion. 36

Figure 2-7. Response of six-story shear structure at each floor when subject to El Centro ground motion. 36

Figure 3-1. Diagram of the mammalian inner ear (a) and a cross-section of the cochlea (b). 44

Figure 3-2. Uncoiled cochlea indicating frequency response of the basilar membrane. . 45

Figure 3-3. Cross section of the Organ of Corti. 47

Figure 3-4. Information transmission through inner hair cell; in a stationary state (a) no information is transmitted but when motion activated (b), ionic fluid flows into the cell and releases transmitters to the across the auditory synapse which triggers a graded potential (c) and eventually a series of action potentials (d). 48

Figure 3-5. Schematic of cochlea-inspired sensor system. 53

Figure 3-6. Input signals used in time domain filter bank optimization. 54

Figure 3-7. Optimization plane (using total reconstruction error, *J*) for a filter bank with 11 filters (a), cross-section of plane at filter spacing equal to 0.7Hz (b), and cross-section of plane at filter bandwidth equal to 0.53Hz (c). 57

Figure 3-8. Optimization of number of filters based on reconstruction error and compression ratios (a) with associated optimal bandwidth (Hz) and filter spacing (Hz) (b) 58

Figure 3-9. Frequency response of optimal filter bank (14 filters with 0.53Hz bandwidth and 0.7Hz uniform spacing). 58

Figure 3-10. Frequency decomposition of El Centro earthquake using filter bank (14 filters with 0.53Hz bandwidth and 0.7Hz uniform spacing). 59

Figure 3-11. Cochlea-inspired data compression: peak picking (a), linear encoding (b) and data transmission at spike trains (c). 60

Figure 3-12. Signal reconstruction after passing through cochlea-inspired system for the El Centro earthquake, shown on a full time scale (a) and a sub-section of time (b), the Kobe earthquake, shown on a full time scale (c) and a sub-section of time (d), and the Northridge earthquake, shown on a full time scale (e) and a sub-section of time (f). 61

Figure 3-13. Vibratory input signals used in compression analysis. 62

Figure 3-14. Absolute difference between the input signal, El Centro earthquake, and each reconstructed signal in the full time domain (a) and a sub-section of the time domain (b). 68

Figure 3-15. Absolute difference between the input signal, El Centro earthquake, and each reconstructed signal in the full frequency domain (a) and a sub-section of the frequency domain (b). 69

Figure 3-16. Absolute difference between the input signal, a single degree of freedom structure subject to El Centro earthquake, and each reconstructed signal in the full time domain (a) and a sub-section of the time domain (b). 70

Figure 3-17. Absolute difference between the input signal, a single degree of freedom structure subject to El Centro earthquake, and each reconstructed signal in the full frequency domain (c) and a sub-section of the frequency domain (d). 71

Figure 3-18. The reconstruction capabilities of the filter bank, shown with respect to the filter *i* (characteristic frequency = ω_i) for an optimal filter bank (0.53Hz bandwidth, $\Delta\omega$ = 0.7Hz) (a) and a sub-optimal filter bank (0.20Hz bandwidth, $\Delta\omega$ = 0.7Hz) (b). The input signals include a sweep of various structural responses (natural frequency = ω_n) when subject to El Centro earthquake ground motion, where ω_n varied from 0 to 10.5Hz in 0.02Hz increments. 72

Figure 4-1. Simplified schematic of the mammalian auditory process (a) compared with the process of the proposed wireless sensor system which utilizes a band-pass filter (BPF) bank and microcontrollers to emulate the function of the cochlea's basilar membrane and neurons, respectively (b)..... 77

Figure 4-2. Cochlea-inspired wireless sensor node with a radio board, multiple neuron boards, and base board (a), schematic of complete sensing node with "*n*" neuron boards (b) and functional schematic of a typical neuron board (c)..... 78

Figure 4-3. Circuit prototype of baseboard (a), neuron board (b), Texas Instruments' CC2520 radio board on radio interface board (c), and radio interface board (d). 80

Figure 4-4. Fliege band-pass filter topology. 82

Figure 4-5. Example of encoding process for 1 Hz filter output. 84

Figure 4-6. Packet structure used in wireless data transmission. 85

Figure 4-7. Three input signals used to determine characteristics of stochastic communication in time (a) and frequency (b) domains. 88

Figure 4-8. Probability density function (PDF) of percentage of skipped packets for wideband-seismic (a), narrowband-seismic (b), and broadband-white (c) signals. 90

Figure 4-9. Average percentage of skipped points (a) and reconstruction error (b) as the number of filter boards increases in the wireless sensor node for a wideband-seismic signal (El Centro earthquake), a narrowband-seismic signal (filtered El Centro earthquake), and a broadband-white signal (random noise). 91

Figure 4-10. Single span bridge used for validation of wireless sensor (a), cochlea-inspired wireless sensor node on test-bed (b), side view schematic of bridge with instrumentation (c), front view schematic of bridge (d), and frequency response function of single-span bridge when subject to random excitation (e). 94

Figure 4-11. Seismic signals used as input in optimization of wireless sensor node on test-bed in time (a) and frequency (b) domains. 96

Figure 4-12. Effect of number of neuron boards on reconstruction error (a), the relation of the reconstruction error to the energy density of the signal (b), and the compression ratio (c) when monitoring three seismic ground motions. Results are based on neuron boards spaced at 0.5Hz with bandwidth of 0.35Hz. 98

Figure 4-13. Effect of filter spacing on reconstruction error (a) and compression ratio (b) when monitoring three seismic ground motions. Bandwidth varies as a scaled function of the filter spacing and the number of boards is varied to ensure that the maximum band-pass center frequency is approximately 6Hz. 100

Figure 4-14. Effect of filter bandwidth on reconstruction error (a) and compression ratio (b) when monitoring three seismic ground motions. Filter spacing is held constant at 0.7Hz and number of filter boards is 9. 101

Figure 4-15. Signal reconstruction of El Centro ground acceleration using cochlea-inspired sensor in the full time-domain (a), a sub-scale in the time-domain (b), a full-scale in the frequency domain (c), and a sub-scale in the frequency domain (d). 102

Figure 4-16. Effect of number of neuron boards on reconstruction error (a) and the compression ratio (c) when monitoring a structure's response to three seismic ground motions. Results are based on neuron boards spaced at 0.5Hz with bandwidth of 0.35Hz. 105

Figure 4-17. Effect of filter spacing on reconstruction error (a) and compression ratio (b) when monitoring a structure's response to three seismic ground motions. Bandwidth varies as a scaled function of the filter spacing and the number of boards is varied to ensure that the maximum band-pass center frequency is approximately 6Hz. 106

Figure 4-18. Effect of filter bandwidth on reconstruction error (a) and compression ratio (b) when monitoring a structure's response to three seismic ground motions. Filter spacing is held constant at 0.7Hz and number of filter boards is 9. 107

Figure 4-19. Signal reconstruction of El Centro ground acceleration using cochlea-inspired wireless sensor in the full time-domain (a), a sub-scale in the time-domain (b), a full-scale in the frequency domain (c), and a sub-scale in the frequency domain (d). 108

Figure 5-1. Complete sensing and actuation process in biological sensory systems. ... 113

Figure 5-2. Complete sensing and actuation process in bio-inspired sensory system. . 115

Figure 5-3. Four story test bed that is attached to shake table and MB dynamics modal shaker (a) and test structure schematic front view (b) and side view (c). 120

Figure 5-4. Frequency response functions (FRF) of four story structure where the input signal is frequency sweep ground motion and the output is the inter-story displacement of each floor. 121

Figure 5-5. Cochlea-inspired wireless sensor node on test bed. 122

Figure 5-6. *Martlet* - wireless sensor node used as motor neuron in bio-inspired control (a) and DC motor controller interface board (b). 123

Figure 5-7. Reconstruction error in time, e_T, and frequency domains, e_F, as a function of the number of filter boards in a single sensing node. 124

Figure 5-8. Interpolation between peak values for bio-inspired control for 1Hz filter board. 128

Figure 5-9. Various control options for the bio-inspired control algorithm. Note that BC is the continuous filtered case, PP is the peaking picking case, PI is the peak-picking plus interpolation case, PZ is the peak-picking plus zero-crossing case and PZI is the peak-picking plus zero-crossing plus interpolation case. 129

Figure 5-10. Controlled to uncontrolled ratios for the El Centro earthquake (±0.5g) simulation results when considering maximum inter-story displacement ($\boldsymbol{J}_{c1}$), norm of inter-story displacement ($\boldsymbol{J}_{c2}$), maximum acceleration ($\boldsymbol{J}_{c3}$), and norm of acceleration ($\boldsymbol{J}_{c4}$) for the traditional LQR controller and five bio-inspired control algorithms (BC, PP, PZ, PZI and PI). 130

Figure 5-11. Controlled to uncontrolled ratios for the Kobe earthquake (±0.4g) simulation results when considering maximum inter-story displacement ($\boldsymbol{J}_{c1}$), norm of inter-story displacement ($\boldsymbol{J}_{c2}$), maximum acceleration ($\boldsymbol{J}_{c3}$), and norm of acceleration ($\boldsymbol{J}_{c4}$) for the traditional LQR controller and five bio-inspired control algorithms (BC, PP, PZ, PZI and PI). 131

Figure 5-12. Optimal synaptic strengths between each filter board on each floor and the centralized motor neuron unit which control actuator 1 and actuator 2. Note that '*CIS X*' depicts the filter boards associated with the cochlea-inspired sensing node that is located on the floor *X*. 134

Figure 5-13. Effect of pruning synaptic connections between the cochlea-inspired sensing node and the motor neuron node for the El Centro earthquake. 135

Figure 5-14. Effect of pruning synaptic connections between the cochlea-inspired sensing node and the motor neuron node for the Kobe earthquake. 135

LIST OF TABLES

Table 1-1. Summary of capabilities and deficiencies of biological sensing systems. 14

Table 2-1. Centralized versus decentralized time consumption for one iteration of the algorithm. 37

Table 2-2. Breakdown of time consumption of decentralized VWNN tasks for one iteration during "Training-On" mode. 37

Table 3-1. Comparison between biological sensory system and engineered sensor system. 50

Table 3-2. Reconstruction error and compression rates for the optimal number of filters, 14 filters. 59

Table 3-3. Comparison of cochlea-inspired sensor system to traditional compressive techniques. 67

Table 4-1. Signals transmitted through bus connections. 79

Table 4-2. Power consumption and cost of each board. *X* is an arbitrary number of Neuron Boards that linearly scales the total cost and power consumption. 87

Table 4-3. Cumulative spectral energy density, $E_s(f)$, for variable number of filters and three earthquake signals: El Centro earthquake (*EC*), Kobe earthquake (*K*), and Northridge earthquake (*NR*). 99

Table 4-4. Comparison of the effect of input signal amplitude when monitoring seismic ground motion. Note that the power ratio is the power consumed by the cochlea-inspired sensing node divided by the power consumed by the respective traditional sensing node. 104

Table 4-5. Comparison of the effect of input signal amplitude when monitoring structural response to seismic ground motion. Note that the power ratio is the power consumed by the cochlea-inspired sensing node divided by the power consumed by the respective traditional sensing node. 109

Table 5-1. Comparison of the control capabilities when using the traditional LQR algorithm and the bio-inspired control algorithm for both the El Centro and Kobe earthquakes and a constrained actuator..... 132

Table 5-2. Comparison of the control capabilities when using the traditional LQR algorithm and the bio-inspired control algorithm for both the El Centro and Kobe earthquakes and an unconstrained actuator..... 132

ABSTRACT

Bio-Inspired Compressive Sensing based on Auditory Neural Circuits for Real-time Monitoring and Control of Civil Structures using Resource Constrained Sensor Networks

by

Courtney Ann Peckens

Chair: Jerome P. Lynch

Recent natural hazard disasters including Hurricane Sandy (2012) and the Tohoku Earthquake (2011) have called public attention to the vulnerability of civil infrastructure systems. To enhance the resiliency of urban communities, arrays of wireless sensors and actuators have been proposed to monitor and control infrastructure systems in order to limit damage, speed emergency response, and make post-disaster decisions more efficiently. While great advances in the use of wireless sensor networks (WSNs) for the purposes of monitoring and control of civil infrastructure have been made, significant technological barriers have hindered their ability to be reliably used in the field for long durations. Some of these limitations include: reliance on finite, portable power supplies, limited radio bandwidth for data communication, and limited computational capacity. To resolve current bottlenecks, paradigm-altering approaches to the design of wireless monitoring and control systems are required. Through the process of evolution, biological central nervous systems (CNS) have evolved into highly adaptive and robust systems whose sensing and actuation capabilities far surpass the current capabilities of engineered (*i.e.*, man-made) monitoring and control systems. In this dissertation, the mechanisms employed by biological sensory systems serve as sources of inspiration for overcoming

the current challenges faced by wireless nodes for structural monitoring and control. The basic, yet elegant, methods of signal processing and data transmission used by the CNS are mimicked in this thesis to enable highly compressed communication with real-time data processing for WSNs engaged in infrastructure monitoring. Specifically, the parallelized time-frequency decomposition of the mammalian cochlea is studied, modeled, and recreated in an ultra-low power analog circuit. In lieu of transmitting data, the cochlea-inspired wireless sensors emulate the neurons by encoding filtered outputs into binary electrical spike trains for highly efficient wireless transmission. These transmitted spike train signals are processed for pattern classification of sensor data to identify structural damage and to perform feedback control in real-time. A key contribution of this thesis is the development and experimental validation of a bio-inspired wireless sensor node that exhibits large energy savings while employing real-time processing techniques, thus overcoming many of the current challenges of traditional wireless sensor nodes.

CHAPTER 1

INTRODUCTION

1.1. Motivation for Smart Structure Technology: Health Monitoring and Feedback Control of Civil Infrastructure

Critical infrastructure systems (*e.g.*, bridges, pipelines, roads, buildings) are vital to the economic success of modern society. However, such structures are susceptible to degradation and deterioration due to aging effects, harsh environments, or extreme loading scenarios, such as earthquakes or high wind loads. Additionally, due to extensive daily use over decades of service, the condition of many infrastructure systems in developed nations like the United States is poor. In a bi-annual review of the United States' infrastructure, the American Society of Civil Engineers reported an average grade of a D+ for all infrastructure (*e.g.*, bridges, dams, drinking water) resulting in infrastructure being assigned to the "at risk" category (ASCE 2013). In particular, it was reported that one in nine bridges are structurally deficient and the average age of bridges in the nation is 42 years old which is rapidly approaching the traditional design life of 50 years for existing bridges (FHWA 2011). Current federal law mandates that many infrastructure systems undergo visual inspections on a regular basis to ensure that they are safe for use. For example, bridges are required to undergo bi-annual inspections at a minimum. Unfortunately, visual inspections can be subjective in nature, time-consuming, costly, and insufficient as the majority of structural defects often lie beneath the surface of the structure (Moore *et al.* 2001). Therefore, alternative methods of accurately assessing a structure's integrity, and in some cases controlling its response, are needed. In particular, structural health monitoring (SHM) has received attention because

it uses sensor data to autonomously and quantitatively track changes in a structure's inherent characteristics, thereby allowing for continuous assessment of structural integrity (Chang *et al.* 2003; Sohn *et al.* 2003; Farrar and Worden 2007; Farrar and Worden 2012). Structural control, on the other hand, involves modifying structural properties such as stiffness or damping through the application of passive or active forces (Housner *et al.* 1997; Spencer and Nagarajaiah 2003), in order to mitigate the negative effects of large extraneous loads (*e.g.* earthquakes, typhoons). Similar to SHM, structural control relies on sensors to measure structural behavior under loading. However, structural control systems also utilize controllers and actuators to calculate and apply control forces. Both SHM and control systems fundamentally rely upon sensing, computing, and actuation technologies to protect structures (and ultimately the public) from long-term deterioration and extreme loads.

1.1.1. Structural Health Monitoring

The majority of today's civil infrastructure relies on traditional structural assessment techniques, such as visual inspections or simple tool-based inspections (*e.g.*, hammer tapping). However, recent structural failures such as the roof collapse at the Charles de Gaulle airport (Reina 2004), the I-70 overpass collapse in Pennsylvania (Harries 2009), and the San Bruno pipeline explosion (NTSB 2010) have called public attention to the problem of deteriorating infrastructure systems. These unfortunate events, and others like them, have served as motivation for the development of more refined SHM techniques. To supplement traditional visual inspection methods, non-destructive testing (NDT) techniques and permanent structural monitoring systems have become increasingly popular as a means of generating quantitative data related to structural performance that can be used to detect damage earlier, especially well before structural failure or collapse. Permanent monitoring systems entail the installation of accelerometers, strain gauges, potentiometers, *etc*. to record responses of the structural system. More recently, NDT-based sensing techniques such as guided waves (Raghavan and Cesnik 2007) have been included in permanent monitoring systems. Using both global and local responses, damage detection algorithms based on physical models

(Doebling *et al.* 1998) and statistical pattern recognition (Farrar and Worden 2012) are used. While significant advancement has been made in this area, few commercial applications of automated damage detection can be found for civil engineering structures. Regardless of this fact, many civil infrastructure have begun to be equipped with permanent sensing systems that enable continual monitoring of the structure's response (Brownjohn 2007). Owners electing to install structural monitoring systems do so to better understand their structures or use monitoring data to make decisions about whether a structure can be safely used or not (*e.g.*, long-span bridge owners track responses during strong wind events to decide if a bridge can remain open for use). However, it is their long-term goal to also use the data collected to make more efficient decisions regarding maintenance over a structure's complete life cycle. Due to their high importance to society, a particular emphasis has been placed on long-span bridges with several monitoring systems now installed on suspension and cable-stay bridges across the world (Fujino *et al.* 2000; Wong *et al.* 2000; Ko and Ni 2005; Park *et al.* 2010; Kurata *et al.* 2013). This enables tracking of the response of the bridge during both normal daily operation, as well as during time-critical events such as earthquakes and typhoons.

1.1.2. Structural Control

While monitoring a system's structural response to extreme load events is beneficial there has been a heightened interest in designing systems that are capable of also mitigating undesired responses (Constantinou *et al.* 1998). Traditionally, a designer mitigates a structure's response to such events by passively increasing its strength and ductility, thereby utilizing internal properties of the structure to build in more capacity (Symans and Constantinou 1999). However, for buildings in particular it has been found that in order to ensure adequate comfort and safety levels for the occupants, alternative methods should be utilized to reduce the effects of large external loads. Structural control was first introduced in the early 1960's in the form of base isolation and later in the form of active and semi-active actuation; since this time, it has evolved into a mature field through decades of research and experience (Chu *et al.* 2005). The overarching objective of structural control is to mitigate the destructive effects of external loads, such

as wind or seismic loads, by either applying counter-acting forces (as in the case of active control) or by developing internal reactionary forces through modification of structural conditions (as is the case in semi-active control). To achieve this, the system relies on real-time feedback of the structure's response (*e.g.*, displacement, velocity, acceleration), properly sized actuators, and controllers that calculate control actions in real-time for application by actuators. The vast amount of research conducted in this area over the last several decades has resulted in the successful implementation of control systems in many real-world structures (Spencer and Sain 1997; Spencer and Nagarajaiah 2003). The majority of these systems have been installed to enhance occupant comfort in buildings during strong wind events. However, semi-active control systems have been more recently implemented to reduce damage during seismic events. Of these successful implementations, however, relatively few include applications in the United States largely due to perceived issues surrounding the technology's cost effectiveness, reliability, and power requirements (Spencer *et al.* 1998).

1.1.3. Limitations of Wired and Centralized Architectures

The functionality of SHM and control systems both rely on the successful integration of information between sensors and/or controllers. Such systems depend on a data acquisition (DAQ) system that collects and stores information from the sensors in a centralized location. Traditionally, data is transmitted from these sensors through wired means (*e.g.*, coaxial cables) as shown in Figure 1-1a While extremely reliable in communication, wires require significant installation time and often cost several thousand dollars per sensing node channel to install (Celebi 2002) making installations of large networks of sensors unattractive. As a result, tethered systems typically lack a high spatial density of sensors within their networks. Low sensor densities are especially limiting for SHM at it becomes difficult to detect localized damage. Furthermore, for control systems that are operating on a centralized server, data must be processed from all sensors prior to making a control decision. While computing power is continuously improving, integration of many sensing channels to calculate control actions at a single controller remains challenging for real-time operation.

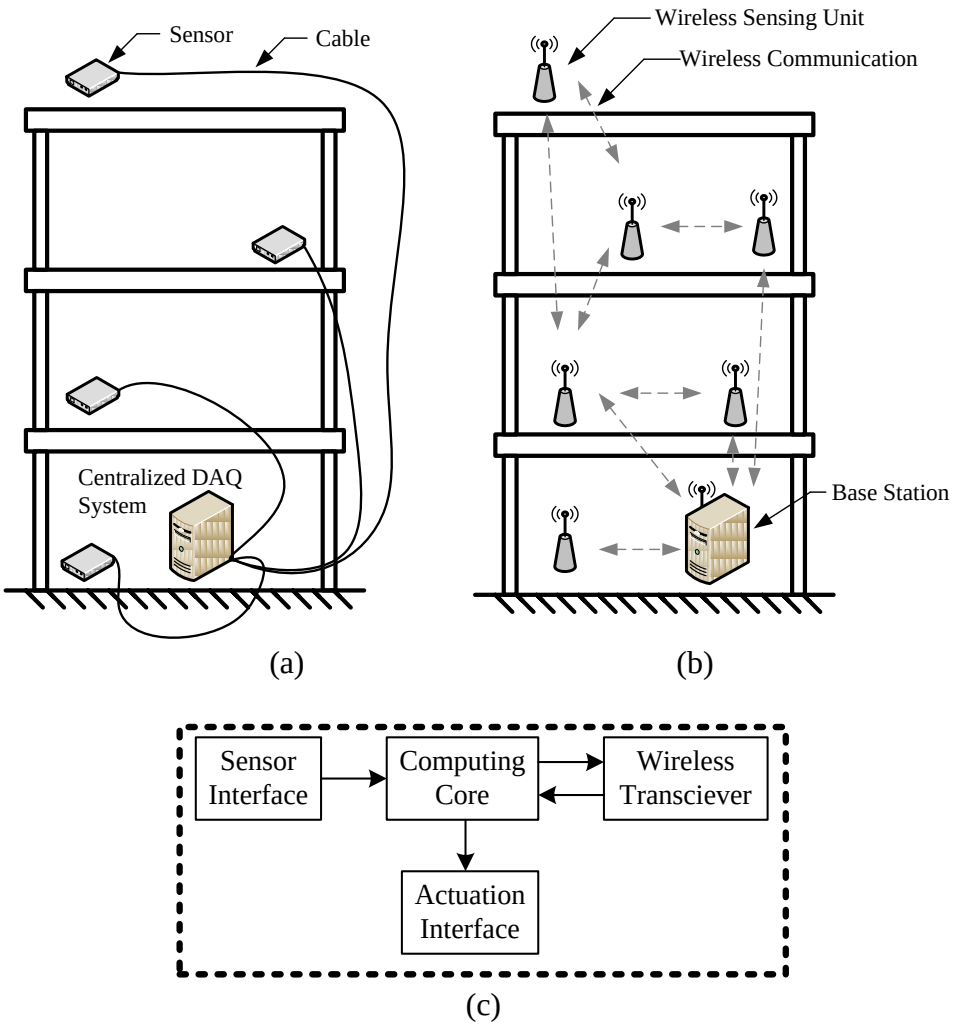

Figure 1-1. Configuration of structural monitoring systems: tethered (a) versus wireless (b) (note: similar configurations exist for control applications), and schematic of components contained within a wireless sensor unit (c).

1.2. Wireless Structural Monitoring and Control

To address the limitations of the traditional tethered DAQ system, the structural monitoring community has investigated alternative methods that could allow for a denser network of sensors with greater affordability. Of particular interest is replacing traditional cables with wireless sensing technology in the monitoring system (Figure 1-1b), thereby enabling an easier and quicker installation and leading to a reduction in

overall system cost. The utilization of wireless sensor networks (WSNs) for structural monitoring, and later structural control, has become increasingly popular for both commercial and academic use in a variety of applications (Straser and Kiremidjian 1998; Lynch 2002; Spencer *et al.* 2004; Lynch and Loh 2006).

Wireless sensors can come in two forms. In the first type, a traditional sensor is interfaced directly with a wireless radio, thus converting it into a "wireless" sensor. In the second type, the wireless sensor is not a sensor *per se*, but rather a wireless data acquisition node which interfaces with external sensing transducers. This second class of wireless sensor is sometimes also referred to as a wireless sensing unit (WSU). Wireless sensing units act as individual data acquisition nodes, capable of collecting data from an external transducer and processing data locally. Each wireless sensor node is typically comprised of a low power computing core, a sensor interface (*i.e.*, analog-to-digital converter), and a wireless transceiver (Figure 1-1c). This enables on-board data collection and processing, as well as stream-lined communication with either a base station unit or between other nodes in the network in a peer-to-peer fashion. Typically, each wireless sensor node in the network costs less than several hundred dollars (Lynch and Loh 2006; Lynch 2007), making it now possible to deploy dense arrays of wireless sensors across the structure.

With the advent of this new sensing paradigm came many successful structural monitoring deployments on a variety of civil infrastructure systems including bridges (Straser *et al.* 1998; Lynch *et al.* 2002; Pakzad *et al.* 2008; Jang *et al.* 2010; Kim *et al.* 2010), wind turbines (Rolfes *et al.* 2007), ships (Paik *et al.* 2009; Swartz *et al.* 2012), and buildings (Kurata *et al.* 2003; Kim and Lynch 2012). While all of these deployments have been successful and have highlighted the many benefits of the technology (*e.g.*, ease of installation, localized data processing), they also illuminated many of the performance bottlenecks associated with wireless sensors in long-term field deployments. Some of these challenges include: 1) limited communication bandwidth which limits the network's ability to reliably transfer data to a centralized location in real-time; 2) the lack of reliable power sources; and 3) limited physical robustness of the sensing nodes in harsh environments. Researchers have sought to overcome the limitations of available radio bandwidth, and hence communication contention between nodes, through novel

communication schemes such as pipelining (Kim *et al.* 2007) or by implementing multiple sub-networks of sensors on the same civil infrastructure system (Jang *et al.* 2010; Kurata *et al.* 2013). While such methods have been successfully validated in the field, these techniques also require complex time synchronization schema (Pakzad *et al.* 2008; Feltrin *et al.* 2010; Kurata *et al.* 2013) and sometimes result in incomplete data acquisition due to radio interference or lost data packets (Pakzad *et al.* 2008). Researchers have also attempted to address the power constraints of WSNs by utilizing: 1) alternative energy sources (such as wind and solar) for power (Jang *et al.* 2010; Park *et al.* 2010; Kurata *et al.* 2013), 2) minimizing power consumption by designing wireless sensors that use low-power components, and 3) integrating periodic sleep intervals into daily monitoring activities (Rice *et al.* 2010; Kurata *et al.* 2013). Even with these promising advancements, power constraints still remain a major challenge for WSNs that inhibit long-term field deployments. Alternative and previously unexplored approaches to wireless monitoring may resolve many of these bottlenecks.

As an additional add-on feature, wireless sensor nodes can also be equipped with actuation interfaces (Lynch *et al.* 2008; Sun *et al.* 2012), thus enabling structural control (Figure 1-1c). When considering this application with wireless telemetry, the new technology has been successful due to its localized, parallel processing capabilities, thus enabling more effective management of network resources through decentralized control (Wang *et al.* 2007; Swartz and Lynch 2009). However, such applications are limited to reliance on a shared communication channel that can get congested during the operation of the control system, leading to lost data and a reduction in the performance of the control solution. Additionally, while each wireless sensor node has on-board computing capabilities thus allowing it to act as a controller (*i.e.*, determine control forces). However, these are limited by a computing core whose computational capacity is significantly lower than that of a centralized computer. As such, complicated control algorithms require significantly more computational time when embedded on a single node which in turn can lead to delays between the taking of measurements and the application of control forces. These delays generally degrade system performance. Yet again, this trend toward computation inundation in wireless sensor nodes may be

overcome by exploring less traditional sources of inspiration for a new paradigm in sensing and actuation.

While the integration of wireless telemetry into structural monitoring and control has greatly advanced both fields, certain limitations of the technology prevent full realization of its potential. The challenges of guaranteeing reliable communication can inhibit real-time data processing due to lost packets and the need for recollecting data. Additionally, the limited computational capacity of each node can lead to computation inundation and also inhibit real-time data processing. These limitations create performance bottlenecks that must be overcome if wireless sensing technology is to become more attractive for real-world use in operational structures. To overcome grand engineering challenges such as these, in recent years engineers have turned to biology for sources of inspiration, thus giving rise to a new field called bio-inspired engineering.

1.3. Bio-Inspired Engineering

Engineering has long been tied to chemistry and physics within the hard sciences and many engineering feats are closely linked with a high level of understanding of these fields. Physics offers laws of statics, dynamics, electricity, and magnetism that have largely affected the bounds on engineering since society first sought to problem solve. As an example, when considering the realm of sensors and actuators, the earliest accelerometers relied on the principles of the dynamic response of a single degree of freedom mass (Walter 2007). For actuators, magnetorheological (MR) dampers are based on the principles of magnetism to create variable control forces (Weiss *et al.* 1994). Chemistry, on the other hand, offers laws of molecular behavior from an atomistic viewpoint. As the field of chemistry has advanced, so has its application toward engineering. A particularly significant advancement was the invention of the transistor (Nelson 1962) which greatly revolutionized all electronics, including sensors and actuators, by enabling the miniaturization of a countless number of components. While engineering has been largely tied to both physics and chemistry, the third natural science, biology, remained largely unattached to engineering until recent years. Of course, engineers have been taking cues from biology in their design for centuries. Many ideas

and inventions, such as Velcro and early attempts at human flight, were originally conceived from biological sources (Jenkins 2012). However, with new technology advancements, such as higher precision microscopes, biologists are able to explore the world at new levels, thus enabling a deeper understanding of living forms. From this exploration and observation, it is clear that in all areas of biology nature has engineered complex structures and systems whose capabilities far exceed many of the current engineering technologies and feats. As such, biology is a logical source of inspiration for deriving solutions to today's complex engineering challenges and bottlenecks.

Bio-inspired engineering has quickly gained footing in a wide variety of applications. Robotics is a natural fit for bio-inspired engineering and many researchers have studied the locomotive techniques of biological specimens in order to improve the capabilities of their robots for numerous applications. For example, based on the locomotion of the lobster, Ayers and Whitting (2007) created a bio-inspired robot that can traverse underwater terrains more easily. Additionally, Chang-Siu *et al.* (2011) drew inspiration from the tail movement of a jumping lizard for stabilizing a land robot and Menon and Sitti (2006) developed a climbing robot based on the adhesive foot surface and gait of a gecko. These are only a few examples; numerous other researchers have explored various biological systems for overcoming engineering constraints. Another area that has been explored is the development of new materials based on properties found in biological systems. Many researchers have explored the hierarchical nanostructure of materials such as teeth, bone, and nacre for the development new composite materials that exhibit the same strength and toughness of their biological counterparts (Ji and Gao 2004). Others have considered the water-repellant characteristics of certain leaves, such as the lotus leaf, to develop similar traits in textiles or corrosion resistant metals (Yao *et al.* 2011). Again, these are only a few examples within the realm of bio-inspired materials and numerous other examples can be found within the literature.

Artificial intelligence (AI) has long been tied to bio-inspired computing first through the development of specific bio-inspired algorithms and more recently through a concrete bio-mimicry of signal processing within the brain. The artificial neural network (ANN) (Yegnanarayana 2004) was the first attempt in machine learning to encapsulate

the functionality of biological signal processing but many other algorithms such as the genetic algorithm (Whitley 1994) and particle swarm optimization (Kennedy 2010) have since evolved based on biological principles. For the ANN, in particular, researchers sought to leverage the parallel processing capabilities of the brain in order to potentially establish a new computing paradigm that was not based on the traditional von Neumann computer (Farrar and Worden 2012). However, through years of development and iterations, this bio-inspired algorithm has strayed from its original source of inspiration and is largely unable to achieve its original design goals. Recently, others have delved further into the processing capabilities of the brain with the ultimate quest of creating super-computing architectures based on the biological brain through cognitive computing (Modha *et al.* 2011). To achieve this lofty goal, researchers have simulated the interconnectedness between processing units within the brain on integrated chips in order to capture the streamlined computing capabilities that are seen in biological sensory systems. While this has been proven successful on small-scale (Ananthanarayanan *et al.* 2009), there are still many challenges that must be overcome to fully encapsulate the functionality of the brain.

Therefore, bio-inspired engineering has recently emerged as a field that seeks to overcome engineering challenges with solutions derived from biology. Given its success in many different areas of engineering, this study seeks to leverage biological principles to overcome the aforementioned bottlenecks found in wireless sensor nodes when used for the purposes of structural monitoring and control. In particular, this study focuses on the adaptation of the signal processing capabilities of biological sensory systems to wireless sensor nodes in order to create a new sensing and actuation paradigm. To set precedence for this, however, the original bio-inspired algorithm, ANN, will be explored with an application to wireless sensor nodes in order to fully understand the limitations of this learning and computing algorithm. Based on the findings from this study, a new sensing and actuation paradigm is sought that has stronger ties to biological sensory systems.

1.4. Signal Processing and Actuation in Biological Systems

Through the process of evolution, biological sensory systems have advanced into highly adaptive and robust entities (Kandel 2000) with processing capabilities that far surpass current engineering technologies (Mead 1990). As such, inspiration for a new sensing and actuation paradigm can be drawn from the biological sensory system, thus potentially addressing the deficiencies currently found in WSNs, both across the network and with individual nodes. The processing mechanisms used in biological sensory systems are attractive to engineers and scientists due to the simplistic individual functional unit, the neuron, that inevitably forms complex architectures with other units to achieve computing objectives in real time (Modha *et al.* 2011). The neuron, as first proposed by Nobel laureate Santiago Ramòn y Cajal in 1891, is the basic building block in the biological sensory system because it functions as the key information processing unit (Nicholls *et al.* 2001). The neuron is comprised of three main components (Figure 1-2.a): 1) tree-like structures called dendrites which receive information from surrounding neurons, 2) the soma which makes decisions based on the integration of these inputs, and 3) the axon which transmits the decision of the soma to the synapse of surrounding neurons via the terminal buttons.

Signal transmission within the neuron relies on the membrane potential, or the voltage difference between the interior and exterior walls, of the neuron. Messages from external sources to the neuron change this potential by either inhibiting (closing) or activating (opening) ionic channels within the cell, thus causing the voltage difference across the cell to become more negative or positive. If the membrane potential reaches a threshold voltage, however, the cell fires an electrical spike, called an action potential. An action potential (Figure 1-2.b) is considered to be all-or-nothing event because it only occurs when a specific threshold membrane voltage has been reached (Nicholls *et al.* 2001); when it does occur, it has a constant amplitude and duration. As a result, a single spike cannot encode significant information about the input stimulus and instead the firing rate between multiple spikes carries information about the input signal such as magnitude or amplitude (Bialek *et al.* 1991). This resulting binary spike train is a highly compressed representation of the neuron's input stimulus, thus requiring minimal energy

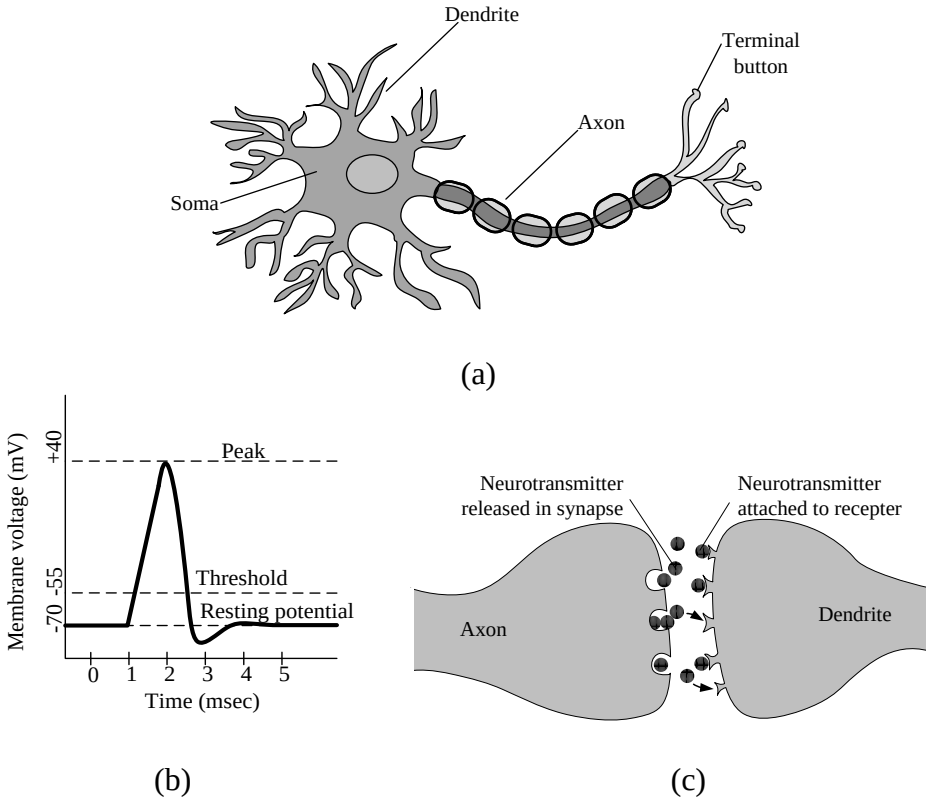

Figure 1-2. Schematic of neuron (a), single action potential (b), and synapse (c).

for transmission to surrounding neurons. The spike train is transmitted down the axon, where it must cross synapse which is the connection to the dendrite of another neuron cell (Figure 1-2c). At the synapse, the electrical signal is converted to a chemical signal through the release of ionic compounds, called neurotransmitters, which convey the message to the receiving neuron. These neurotransmitters will either enhance or inhibit the receiving neuron's tendency to emit its own electrical pulses depending on the type of connection between the two neurons. Through these connections, a single neuron is able to convey its information to multiple neurons simultaneously, resulting in a complex interconnection of information flow.

The primary function of the sensory system is to receive, integrate, and transmit binary spike train information such that a reaction is formulated by the organism in response to an environmental stimulus. The neuron is the basic building block that allows for such mechanisms, but numerous research studies have determined that the response of an individual neuron contributes very little to the resulting response of the

organism (Georgopoulos *et al.* 1986; Lewis and Kristan 1997). Instead, individual neurons must extensively collaborate to form networks with decision-making skills far superior to the capability of an individual neuron. As such, sensory information is processed in relays, or layers, with each progressive relay within the network capable of more complex decisions (Kandel *et al.* 2000). The architecture of these networks is not absolute, however, and connections between individual neurons are often reinforced or eliminated based on experience, thus allowing the organism to achieve its objective more efficiently with increased learning (Schultz *et al.* 1997; Song *et al.* 2000). Additionally, the sensory system processes information from multiple input sources simultaneously through parallel neural networks, thus allowing for higher processing efficiency. This also includes an aggregation of data from multiple sensor types through sensor fusion, resulting in a deeper foundation of knowledge for decision making. The precise methodologies that biological systems use to integrate information from multiple sources are largely unknown, although current theories trend toward a form of probabilistic pattern recognition (Bialek *et al.* 1991; Rieke *et al.* 1999; Dayan and Abbott 2005; Averbeck *et al.* 2006). Regardless of the mechanism, networks of biological neurons are able to make extremely sophisticated decisions with reaction times in the millisecond range which is an attractive feature for engineering applications that require real-time decision making.

The processing techniques offered by biological systems differ in many ways from the traditional methods used in engineering applications; it is these differences that make them attractive sources of inspiration (Table 1-1). In contrast to the rigid architectures of engineering systems, the laws of natural selection have allowed biological systems to become extremely adaptable to environmental stimulus and to learn through experience. This high level of adaptability is achieved through large, complex networks of neurons that modify their connections to process and aggregate information so that information-rich representations of input stimuli can be formulated. Biological systems, however, have had the advantage of centuries of evolution, molding them into functional systems that are well-suited for their environment. Biological systems are also able to process vast amounts of information very rapidly and with minimal energy consumption through very compressed communication mechanisms. Current engineering

Table 1-1. Summary of capabilities and deficiencies of biological sensing systems.

Benefits of Biological Sensing Systems	Deficiencies of Biological Sensing Systems
• Extremely adaptable to environmental stimulus • High level of redundancy • Capable of decentralized, real-time processing • Operates solely in analog domain • Communicates through compressed format	• Required thousands of years of evolution to achieve current system • Relies on thousands of processing units • Individual processing unit is "unreliable"

technologies (such as WSNs) are much more power intensive and may largely benefit from adapting the compressive techniques utilized by biological sensory systems. Finally, biological systems operate through analog mechanisms, allowing for real-time processing. Modern engineered systems, on the other hand, must perform numerous conversions between the analog and digital domains which inhibit the computational speed of the overall network. By drawing inspiration from biological systems, new methods of sensing and control can be formulated that address deficiencies in WSNs (Figure 1-3.).

1.5. Artificial Neural Networks

The adaptive architectures and parallel processing capabilities offered by biological systems have long been attractive to mathematicians and engineers. Artificial neural networks (ANNs) were first developed in the early 1950's as an attempt to formulate mathematical representations of the information processing techniques found in biological systems (McCulloch and Pitts 1943; Minsky 1961; Rosenblatt 1962). With this new algorithm it was hoped to achieve a new computing paradigm that leveraged the adaptive learning capabilities, fault tolerance, and nonlinear processing capabilities of biological neural networks (Haykins 1994). Early efforts in this area focused on a basic building block termed the linear perceptron that accepted n number of inputs, x_i (i=1,..., n), scaled the inputs by a weight, w_i, and summed the resulting values, $\Sigma x_i w_i$.

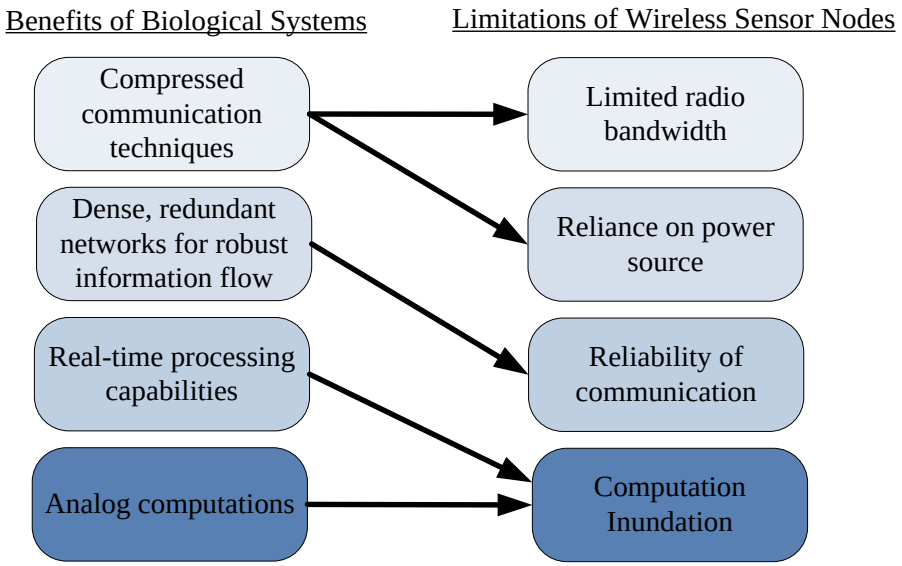

Figure 1-3. Utilization of biological processes for inspiration in addressing WSNs' current limitations.

This sum was then compared with a threshold value, α, and an output y was produced that was one if the sum exceeded the threshold and zero otherwise,

$$y = \begin{cases} 1 \text{ if } (\sum_{i=1}^{n} x_i w_i) \geq \alpha \\ 0 \text{ if } (\sum_{i=1}^{n} x_i w_i) < \alpha \end{cases} \quad (1.1)$$

thus acting as a step activation function (Figure 1-4). This simplistic design was termed the McCulloch-Pitts perceptron. The intent of the design was to model the interactions of biological neural networks where the interconnectedness of the model represented axons and dendrites, the activation function symbolized processing in the soma, and the weights approximated the synaptic strength between neurons (Jain and Mao 1996). While these early neural networks successfully captured the threshold activation nuance of biological systems, they lacked the capability of making sophisticated decisions like their biological counterparts and were limited to linear classification applications. Additionally, early applications of neural networks lacked rigorous methods for autonomously determining the weights, or the synaptic strength, between connected nodes, making them difficult to implement (Jain and Mao 1996).

With these limitations, neural networks did not gain popularity until the early 1980's when a novel training algorithm termed backpropagation was first proposed by

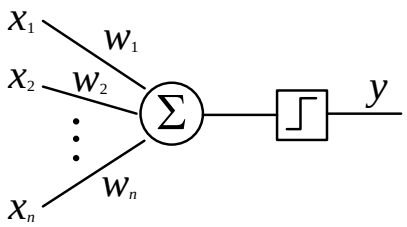

Figure 1-4. McCulloch-Pitts perceptron.

Werbos (1974) and then re-popularized through novel applications by Rumelhart *et al.* (1986). Shortly following this reinvention, it was demonstrated that virtually any static function could be approximated by neural networks (Cybenko 1989; Hornik *et al.* 1989) and more specifically, a properly designed three layer network could be used to model any nonlinear function (Hecht-Nielsen 1989). These significant findings led to an explosion of applications across all engineering fields, including pattern classification, categorization, function approximation (regression), prediction, optimization, and control (Jain and Mao 1996).

While the original intent of ANNs was to relate to the processing mechanisms employed by biological systems, the architecture of the networks quickly evolved into increasingly complex representations whose methods of analyses largely deviated from the original source of inspiration. For example, many training algorithms for ANN require that the activation function be continuously differentiable, thus making the simplistic step function a poor choice for an activation function. Instead, more complex activation functions have been proven to be better suited for the training, such as sigmoidal functions or Gaussian functions, but these functions have weaker ties to the original biological inspiration of ANN. As such, while ANNs attempt to encapsulate the complex flow of information within biological neuronal networks, these networks now largely deviate from their original source of inspiration. The training techniques and architectural design are hardly reminiscent of the techniques utilized by biological systems (Grossberg 1987); apart from their parallel processing capabilities and general neuronal architecture, ANNs lack the previously outlined benefits provided by biological systems. In light of this, this thesis focuses on returning to the biological systems that provided inspiration for artificial neural networks in order to establish a new paradigm

for signal processing, sensing, and actuation that is more directly based on biological principles.

1.6. Research Objectives and Dissertation Outline

While early bio-inspired algorithms, such as artificial neural networks, attempted to encapsulate the processing capabilities of biological systems, they inevitably strayed from their source of inspiration and now miss out on the potential benefits associated with biological sensory systems. As such, this dissertation seeks to return to the source of inspiration for artificial neural networks (*i.e.*, biological sensory systems) to fully leverage the benefits of such systems and therefore address the current bottlenecks seen in wireless sensor nodes for the purpose of structural monitoring and control. By adopting the compressive data transmission strategies, parallel processing, and analog computing techniques of biological sensory systems, a new paradigm in wireless sensing will be established that is alleviated from the current wireless sensor node constraints of limited radio bandwidth, large power consumption, and computational inundation. Each successive chapter is founded on the signal processing techniques employed by biological sensory systems and progresses from theoretical principles to implementation and validation in hardware (Figure 1-5). The objectives of this dissertation are to:

- explore artificial neural networks, the traditionally bio-inspired algorithm, as they relate to wireless sensor nodes so as to define a baseline for the current bio-inspired signal processing method and to establish areas for improvement;
- develop and implement a new sensing and signal processing paradigm based on the operational principles of the biological sensory system in order to address the current bottlenecks of wireless sensing and control;
- develop and implement a new control paradigm based on actuation mechanisms employed by the biological sensory system.

In *Chapter 2: Distributed Neural Computations in Wireless Sensor Networks Using Artificial Neural Networks*, artificial neural networks will be revisited in order to understand the true benefits and limitations of this traditional bio-inspired algorithm. While it has already been acknowledged that ANNs are only loosely based on biological

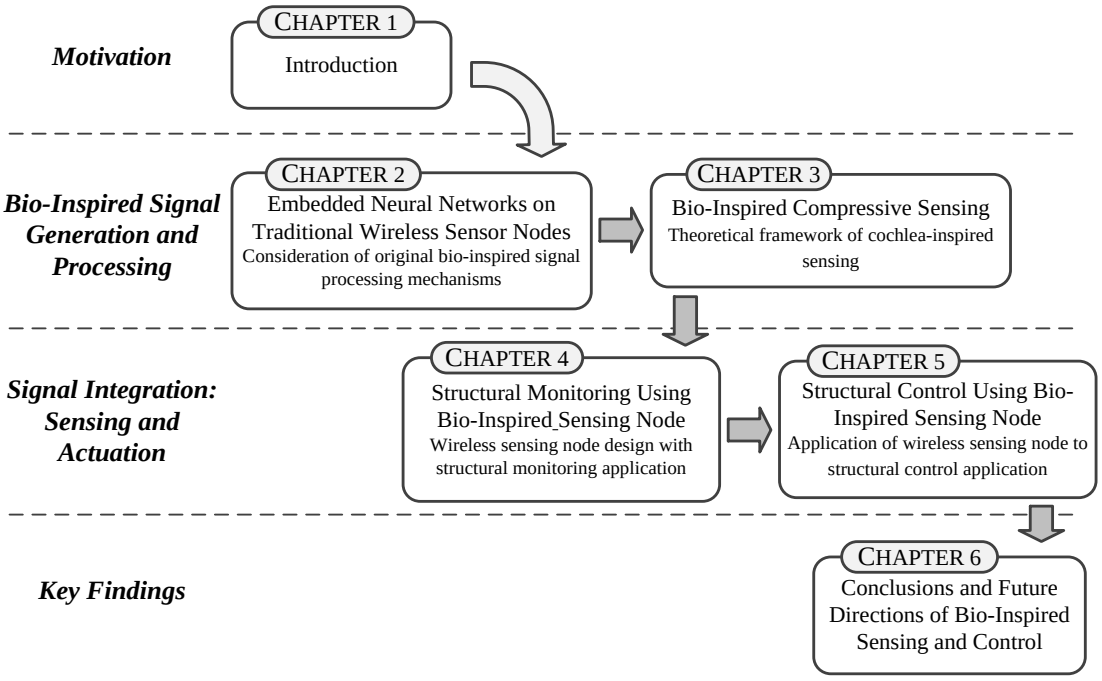

Figure 1-5. Schematic representing the major topics covered in this dissertation.

neural circuits, the algorithm is computationally efficient and may still provide some benefit for the purposes of structural monitoring and control. This possibility will be further explored in this chapter. Additionally, by implementing an ANN within a WSN, the limitations of the algorithm will also be highlighted, thus providing further motivation for re-aligning with the original biological source of inspiration. Due to its streamlined architecture, the Volterra-Weiner neural network is adopted as the traditional bio-inspired algorithm in this study and it is decentralized across a network of wireless sensor nodes, thus enabling parallel processing. These distributed computing techniques are evaluated by predicting the response of a six-story shear structure when subject to seismic ground motion. It is demonstrated that only modest benefits are gained by decentralizing the algorithm across a network of sensor nodes.

By recognizing the limitations and deficiencies of the commonly-utilized artificial neural network and also considering the known bottlenecks of wireless nodes for the purposes of structural monitoring and control, *Chapter 3: Utilizing the Cochlea as a Bio-inspired Compressive Sensing Technique* seeks to return to the biological sensory system to establish a new paradigm for sensor networks. In doing this, the benefits of the

biological sensory system, such as compressive data transmission and real-time processing capabilities, will be leveraged so that the deficiencies of WSNs can be addressed. From this study, it is found that the method by which biological sensory systems transmit data is highly compressive, thus resulting in large energy savings during signal processing of input stimuli. Traditional ANNs do not leverage these compressive transmission techniques and therefore do not see these benefits. The techniques used by biological sensory systems are analyzed from an engineering perspective and compared against other traditional data compression techniques. It is found that while some traditional techniques result in lower reconstruction error after compression, the bio-inspired method achieves similar compression rates while being the only one offering real-time processing.

In *Chapter 4: Resource Efficient Wireless Sensor Network Architecture based on Bio-Mimicry of the Mammalian Auditory System* the new sensing paradigm is implemented in hardware in the form of a new wireless node. By leveraging the benefits of the biological sensory system, this new sensing node is designed to address some of the challenges of traditional WSNs such as limited radio bandwidth and computation inundation. First, this sensing node leverages the benefits seen in biological sensory systems through real-time pre-processing with analog circuitry. Next, this processed data is compressed into single-byte wireless packets and transmitted to a centralized receiver. The performance of the proposed sensor is validated on a single degree-of-freedom structure that is excited by seismic ground motion signals. The proposed sensor is optimized for monitoring both seismic signals and the response of a structure when subject to seismic excitation. Overall, this chapter demonstrates its real-time monitoring capabilities of the new wireless node while maintaining high data compression rates and therefore, alleviating some challenges faced by WSNs.

Once the new bio-inspired wireless sensor node has been successfully implemented in a structural monitoring application it is next used for the purposes of real-time control in *Chapter 5: Real-Time Control of Civil Infrastructure using Wireless Sensor Networks based on Bio-Mimicry of the Biological Sensory System*. While WSNs for the purposes of feedback control can become inundated with computations, thus reducing their real-time capabilities, biological systems are capable of streamlined

processing that result in reflexive, real-time actuation. In this chapter, the mechanisms employed by biological sensory systems for actuation are explored and the wireless sensor node is applied to a bio-inspired control application, thus highlighting real-time capabilities during time-critical events. The streamlined feedback system is validated on a four degree-of-freedom structure that is subject to seismic ground motions.

Finally, in *Chapter 6: Conclusions* key findings from the thesis are provided. The benefits of the new bio-inspired wireless sensor as they pertain to structural monitoring and control are highlighted. Additionally, an outline for potential future work in the area of bio-inspired sensing and control for civil infrastructure is provided.

CHAPTER 2

DISTRIBUTED NEURAL COMPUTATIONS IN WIRELESS SENSOR NETWORKS USING ARTIFICIAL NEURAL NETWORKS

2.1. Introduction

Researchers have attempted to encapsulate the signal processing capabilities of biological sensory systems through complex networks of interconnected computing nodes, called artificial neural networks (ANNs). While this field of study has had relative success over the last several decades (Haykins 1994), it has largely strayed from its original biological source of inspiration (Mehrotra *et al.* 2000). To fully understand the benefits, as well as shortcomings of this foundational bio-inspired signal processing technique, a traditional ANN is explored as it relates to structural health monitoring (SHM) using wireless sensor networks (WSNs). In doing this, it is hoped that some of the traditional deficiencies of WSNs (*e.g.*, limited radio bandwidth, reliance on finite power sources) will be overcome and if not, areas in which biological sensory systems can better serve as a source of inspiration for wireless sensor nodes will be illuminated.

In recent years, many researchers have focused on embedding various algorithms in WSNs. These efforts leverage each node's computational capacity as well as the parallel processing capabilities across the network by manipulating data prior to transmission. By doing this, low bandwidths of processed data can be transmitted across the network as opposed to high bandwidths of raw data. As communication is often the most power intensive component of a sensor node (Lynch *et al.* 2004), taking advantage

of these computing capabilities of the node to compress raw data prior to transmission results in higher energy savings and better use of radio bandwidth. Initially, researchers focused on embedding algorithms that required no communication between sensor nodes, such as the fast Fourier transform (FFT) and auto-regression (AR) models (Lynch *et al.* 2003; Nitta *et al.* 2005), but this resulted in only localized information extraction and did not take advantage of the intra-network capabilities of the technology. These limitations prompted researchers to utilize node-to-node communication techniques that would allow for global information (*e.g.*, mode shapes, state space models) to be extracted from the data through collaborative efforts of the entire wireless sensor network (Chintalapudi *et al.* 2006; Zimmerman *et al.* 2008; Sim *et al.* 2010). In addition to gaining system-wide spatial properties, the addition of node-to-node communication allows WSNs to perform more efficient parallel processing by reaping computational efficiency as memory intensive algorithms can now be decentralized across a network of sensors. Zimmerman and Lynch (2009) first demonstrated the benefits of this parallel processing environment by distributing a parallelized version of simulated annealing across a network of sensors to solve combinatorial optimization (CO) problems. The parallel architecture of decentralized algorithms reduces processing time and requires minimal communication, thereby reducing overall energy consumption.

The inherent parallel architecture of artificial neural networks lend themselves well for embedding in wireless sensor networks. By distributing an ANN across a network of nodes, the parallel processing benefits of the algorithm can be realized and overall processing time can be reduced. Similar to its biological source of inspiration, each node within the ANN employs very simple computations that can be quickly shared amongst all of the nodes to produce the desired algorithm output. By distributing these computations across a WSN, the network should experience large energy savings through increased computational efficiency. However, it is also anticipated that due to the interconnectedness of the ANN architecture, there will be an increase in communication costs which may overpower the benefits seen from the computational parallelization. In this study, the benefits and limitations of this distributed algorithm will be explored as they relate to wireless sensor nodes. In doing this, it is thought that the deficiencies of

the traditional bio-inspired algorithm will be more transparent, thus highlighting areas for improvement in terms of a new bio-inspired sensing paradigm.

In this study, a decentralized parallel architecture will be developed for an artificial neural network. The neural network of choice is the Volterra-Weiner neural network (VWNN), first developed by E.B. Kosmatopoulos *et al.* (2001) and further refined by Pei *et al.* (2004). Its selection is due to its unique architecture that allows for intuitive decomposition across a WSN. For validation of the embedded algorithm, acceleration data collected from a six-story shear structure is used to train and test the decentralized VWNN. Additionally, the algorithm is first embedded on a single wireless sensor and then distributed across a network of sensors. This decentralization is examined in a quantitative manner so as to better highlight the benefits and limitations of ANN.

2.2. Volterra-Weiner Neural Networks (VWNN)

When properly designed, artificial neural networks are powerful tools that can efficiently model the nonlinear behavior of a system through regression. As first demonstrated independently by Cybenko (1989) and Hornik *et al.* (1989), given an unlimited number of hidden nodes, a multilayer feedforward neural network can approximate virtually any static function of interest. Other powerful neural networks that are capable of approximating more complex nonlinear functions have been reviewed in the literature (Haykins 1994; Bishop 2006). This capability to model any behavior, and specifically non-linear hysteretic behavior, allows neural networks to be applied to a wide range of engineering applications across numerous disciplines. In particular, artificial neural networks are highly adaptable tools that can be used for a variety of applications, such as non-linear system analysis or pattern recognition, making them a valuable resource for many different structural health monitoring applications.

ANNs are typically considered to be powerful “black box” modeling tools whose inner workings are not easily understood due to the complex interconnectedness of the algorithm. A traditional neural network has full connectedness between the input layer

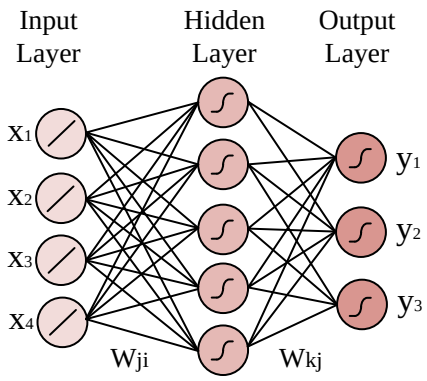

Figure 2-1. Architecture of traditional neural network. Note that multiple hidden layers can be used.

and its hidden layer(s), as well as between the hidden layer(s) and the output layer (Figure 2-1), thus enabling it to capture non-linear behaviors but also adding to the complexity of the mapping between input and output values. This complex architecture presents several issues when attempting to design the appropriate neural network for a given application. First, determining the appropriate number of hidden nodes, as well as hidden layers, is fairly ambiguous and while some guidelines have been established (Duda *et al.* 2001), developing these values often a trial and error process. Additionally, throughout the evolution of the algorithm, several activation functions within the hidden nodes (*e.g.*, sigmoidal functions, Gaussian functions) have arisen and choice of this function has an impact on the training speed of the algorithm, as well as on the overall effectiveness of the network. In general, the convergence of the algorithm during training (*i.e.*, determining inter-layer weighting values), as well as ability of the network to achieve its objectives, is highly dependent on the appropriate architecture which is dictated by the number of hidden nodes and activation functions. As a result of these factors, designing an effective ANN is as much of an art as a science that requires an intimate knowledge of the field.

The Volterra Weiner neural network, however, was designed to allow for greater transparency in its application. First proposed by Kosmatopoulos (1998), the architecture was designed to predict output functions based on nonlinear relationships with input functions. Kosmatopoulos (1998) originally used this network for control of nonlinear systems and later refined the network to predict restoring forces in nonlinear structures

(Kosmatopoulos *et al.* 2001). With the latter study, Kosmatopoulos *et al.* (2001) used the network to model the restoring forces of a multi-degree-of-freedom structure with each output node representing a single degree of freedom. The inputs of the network were the acceleration of all of the degrees of freedom and also a control force vector, while the output was the restoring forces at each degree of freedom. In a subsequent study conducted by Pei *et al*. (2004), the VWNN was further refined to increase the transparency of the VWNN by again modeling the non-linear hysteretic behavior of multi-degree of freedom structures. In this study, the input nodes included displacement, velocity, acceleration, and the restoring force at the current time step as well as the anticipated restoring force at the next time step for each degree of freedom. These inputs were used to predict the acceleration at the next time step. In this study, Pei *et al.* (2004) further defined the architecture so as to give a near-parametric definition to the design and training of the network, thus resulting in near-transparent use of the network. Due to the applicability of the neural network to multi-degree-of-freedom systems, as well as because of its intuitive design, the VWNN was chosen as the neural network architecture for this study on embedded ANNs in WSNs.

Figure 2-2 presents the VWNN architecture as outlined by Kosmatopoulos *et al.* (2001) and adapted by Pei *et al.* (2004). Within this architecture, the input layer consists of 5n input nodes, where n is the number of degrees of freedom of the system of interest. As previously seen with the VWNN (Pei *et al.* 2004), these inputs include displacement, velocity, acceleration, force at the current time step, and force at the next time step for each degree of freedom in the system. Displacement and velocity are calculated from acceleration through a pre-processing step using the variable α, and therefore, α acts as a time-step integrator. The five inputs to the network are generically denoted as p_1 through p_{5n} in Figure 2-2. The input layer is singly connected to the hidden layer, where a single hidden node is denoted as h_i, through a weight value, λ. The number of nodes within the hidden layer is formulated based on the known non-linearities of the system of interest. Hidden nodes are introduced in "blocks" with the addition of each block permitting increasing fidelity when modeling nonlinearities of the system. First-order hidden nodes are formed based on a linear connection with the input nodes. All other higher-order nodes (*e.g.*, second-order, third-order) are formed directly from the lower-order hidden

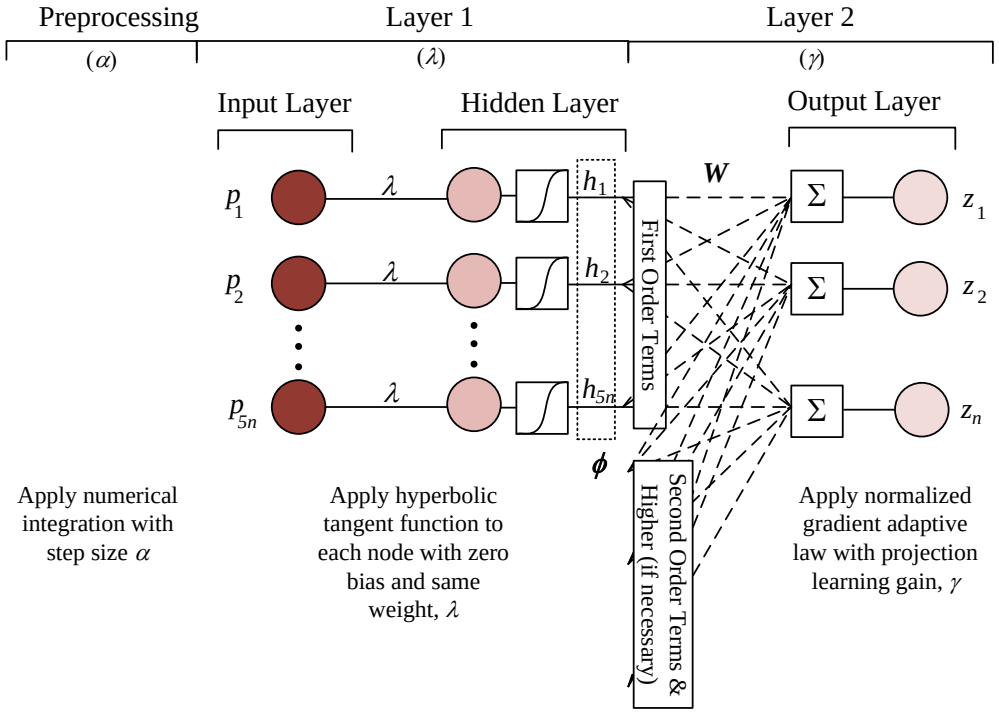

Figure 2-2. VWNN architecture (adapted from Pei *et al.* (2005)).

nodes. For example, to form second-order hidden nodes from an arbitrary number of q first order hidden nodes, h_1 to h_q, the outer product is taken of the first-order hidden nodes producing q^2 second-order nodes,

$$[h_1 \quad h_2 \quad \cdots \quad h_q]^{\mathrm{T}}[h_1 \quad h_2 \quad \cdots \quad h_q]=\begin{bmatrix} \boldsymbol{h_1^2} & h_1h_2 & \cdots & h_1h_q \\ \boldsymbol{h_1h_2} & \boldsymbol{h_2^2} & \cdots & h_2h_q \\ \vdots & \vdots & \ddots & \vdots \\ \boldsymbol{h_1h_q} & \boldsymbol{h_2h_q} & \cdots & \boldsymbol{h_q^2} \end{bmatrix}. \tag{2.1}$$

From these new terms, all redundant terms are eliminated (bold terms in the lower half of the square matrix in Equation 2.1 represent the retained terms) to increase computational efficiency, resulting in $\frac{q(q+1)}{2}$ second-order nodes. This entire set of second order nodes is then added to the neural network. With this addition, the network is better able to capture second-order nonlinearities. If it is desirable to model higher order nonlinearities, then higher order terms are added to the network through the same method as the second-order terms. Finally, as typically seen in traditional ANNs, the output layer is fully connected to the hidden nodes and each output node, z_i, represents an individual degree of freedom's

acceleration as predicted at the next time step. As such, the number of output nodes equals the number of degrees of freedom of the system in this case z_1 through z_n.

The connections from the hidden layer to the output layer captures the nonlinear relationships in the system through a weighting matrix, $\boldsymbol{W}$. Each j^{th} column of the weighting matrix, $\boldsymbol{w}_j$, is associated with the j^{th} output node and is updated during training through a normalized gradient adaptive law with a learning gain of γ,

$$\boldsymbol{w}_j(t_k+1)=\boldsymbol{w}_j(t_k)+\Delta\boldsymbol{w}_j(t_k) \tag{2.2}$$

where

$$\Delta\boldsymbol{w}_j(t_k) = \begin{cases} \gamma\varepsilon_j(t_k)\boldsymbol{\phi}(t_k) & \text{if } \|\boldsymbol{w}_j(t_k)\|<M, \text{ or} \\ & \|\boldsymbol{w}_j(t_k)\|<M \text{ and } \left(\gamma\varepsilon_j(t_k)\boldsymbol{\phi}(t_k)\right)^{\mathrm{T}}\boldsymbol{w}_j(t_k)\le 0, \\ \left(\mathbf{I}-\dfrac{\boldsymbol{w}_j(t_k)\boldsymbol{w}_j(t_k)^{\mathbf{T}}}{\boldsymbol{w}_j(t_k)^{\mathbf{T}}\boldsymbol{w}_j(t_k)}\right)\gamma\varepsilon_j(t_k)\boldsymbol{\phi}(t_k) & \text{otherwise,} \end{cases} \tag{2.3}$$

such that $\boldsymbol{\phi}$ is the hidden node output vector, t_k is the k^{th} time step, $\mathbf{I}$ is the square identity matrix with same dimensions as the length of $\boldsymbol{\phi}$, $\|\cdot\|$ is the l_2 norm, and M is a scalar design constant. The scalar $\varepsilon_j(t_k)$ is the estimation error,

$$\varepsilon_j(t_k)=\frac{g_j(t_k)-z_j(t_k)}{1+\boldsymbol{\phi}(t_k)^{\mathbf{T}}\boldsymbol{\phi}(t_k)} \tag{2.4}$$

where $g_j(t_k)$ is the desired value of the j^{th} output node and $z_j(t_k)$ is the network output for the j^{th} node.

Based on this architecture, there are three parameters (α, λ, γ) which are crucial in the design of the VWNN. Pei *et al.* (2004) developed near-physical meanings for each of these model terms such that the design of the network has an intuitive mechanics basis.

The first parameter, α, is considered to be the pre-processing design parameter and is utilized to approximate the velocity, $\dot{x}$, at t_k

$$\dot{x}(t_k) = \dot{x}(t_{k-1}) + \alpha\ddot{x}(t_k) \tag{2.5}$$

and then displacement, x,

$$x(t_k) = x(t_{k-1}) + \alpha\dot{x}(t_k) \tag{2.6}$$

from the measured acceleration, $\ddot{x}$. In this case, acceleration is the measured response of the structure and all other parameters are extrapolated from it. An accelerometer is the prevalent sensor of choice for data collection when measuring the response of dynamic structures due to its low-costs and ease of installation. Because of the derivation of displacement and velocity from acceleration, α is typically chosen to be equivalent to the time step of the system. This assumes that the time step $\Delta t = t_k - t_{k-1}$ is sufficiently small. The second parameter, λ, is the weight coefficient and determines the shape of the hyperbolic tangent function,

$$h(p_i) = 2\left(1+e^{-2\lambda p_i}\right)^{-1} - 1, \quad i = 1,...,5n \tag{2.7}$$

where p_i denotes the input to the i^{th} node and $5n$ denotes the number of model inputs (*i.e.*, displacement, velocity, acceleration of each degree of freedom at the current time step, as well as the current and future restoring force value at each degree of freedom). For a network using only first order nodes, small values of the weighting coefficient linearize the shape of the hyperbolic tangent function while large values saturate it. In this case, however, λ should be chosen such that a strong sigmoidal shape is given by the hyperbolic tangent function for the entire range of input values. If higher-order terms are included, more consideration should be used when choosing a value for λ and further details in this process can be found in Pei *et al.* (2004). The final parameter, γ, which is the adaptive gain, governs the convergence of the weighting matrix $\boldsymbol{W}$ during training with a normalized gradient adaptive law. If γ is too small the convergence of the weights will be very slow, while too large the weights may become unstable. The proper range for γ is often determined through an iterative process that seeks to minimizes the normalized

root mean square (RMS) error, e_{RMS}, between a desired output of the i^{th} output node, $\boldsymbol{g}_i$, and its neural network approximation, $\boldsymbol{z}_i$,

$$e_{RMS}=\frac{\|\boldsymbol{g}_i-\boldsymbol{z}_i\|}{\|\boldsymbol{g}_i\|} \tag{2.8}$$

where $\|\cdot\|$ is the is the l_2 norm. In this study, again $\boldsymbol{z}_i$ is the predicted acceleration at the i^{th} degree-of-freedom at the next time step. Even though guidance is provided for selecting initial values for α and λ, these too can be further refined by minimizing the RMS error of the system output.

The VWNN offers a unique architecture that enables intuitive design of the network, something which is often lacking with traditional neural networks. Because of this overall design transparency and associated streamlined architecture, the VWNN can be easily adapted to a decentralized neural network algorithm that can be embedded on a wireless sensor network. In this way, the parallel processing capabilities of the network will be leveraged and ideally, power savings will be established by taking advantage of localized data processing.

2.3. Embedding the VWNN in a Wireless Sensor Network

When considering embedment of an artificial neural network across a WSN, several factors must be considered. First, during the training mode of the ANN, the weighting matrix of the network is updated numerous times, thus requiring thousands of computations. The processing speed of a single wireless sensor node is only a small fraction of that of an ordinary personal computer, making updating the weighting matrix in the embedded environment a potentially arduous task. The second limiting factor when considering embedment of an ANN on a WSN is the communication requirement between each sensor. Theoretically, each interconnection between layers in the neural network would require communication in the WSN and if not properly considered, the WSN could rapidly become inundated with communication costs that far outweigh the computational efficiency of parallel computations.

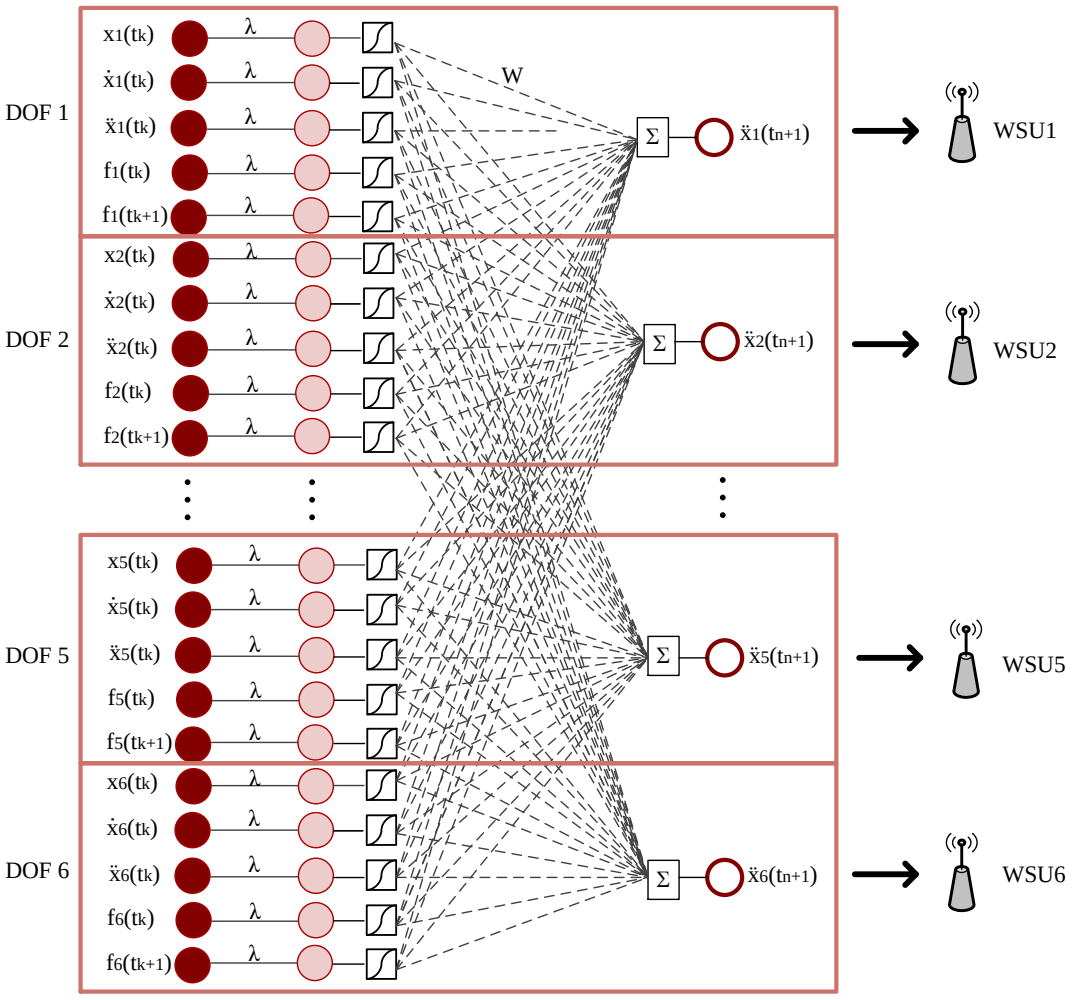

Figure 2-3. Distribution of a six degree-of-freedom system's Volterra-Weinter neural network onto six wireless sensor nodes. Each floor utilizes a unique wireless sensor node termed WSU1 through 6 and dotted lines represent wireless communication.

Decentralizing the ANN requires that each wireless sensor node is computationally responsible for a portion of the neural network. Due to its streamlined architecture, the VWNN presents itself well for decentralizing across a network of wireless sensors while minimizing communication costs (Figure 2-3). The construction of the input layer provides the first minimization of the required embedded WSN. Each degree of freedom in the system has five associated input nodes: 1) displacement, $x(t_n)$, 2) velocity, $\dot{x}(t_n)$, 3) acceleration, $\ddot{x}(t_n)$, 4) force at the current time step, $f(t_n)$, and 5) anticipated force at the next time step, $f(t_{n+1})$. One wireless sensor node can contain one degree of freedom's five neural network input nodes and perform all required pre-processing steps. Because each input node is singly connected to a hidden node, no

communication is required between the input node and hidden node so the five associated hidden nodes for a specific degree of freedom are also embedded on the same wireless sensor node. As such, each wireless sensor node will apply the tangent hyperbolic sigmoidal function required at each hidden node.

Due to the interconnection of the weighting matrix between the hidden layer and the output layer, all wireless sensor nodes must pass the output from their hidden nodes to all of the other nodes in the network. To achieve this, a waterfall algorithm is implemented to efficiently wirelessly communicate this information while still ensuring that all nodes receive the information. In this algorithm, Wireless Sensor Unit (WSU) 1 passes the output from its five hidden nodes to WSU 2. WSU 2 then passes its hidden nodes' outputs plus the information received from WSU 1 to WSU 3. This process continues to the final WSU in the network who then has the information required from all other units. This unit starts the same waterfall action by passing its information back down the chain of units and then continues with its calculations. There are more energy efficient algorithms for transmitting data throughout a WSN (Zhao and Guibas 2004) but the waterfall algorithm was chosen because it ensures that every node receives information from all other nodes in the network in an organized manner. Until all information has been received from all other processing units in the WSN, a single unit cannot continue its calculations. Thus, the extra energy consumption for a less efficient communication algorithm is acceptable because it ensures the success of the neural network predictions.

While the decentralized neural network algorithm can be embedded into any wireless sensor unit, the *Narada* wireless sensor node, developed at the University of Michigan (Swartz *et al.* 2005), was chosen as the data acquisition unit for this study due to its compact design, as well as having been tailored specifically for structural monitoring applications (Figure 2-4). The *Narada* has also been successfully used to monitor a variety of civil infrastructure including bridges (Kim *et al.* 2010; Kurata *et al.* 2013), wind turbines (Swartz *et al.* 2010), ships (Swartz *et al.* 2012), and buildings (Kim and Lynch 2012). This sensor node utilizes Atmel's ATmega 128 microcontroller (powered at 5V, with an 8MHz clock speed) to enable on-board computing. The unit includes an additional 128kB of external random access memory thus allowing data

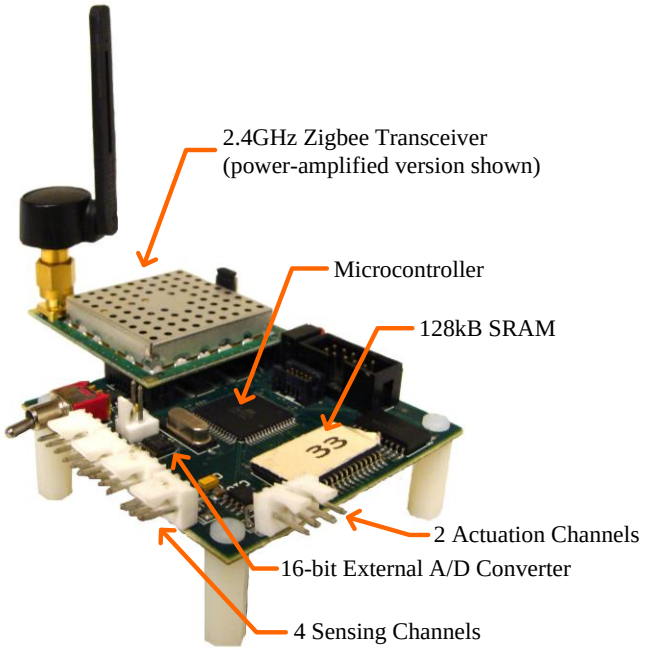

Figure 2-4. *Narada* wireless sensor node with long-range radio board.

storage and manipulation. Its sensing interface includes four input channels (0-5V) which feed into an external 16-bit Texas Instrument ASD8341 analog-to-digital converter (ADC) that is capable of high resolution data acquisition with high sampling rates up. A two channel actuation interface is also provided which is capable of outputting 0-4V signals. The unit uses a Chipcon CC2420 wireless Zigbee transceiver that is compliant with the IEEE 802.15.4 wireless communication standard, thus enabling reliable communication between units and to a centralized server. Two versions of the radio can be used: short-range and long-range. The long-range radio has been designed using power amplifiers on the radio output, thus offering 700m line-of-sight communication ranges.

2.4. Experimental Validation

In order to validate the computational efficiency of the distributed neural network, the algorithm is applied to data collected from a partial-scale six-story steel structure

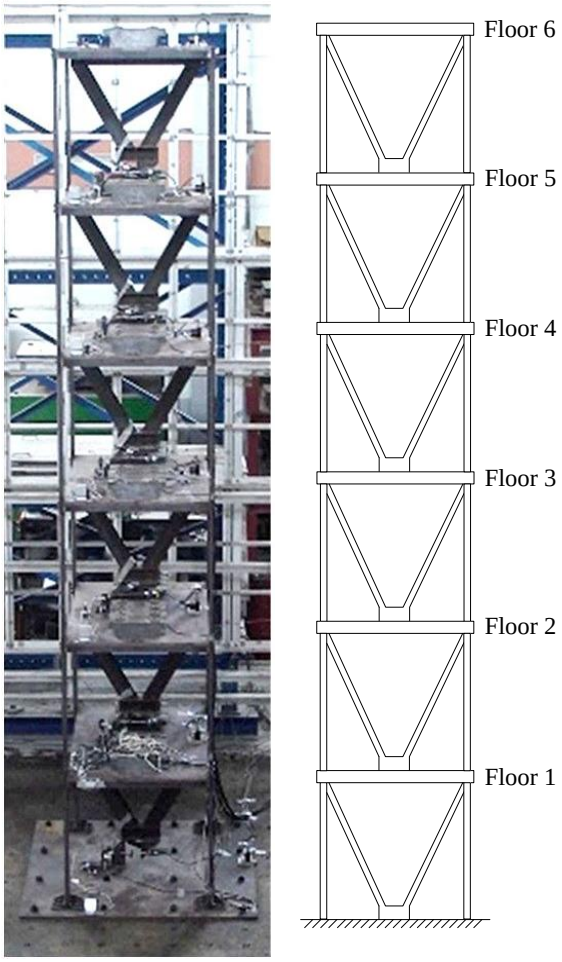

(a) (b)

Figure 2-5. Six-story shear structure (a) and model (b) used for validating the embedded Volterra-Weiner neural network.

located at the National Center for Research in Earthquake Engineering (NCREE) at National Taiwan University in Taipei, Taiwan (Figure 2-5). Each floor of the structure has a width of 1.0m, a length of 1.5m, and a height of 1.0m. The columns are 15cm x 2.5cm rectangular steel sections oriented on their weak axis. Steel wide flange H100x100x6x8 vertical braces are installed between every floor in order to resist lateral movement. For each story, the connection from the brace to the floor is a plate that can be varied in thickness, and thus stiffness, to create nonlinearities in the structure. The structure sits on a 5m x 5m shake table that is capable of applying seismic motion parallel to the long dimension of the structure. In this study, the structure is preliminarily subject to the El Centro earthquake with peak ground acceleration of 100gal ($10m/s^2$).

Each degree of freedom (*i.e.*, floor) on the structure has one *Narada* collecting data and executing its sub-section of the neural network, thus requiring six WSUs for the entire algorithm. According to the architectural design of the VWNN, each degree of freedom has five input nodes, five hidden nodes and one output node, all embedded on a single *Narada*. The weighting matrix ($\boldsymbol{W} \in \mathbb{R}^{6x30}$), is distributed across the network of *Naradas* such that each sensor contains one row, or 30 elements (with 5 elements contributed from each degree of freedom). For the VWNN, the three parameters, (α, λ, γ) are individually optimized by holding two parameters constant and then minimizing the average neural network approximation error, e_{AVG}, (or normalized RMS error) for all six degrees of freedom,

$$e_{AVG}=\sum_{i=1}^{N}\left[\frac{\left\|\ddot{\boldsymbol{x}}_i-\ddot{\boldsymbol{x}}_{est,i}\right\|}{\left\|\ddot{\boldsymbol{x}}_i\right\|}\right]N^{-1} \tag{2.9}$$

where N is the number of degrees of freedom in the neural network approximation (in this case 6), $\ddot{x}_i(t)$ is the structure's acceleration at the i^{th} degree of freedom, $\ddot{x}_{est,i}(t)$ is the neural network's approximation of the structure's acceleration at the i^{th} degree of freedom, Δt is the sampling time of the two signals, and K is the number of samples that result from this sampling scheme over some defined time horizon.

The pre-processing parameter, α, is initially chosen to be 0.005 to match the sampling frequency of the system (200Hz). During optimization of this parameter there is little variation in e_{AVG} (Figure 2-6a) and the final value is kept at 0.005. Because all inputs to the hidden layer fall between -1 to 1, the weight coefficient, λ, is first approximated as 1, which produces a strong sigmoidal shape in the hyperbolic tangent function for this input range. This value is fine-tuned through the optimization to a final value of 2.8 (Figure 2-6b). Because the final parameter, γ, governs the speed of convergence during training, a conservative initial value is chosen as 1.0 which may lead to slow convergence but will always be stable. This was then optimized to a final value of 1.8 (Figure 2-6c).

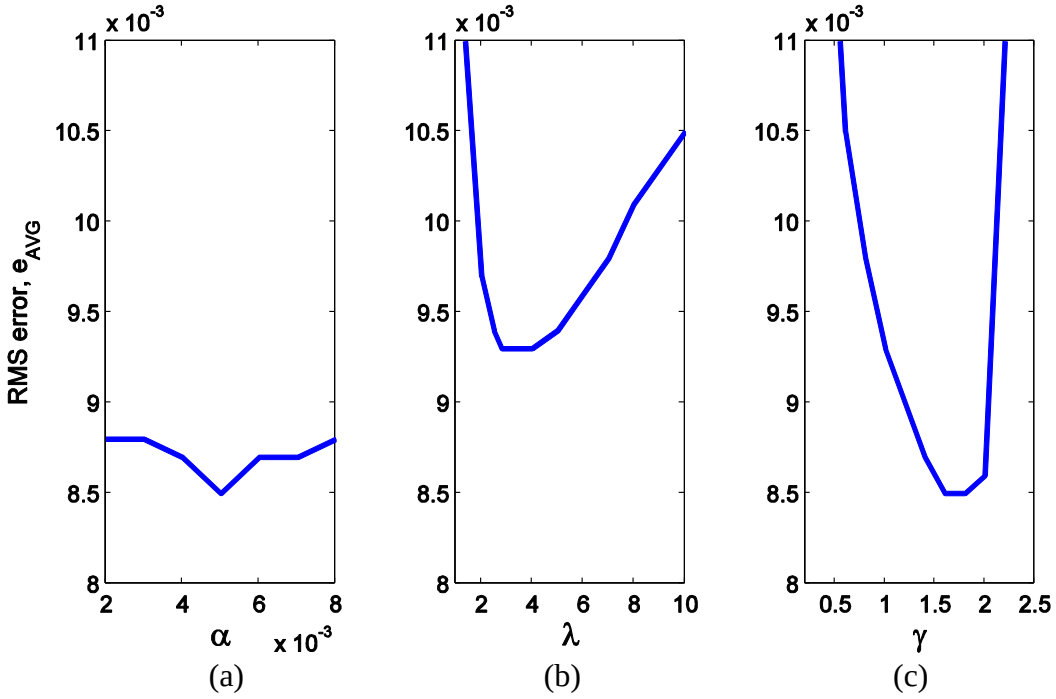

Figure 2-6. Parameter optimization based on RMS error for α (a), λ (b), and γ (c).

These chosen parameters define a neural network that minimizes the target output errors over the entire time interval of the El Centro earthquake (Figure 2-8). When training is on and the weights are updated at each time step, the average normalized RMS error for all degrees of freedom is 0.1824 (Figure 2-7). After the weights have been updated for the entire duration of the earthquake, the final weights are frozen and the neural network predicts the system output acceleration for each floor when subject to the El Centro earthquake. Because the weights are no longer being updated each time step, the neural network prediction is less accurate, with an average normalized RMS error of 0.2712 (Figure 2-7). To further validate the predictive capabilities of the ANN, each floor's acceleration response due to Kobe earthquake and Chi Chi earthquake were also predicted using the weights found through training from the El Centro earthquake. The average normalized RMS error for these two earthquakes were 0.2672 and 0.2578, respectively, thus proving that the weights derived through training the El Centro earthquake were also applicable to other seismic signals.

Therefore, the decentralized VWNN is able to successfully model each floor's acceleration, both for the "training-on" and "training- off" cases. However, the true

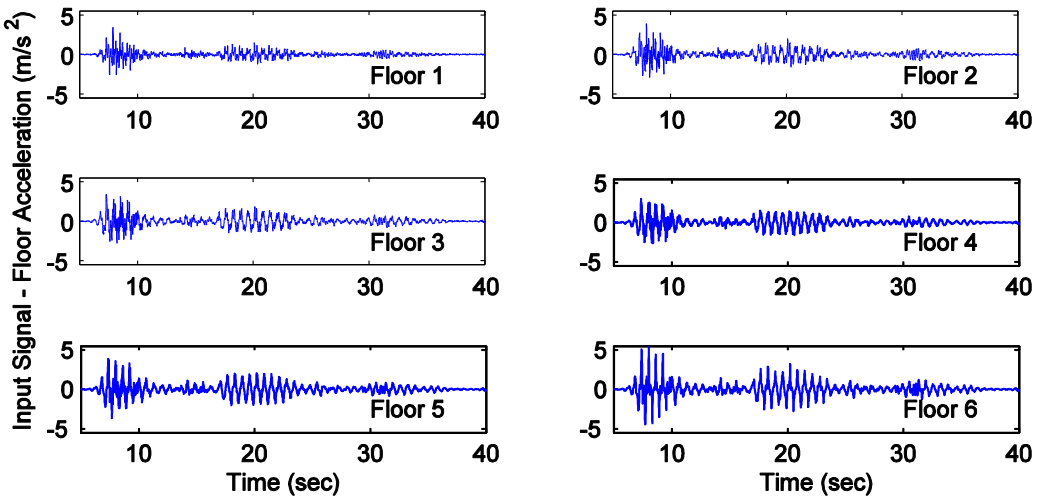

Figure 2-8. Response of six-story shear structure at each floor when subject to El Centro ground motion.

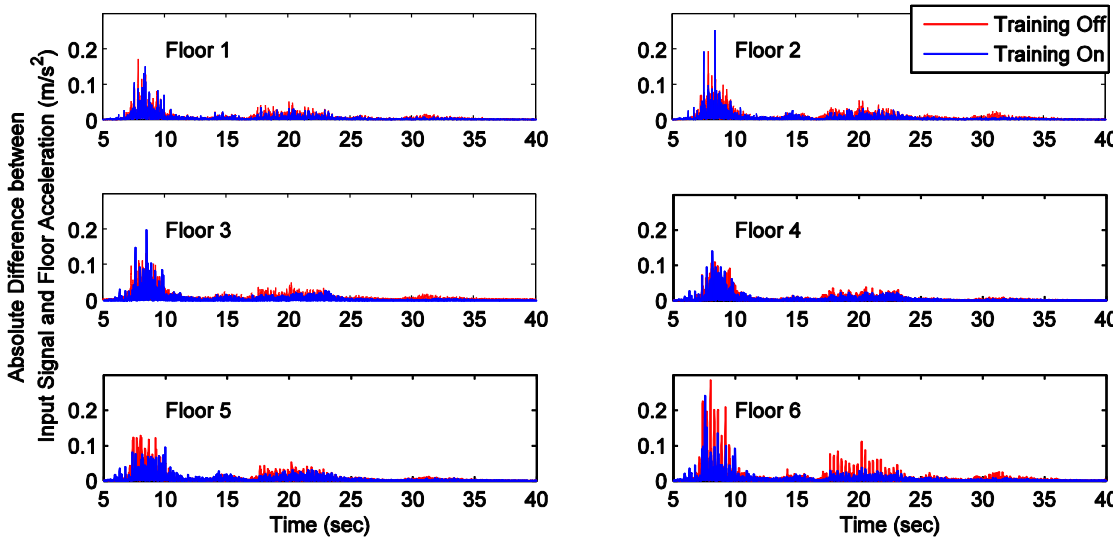

Figure 2-7. Absolute difference between neural network prediction and measured acceleration for both the training-on case and the training-off case when subject to the El Centro ground motion.

success of the decentralized algorithm is demonstrated by the overall time consumed during prediction of the entire acceleration profile. When the entire algorithm is embedded onto a single *Narada*, the computations are slowed by the repetitive matrix computations and during "training-on" mode, a single iteration of the algorithm takes 1.63 seconds. When in "training-off" mode, there are no weighting matrix computations,

Table 2-1. Centralized versus decentralized time consumption for one iteration of the algorithm.

	Training		Execution	
Network	Time consumption (sec)	Energy consumption (mJ)	Time consumption (sec)	Energy consumption (mJ)
Centralized network (one sensor)	1.63	244.5	0.32	48.0
Decentralized network (six sensors)	0.18	328.0	0.16	312.8
Percent difference (between centralized and decentralized)	**89%**	**-34.2%**	**50%**	**-551.7%**

Table 2-2. Breakdown of time consumption of decentralized VWNN tasks for one iteration during "Training-On" mode.

Decentralized task	Time consumption (μsec)	Energy consumption (μJ) per sensing unit
Pre-process data	1 117	168
Threshold evaluation	83 923	12 588
Communication*	151 464	39 381
Output estimation	0	0
Update weighted matrix	16 810	2 522
Total	**178 314 (0.178 sec)**	**54 659 (54.7 mJ)**

*****Radio-on

thus eliminating a majority of the calculations and reducing computational time to 0.32 seconds per iteration (Table 2-1).

Where the centralized algorithm (*i.e.*, the entire VWNN is embedded in a single node) is inhibited by extensive matrix computations, the decentralized implementation attempts to parallelize these computations but at the expense of increased communication. The decentralized algorithm executes one iteration in only 0.178 seconds in “training-on” mode, which is an 89% reduction in computation time when compared to the centralized implementation. If the time consumption of each task is individually evaluated (Table 2-2), it is clear that decentralizing the algorithm is computationally faster as the core tasks (*i.e.*, pre-processing, threshold evaluation, update weight matrix) only require 0.102

seconds (= 0.001 seconds + 0.084 seconds + 0.017 seconds) to complete. This achievement in reduced computational time is slightly diminished by the penalty of an increase in communication costs (using the waterfall communication scheme), which account for 85% of the total time for one iteration of the decentralized algorithm. Even with this extra cost, however, there is still a significant decrease in training time so the decentralization of the algorithm is successful. In execution mode (*i.e.*, "training-off"), the decentralized algorithm performs an iteration in 0.16 seconds, a 50% reduction in time consumption from the centralized algorithm. The elimination of updates to the weighting matrix makes the centralized algorithm more computationally efficient and the communication costs of the decentralized algorithm almost outweigh the benefits gained from parallel computations. Therefore, there is still some benefit in the decentralized algorithm during the "training-off" case but not as significant as the "training-on" case.

In addition to time consumption, the energy consumed during one iteration of the network can be used as a metric for success. The *Narada* is designed such that its power draw is 150mW (30mA at 5V) when the radio is off and 260mW (52mA at 5V) when the radio is on. By default the *Narada* operates with its radio off and the radio is only activated for communication. Thus when the neural network is centralized on one wireless sensing unit and in "training-on" mode, the radio is always off and therefore consumes 244.5mJ of energy (Table 2-1). When the neural network is decentralized across a network of wireless sensor units, the majority of its tasks are executed with the radio off. However, the communication task, which is the most time consuming task, requires the radio to be on. Each wireless sensor unit, therefore, uses 54.7mJ of energy during a single iteration (Table 2-2). Because six sensors are employed for the VWNN computation, this results in a combined energy consumption of 328.0mJ, which is an increase in the energy consumption when compared to the centralized algorithm. In the "training-off" mode, the decentralized algorithm must still include communication between all the units so its energy consumption is 52.1mJ for one iteration of one sensor, resulting in a total consumption of 312.8mJ across the entire network. The centralized algorithm, on the other hand, uses only 48.0mJ of energy per iteration which is significantly less than the decentralized algorithm. Thus, the decentralized algorithm is capable of faster completion of the computations of the neural network by leveraging

parallel processing. However, the decentralized network does see much higher energy consumption due to increased communication costs. As such, if computational speed is a concern for the application of the ANN then decentralizing the algorithm across a network of sensors is the best option. If energy consumption is the largest concern then embedding the algorithm on a single sensing node is optimal. However, if both computational speed and energy consumption are of interest then a hybrid network of sensors should be established in which the training (*i.e.*, updating of weights) is decentralized and the execution is centralized.

2.5. Chapter Summary

This chapter considers the benefits of artificial neural networks as they apply to model prediction of dynamic structures on a wireless sensing network. To achieve this, the VWNN algorithm is embedded onto a network of wireless sensors and is used to predict the accelerations of a six-story shear building subject to the El Centro earthquake, the Kobe earthquake and the Chi Chi earthquake. While significant computational benefits (namely, execution speed) are seen through decentralization of the algorithm, some of these gains are lost to communication costs as information about the neural network is shared across a network of sensors. Additionally, the overall energy consumption of the network is greatly increased when the neural network is decentralized across a network of sensors due to this increase in communication costs. Therefore, to effectively utilize this algorithm, careful consideration must be given to the overall architecture of the network and it must be decided if reduction in time consumption or energy consumption across the WSN is more desirable for the application of interest.

To improve the overall performance of ANNs on WSNs, future work will consider pruning insignificant weighting connections between the hidden layer and the output layer. Researchers have shown that certain weights within ANNs do not have a significant impact on the prediction capabilities of the network and therefore, can be eliminated from the network (Reed 1993). As such, various techniques have been established such as the Optimal Brain Surgeon (Hassibi and Stork 1993) and the Optimal

Brain Damage (Le Cun *et al.* 1990) algorithms, that systematically highlight insignificant weights and remove them from the network. When considering embedment of ANNs on WSNs, by eliminating these connections less information must be communicated across the WSN, which results in an overall reduction in energy consumption. Therefore, future work will consider this as an avenue for increasing the attractiveness of ANNs for WSN applications.

This study explored an ANN as it pertains to wireless sensor nodes. While the ANN does take advantage of parallel processing, similar to its biological inspiration, few other benefits are seen when embedding the algorithm and the current limitations of WSNs nodes, such as power consumption and radio bandwidth, are not adequately addressed. In fact, this study highlighted the high energy costs associated with radio communication as well as the difficulties of optimally utilizing the parallel processing capabilities of the network. As such, a new paradigm of sensing should be explored that deviates from the traditional ANN and is more strongly tied to biological sensory systems if these limitations are to be overcome. The remainder of this thesis focuses on that goal by developing a new method of sensing and actuation that is not directly tied to ANNs but instead attempts to make a stronger tie to the principles employed by biological sensory systems.

CHAPTER 3

UTILIZING THE COCHLEA AS A BIO-INSPIRED COMPRESSIVE SENSING TECHNIQUE

3.1. Introduction

Given that a traditional bio-inspired signal processing technique, artificial neural networks, did not adequately address the current limitations of wireless sensor nodes, the biological sensory system will be re-examined from an engineering perspective. In doing so, a new sensing and actuation paradigm will be established for wireless sensor nodes that can address some of the deficiencies which are currently found in wireless sensor networks (WSNs). When returning to the principles of biological sensory systems, it is evident that these systems, such as the central nervous system (CNS), are capable of compressing, integrating, and processing information in real-time, thereby enabling instantaneous decision making. This is possible because the core processing unit, the neuron, communicates to other units through a highly compressive method by encoding a continuous input signal into a series of single bit electrical pulses (Rieke *et al.* 1999). As a result, large networks of neurons are able to process information at extremely fast rates with minimal energy costs, a characteristic that is highly desirable in engineering sensing systems. This chapter will draw inspiration from the data compression and information transmission techniques employed by biological systems in order to establish a new sensing paradigm for the purposes of structural monitoring and control. In doing this, it is hoped that the new engineered system will be capable of extreme data compression and correspondingly large energy savings, while maintaining real-time processing capabilities.

Engineers have long been interested in data compression techniques for the purposes of energy conservation in WSNs and various methods have been widely explored. Traditional engineering data compression techniques can be classified into two categories: lossless compression and lossy compression (Sayood 2006). In lossless compression, no information is lost in the process of compression and the original signal can be perfectly reconstructed. In lossy compression, some information about the original signal is lost through the compression process and exact reconstruction of the original signal is not achievable. This error in reconstruction, however, is often offset through the achievement of higher compression rates than those associated with lossless compression. For the purposes of structural monitoring, minimal signal distortion is allowable if it results in significant resource savings such as communication bandwidth and battery power; therefore, lossy compression techniques are acceptable. Several researchers have explored the use of various traditional data rate compressive methods for vibratory signals, such as those typically found in structural monitoring applications. The use of wavelet transforms, both with lossless (Lynch *et al.* 2003) and lossy applications (Xu *et al.* 2004; Zhang and Li 2006) have been explored with relative success. Other studies have focused on non-traditional sampling schemes (*e.g.*, asynchronous, sub-Nyquist), such as those afforded by compressed sensing, to reduce the flow of sensor information (Bao *et al.* 2011; O'Connor *et al.* 2012). Still other researchers have explored the use of transform coding schemes, such as the Discrete Fourier Transform or the Karhunum-Loeve Transform, to transmit large amounts of seismic data (Spanias *et al.* 1991). While all of these compression methods result in high compression rates, they are often computationally expensive and require complex post-processing steps, thus detracting from any real-time processing capabilities of the monitoring system.

This chapter proposes a new sensing paradigm for structural monitoring applications that draws inspiration from the sensing and processing capabilities of the biological CNS, with a specific concentration on the compressive capabilities achieved in data transmission. While these techniques can be found universally across the central nervous system, the mammalian auditory system is chosen as a system of interest in this study due to its unique signal processing techniques and real-time spectral decomposition

capabilities. As such, a new approach to data collection and communication in structural monitoring systems is proposed based on the methods employed by the auditory system. Such applications of the auditory system were first proposed by Peckens and Lynch (2012; 2013) and also explored by Elliot and Shera (2012). In this chapter, the properties of the CNS combined with the signal processing capabilities of the auditory system are interpreted from an engineering viewpoint and its functionality is applied to enhance the performance of wireless structural monitoring systems. While the auditory system does exhibit impressive dynamic range compression (Yates *et al.* 1990), this study draws inspiration from the biological system's signal processing capabilities and highly compressed data transmission rates. The first section of the chapter provides an overview of the mechanisms employed by the mammalian cochlea. Next, a bio-inspired sensor is proposed that is based on the functionality of the auditory system and capable of real-time processing while exhibiting impressive data compression rates. Finally, the compressive capabilities of the proposed sensor are compared to two mature compression techniques to quantify its performance. First, a wavelet transform compression method is adapted as a traditional lossy compression method using Nyquist-sampled sensor data. Second, a compressive sensing strategy is also used because it exhibits many common characteristics as the cochlea-based compressive sensing strategy proposed herein including asynchronous signal sampling.

3.2. Mechanisms of the Mammalian Cochlea

The auditory system's ability for real-time spectral decomposition and high compressive capabilities render it an ideal subsystem of the biological sensory system to study for improving the performance and extending the functionality of structural monitoring systems. Researchers have extensively studied the mammalian auditory system and through experimental observation have identified its operational principles. Sound (*i.e.*, a pressure wave) is received in the auditory system at the outer ear, is passed to the middle ear through the ear drum, and is transmitted to the inner ear through induced vibrations at the oval window. This vibration is directly transmitted to the cochlea, the main signal processing unit of the auditory system (Figure 3-1a). The

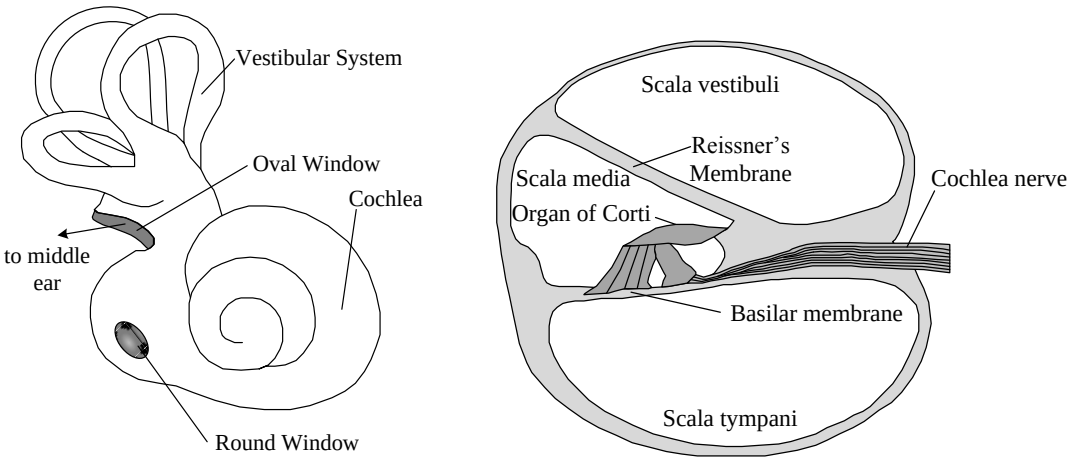

Figure 3-1. Diagram of the mammalian inner ear (a) and a cross-section of the cochlea (b).

cochlea is responsible for translating the perceived stimulus (*i.e.*, sound) to higher levels within the auditory cortex. The cochlea is a thin-walled membrane (approximately 35mm in length) which tightly coils in on itself to form a shape similar to a snail or nautilus. It is comprised of three fluid-filled cavities: the scala vestibuli, the scala media, and the scala tympani, which are separated by two elastic cochlear partitions: the Reissner's membrane and the basilar membrane, respectively (Figure 3-1b). The vibration of the input signal at the oval window produces a pressure change in the scala vestibuli, which induces a deflection of the elastic cochlear partitions and an increased pressure on the scala tympani. Because of this pressure, the scala tympani bows against its boundaries, resulting in an up-down movement of the fluid. Such motion forces deflections in the basilar membrane, which are directly correlated to the external sound wave exciting the membrane and are characterized as (Zweig *et al.* 1976)

$$v_{BM}(x) = P(x)\,Y(x,\omega), \tag{3.1}$$

where $v_{BM}(x)$ is the vertical velocity of the basilar membrane, *BM*, at location x, $P(x)$ is the induced pressure from the fluid movement in the scala tympani and $Y(x,\omega)$ is the admittance of the basilar membrane which depends on its physical characteristics at location x and the angular frequency of the input signal, ω.

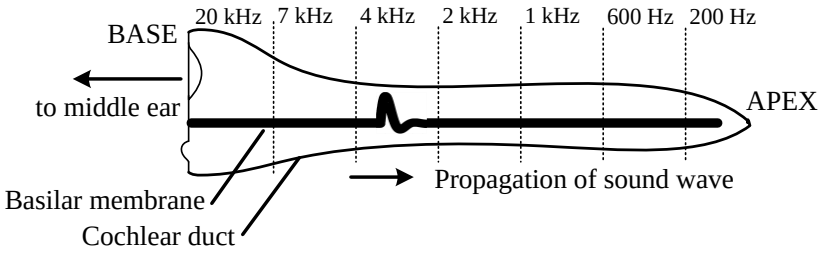

Figure 3-2. Uncoiled cochlea indicating frequency response of the basilar membrane.

The primary function of the basilar membrane is to encode its induced motion, and more specifically its vertical velocity, into electrical spikes which can then be transmitted to the central nervous system. It does this by acting as a hydro-mechanical frequency analyzer, capable of decomposing a sound signal into its frequency components in a spatial manner. Place theory hypothesizes that the auditory cortex maps the location of the basilar membrane response to given frequencies, thus enabling effective time-frequency management of information flow. This is possible due to the unique properties of the basilar membrane. To fully understand the mechanisms of the basilar membrane it will be considered in its passive state. In its active state, the cochlea uses feedback mechanisms to achieve higher precision and sensitivity but these do not significantly change the overall function of the basilar membrane (Dallos 1992). Therefore, for the purposes of this study, it is acceptable to consider the functionality of the basilar membrane in its passive state.

The motion of the basilar membrane in its passive state was first described as a traveling wave by von Békésy (1960) based on observations of a dead cochlea. This theory of motion assumes that a sound wave starts at the base of the cochlea and moves toward the apex. As it traverses the cochlea (Figure 3-2), the amplitude of the response of the membrane changes depending on its location along the basilar membrane and the exact location of largest amplitude depends on the frequency of the input stimulus (Dallos 1996). This theory also assumes that when the wave reaches the apex of the cochlea there is little energy remaining in the signal and therefore, there is no reflection of the sound wave back up the membrane. This reduces the complexity of the model and can therefore be modeled as

$$Y(x,\omega)=\frac{-\frac{1}{i\omega}}{-M(x)\omega^2+i\omega R(x)+K(x)}, \tag{3.2}$$

where $M(x)$, $R(x)$, and $K(x)$ are the basilar membrane's localized mass, damping and stiffness factors, respectively, and i is the imaginary unit.

The mass term is relatively constant across the length of the basilar membrane and can be depicted as a constant value, M_0. It has been shown that the stiffness of the basilar membrane varies nonlinearly across its longitudinal length which results in the frequency dependency of the membrane (Olson and Mountain 1991; Emadi *et al.* 2004). In its simplest form the stiffness term is represented as a decaying exponential,

$$K(x)=S_0 e^{-\alpha x}, \tag{3.3}$$

where S_0 is the stiffness of the membrane at the base and α is the constant controlling the rate of decay. To achieve constant bandwidth in the frequency domain, the resistance of the membrane is often modeled as $e^{-\alpha x/2}$, such that the damping ratio term can be represented as (De Boer 1996)

$$R(x)=\delta\sqrt{M_0 S_0}e^{-\alpha x/2}, \tag{3.4}$$

where δ is the damping constant. Such properties of the basilar membrane lead to a unique response in which sub-sections of the membrane are tuned to specific frequencies that vibrate with large amplitude when presented with that frequency (Figure 3-2). As such, the cochlea effectively creates a map for the auditory cortex in which the frequency content of a signal can be instantaneously determined based on the vibrating sections of the basilar membrane.

The Organ of Corti lies on top of the basilar membrane and is responsible for encoding and transmitting information to the CNS (Figure 3-3). While comprised of a variety of components, each with its own unique role within the auditory system, the inner hair cells (IHCs) play the largest role in transmitting information to auditory nerve

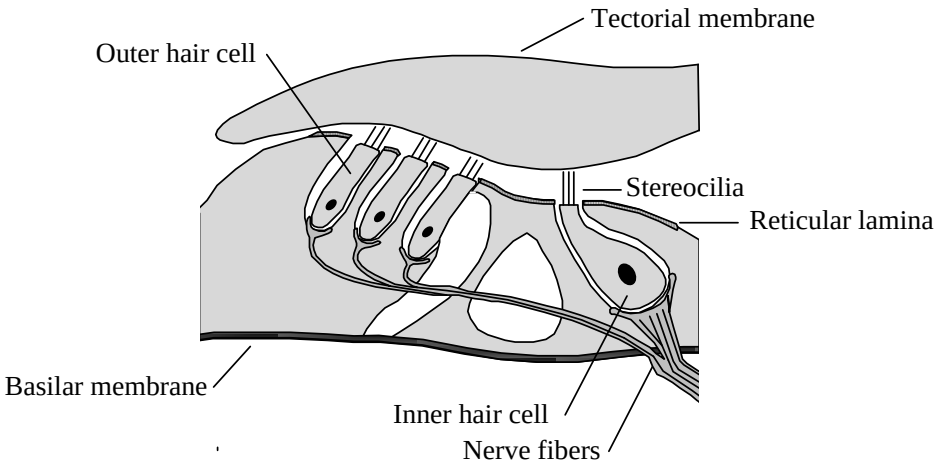

Figure 3-3. Cross section of the Organ of Corti.

fibers (Figure 3-4a, b). Within the human cochlea there are approximately 3,500 IHCs, each responsible for conveying specific information to the CNS. Each hair cell is topped with a bundle of rigid sensory hairs, termed stereocilia, that are cantilevered from the IHC and arranged in a shallow U-shape configuration (Flock and Cheung 1977; Hudspeth 1989). The entire bundle is connected together by a series of fine extracellular filaments termed tip links (Fettiplace and Hackney 2006), thus ensuring uniform rotation of the bundle about its base. Each of the stereocilia are equipped with a mechano-electrical transduction (MET) ion channel which plays a key role in the transmission of information to the CNS.

The motion of the basilar membrane induces movement of ionic fluid that is trapped in the subtectorial space (*i.e.*, the space between the reticular lamina and the tectorial membrane), resulting in deflection of the stereocilia on the IHCs. With this movement, the MET ion channels are opened thus allowing the ionic fluid (comprised of potassium, K^+, and calcium, Ca^{2+}, ions) surrounding the hairs to flow into the cell. With this influx of ions, the cell becomes depolarized and releases a chemical transmitter that initiates a graded potential at the base of the hair cell (Figure 3-4c). As the motion of the basilar membrane subdues the MET ion channels close and the graded potential ends. Therefore, the duration of the graded potential corresponds to the amplitude of response of the basilar membrane. The graded potential is transmitted a short distance down the afferent nerve fiber to the auditory nerve, where its amplitude is encoded into a series of

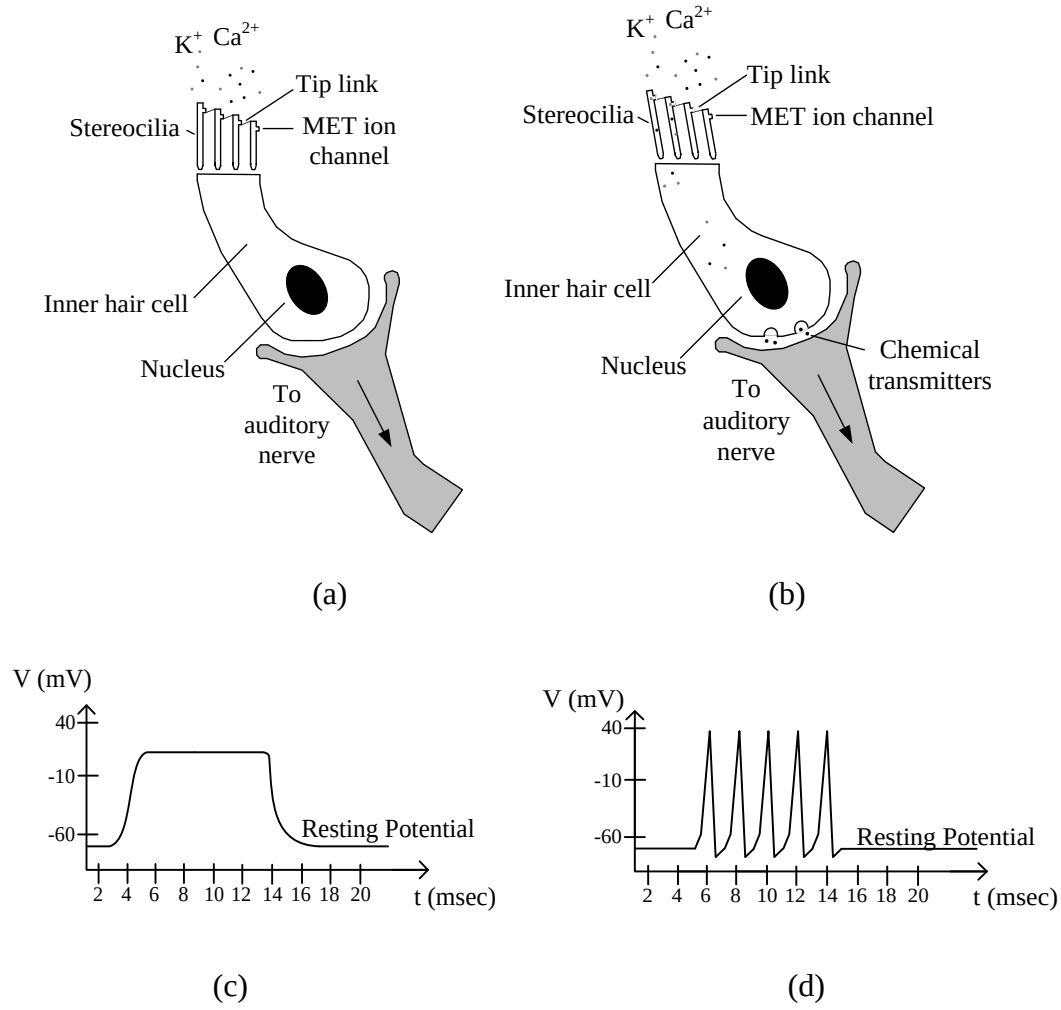

Figure 3-4. Information transmission through inner hair cell; in a stationary state (a) no information is transmitted but when motion activated (b), ionic fluid flows into the cell and releases transmitters to the across the auditory synapse which triggers a graded potential (c) and eventually a series of action potentials (d).

neural spikes whose firing rate is proportional to the velocity of the basilar membrane at the hair cell location (Figure 3-4d) (Yost 2007).

In its most general form, the neural spike train is a series of electrical spikes that encode a perceived stimulus. Each electrical spike is an all-or-nothing event in that the spike will only fire when a threshold stimulus value is reached. Once the threshold is met, the resulting electrical spike has a constant amplitude and duration that is independent of the input stimulus. As a result, the individual spike does not carry information about the stimulus but instead is part of a series of pulses that encode information (Bialek *et al.*

1991). The pulse trains are transmitted down the auditory nerve to the central nervous system where they can be further interpreted and manipulated. Each IHC connects to a unique set of auditory nerve fibers resulting in a finely tuned map of the motion of the basilar membrane (Yost 2007). As a result, the central nervous system is able to determine the frequency of the incoming sound wave based on the activated nerve and also the associated amplitude through the firing rate of the spike train. Therefore, based on analog electro-mechanical transduction, the communication of information from the basilar membrane is more or less real-time (*i.e.*, has near zero delay).

Thus, the auditory system utilizes a unique method of real-time spectral decomposition along with place theory to attain an impressive auditory range while maintaining real-time processing capabilities. It is able to achieve this by acting as a hydro-mechanical frequency analyzer, as well as using compressive techniques to efficiently transmit data. These unique mechanisms can be used as inspiration in overcoming the deficiencies of information inundation and large computational requirements that currently limit existing structural monitoring technologies.

3.3. Representation of the Cochlea as an Engineered System

The unique method by which the auditory system processes and encodes incoming sound waves can serve as inspiration for engineering sensing technologies used in structural monitoring applications. The auditory process is summarized through two main steps: 1) signal decomposition of the basilar membrane and 2) signal encoding of peak values by the inner hair cells. These mechanisms can be translated into a cochlea-inspired sensor system by first passing a vibratory signal through a bank of analog band-pass filters, thus allowing for spectral decomposition of the signal, and then implementing a real-time peak picking algorithm with linear encoding, similar to the function of the IHC (Table 3-1). By employing these methods, the proposed sensor system will be capable of real-time signal compression through minimal processing, similar to that found in the biological CNS.

Table 3-1. Comparison between biological sensory system and engineered sensor system.

Process	Biological System	Sensor System
Frequency extraction from convoluted input signals	Section of basilar membrane	Band-pass filter
Encode magnitude of peak values of filtered signal	Organ of Corti and inner hair cells	Peak-picking algorithm with linear encoding

The inspiring functionality of the basilar membrane is its ability to perform real-time spectral decomposition. Activation of sub-sections of the basilar membrane results in sinusoidal vibrations of varying amplitude and phase, depending on the content of the input signal. As such, the basilar membrane has often been compared to a bank of band-pass filters (BPFs) that simultaneously decompose a convoluted signal into its frequency components (Lyon 1982). Therefore, in the proposed sensor system a unique band-pass filter represents a finite sub-section of the basilar membrane (Equation 3.2), capable of extracting a specific frequency range from an input signal. Each i^{th} filter has a characteristic frequency, ω_i (rad s^{-1}), at the center of its passband and a bandwidth of $2\xi_i\omega_i$, where ξ_i is the damping ratio of the filter. When the filter is presented with a convoluted signal it will only pass signals within its passband and attenuate all others, thus creating a filtered signal with a defined frequency range. Due to the overlap of filters in the filter bank, the engineered system typically does not achieve perfect signal reconstruction. The signal can be better approximated through the addition of more filters in the systems but at the expense of increased information flow in the system. Therefore, a balance must be found between maximizing the number of filters in the bank so as to minimize the reconstruction error, while minimizing the information flow so as to minimize energy consumption in the system.

When passing a signal through a bank of band-pass filters it is desired for the sum of the output of all of the band-pass filters to be a close approximation of the original input signal, thus resulting in minimal distortion upon reconstruction,

$$y(t) = \sum_{i=1}^{N} y_i(t) \approx u(t), \tag{3.5}$$

where $u(t)$ is the input signal, $y(t)$ is the reconstructed signal, $y_i(t)$ is the output of the i^{th} filter and N is the number of filters in the filter bank. The output of the i^{th} filter can be found by convolving the input signal, $u(t)$, with the impulse response of the i^{th} filter, $h_i(t)$, where

$$y_i(t) = \int_0^t u(\tau) h_i(t-\tau) d\tau \tag{3.6}$$

and

$$h_i(t) = -2\xi_i\omega_i \left(\sqrt{1-\xi_i^2}\right)^{-1} e^{-\xi_i\omega_i t} \sin\left(\omega_i\sqrt{1-\xi_i^2}\,t-\theta\right) \tag{3.7}$$

with

$$\theta = \tan^{-1}\left(\xi_i^{-1}\sqrt{1-\xi_i^2}\right). \tag{3.8}$$

Three variables can be optimized across the filter bank to result in more accurate signal reconstruction: the number of filters, the bandwidth of each filter, and the spacing of each filter. While the mammalian auditory system can perceive signals in the frequency range of 20 to 20kHz (Robles and Ruggero 2001), this range is not needed in many monitoring systems, especially those used to monitor large-scale civil infrastructure systems. The input signals for the proposed cochlea-inspired sensor system will be low-frequency vibratory signals (< 20Hz) such as those associated with earthquakes or structural vibrations; the filter bank is designed, therefore, for optimal reconstruction of such signals in this desired frequency range.

Prior to designing the filter bank for vibratory signals, the second step of the auditory system, which includes encoding the stimulus into electrical spikes, must be considered in order to assess the compressibility of information flow across the system. In the auditory system, Avissar *et al*. (2007) showed that action potentials are phase locked with the input signal, which results in neurons firing with a higher probability and at a higher rate on the peaks of a sinusoidal input signal, or sound wave. Similarly, the

cochlea-inspired sensor system will only encode the peak values of the incoming signal, resulting in a large reduction in the overall amount of transmitted data. While the biological auditory system relies primarily on chemical processes to activate spike trains, the cochlea-inspired sensor system will instead utilize a real-time peak-picking algorithm to invoke data transmission. Once a local peak is detected, the magnitude of this peak is linearly encoded into an electrical spike train (*i.e.*, multiple spikes adjacent in time). When a peak value is detected the cochlea-inspired sensor system emits four spikes with the magnitude of the detected peak encoded in the delay between successive spikes. In turn, a centralized repository receives and decodes the pulse trains into peak values by using the timing between successive spikes. Four spikes are used to allow for redundancy in the event that a spike is lost during transmission. Due to the mechanisms involved in the process, the biological system typically fires a spike train at a maximum rate of 1000Hz, or one spike every 1msec (Nicholls *et al.* 2001). Therefore, the upper limit of the firing frequency of the cochlea-inspired sensor system is chosen as 1000Hz. To eliminate large delays at the receiving station, the minimum firing frequency is chosen to be 500Hz resulting in a maximum delay of 6msec for any peak value when waiting to receive four spikes. Ideally, peaks are detected by the cochlea-inspired sensor system at approximately twice the characteristic frequency of any filter. As such, to prevent overlap between two consecutive 4-pulse trains, the maximum allowable characteristic frequency of the filter bank is limited to 80Hz, resulting in detected peaks every 6.3msec. If higher filter frequencies are required then the minimum firing rate can be increased. Additionally, should larger amplitude dynamics be recorded, these firing rates can be elevated to higher levels.

The encoded spike trains are transmitted to a centralized receiving station where the original input signal can be reconstructed through a decoding process. The entire process is demonstrated in Figure 3-5 where the cochlea-inspired sensor system decomposes and encodes the input signal and a less resource constrained centralized repository reconstructs the signal. The success of the decomposition and encoding process are determined through two measurements: the reconstruction error, *e*,

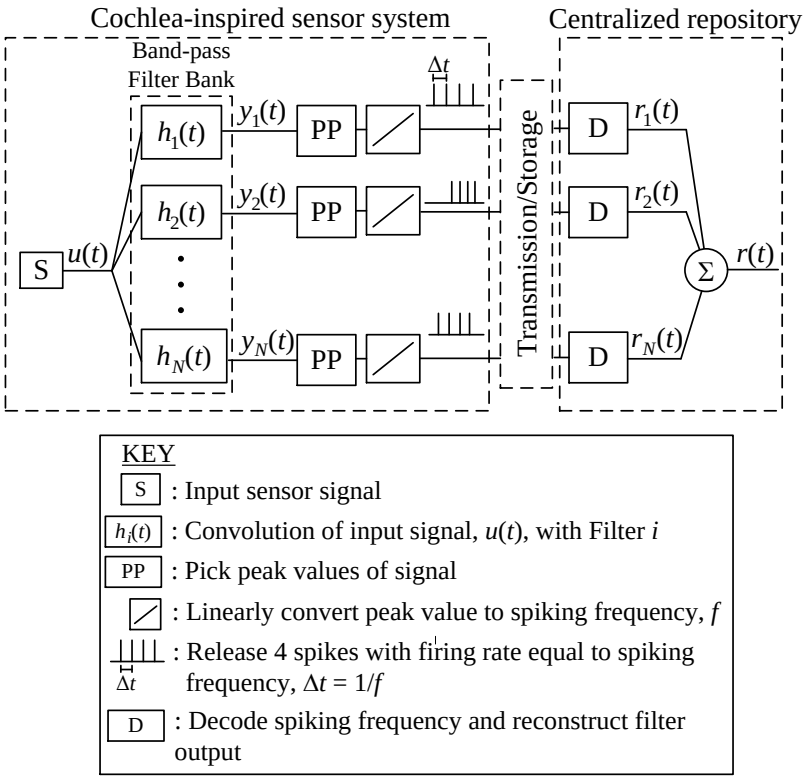

Figure 3-5. Schematic of cochlea-inspired sensor system.

$$e = \frac{\|u(t) - r(t)\|}{\|u(t)\|}, \tag{3.9}$$

where $\|\cdot\|$ is the l_2-norm and $r(t)$ is the reconstructed signal after encoding and decoding, and the compression ratio, *CR*,

$$CR = 1 - \frac{NB_C}{NB_S}, \tag{3.10}$$

where NB_C is the number of bits (spikes) used to represent the signal in its compressed state and NB_S is the number of bits used to represent the original input signal via traditional analog-to-digital converter based data acquisition at Nyquist rates. A compression ratio close to 1 indicates that the cochlea-inspired sensor system achieves high compression while a value close to zero indicates poor compressive performance of the proposed method. These two performance metrics (*i.e.*, *e* and *CR*) compete against each other because as the number of filters in the system increases the reconstruction

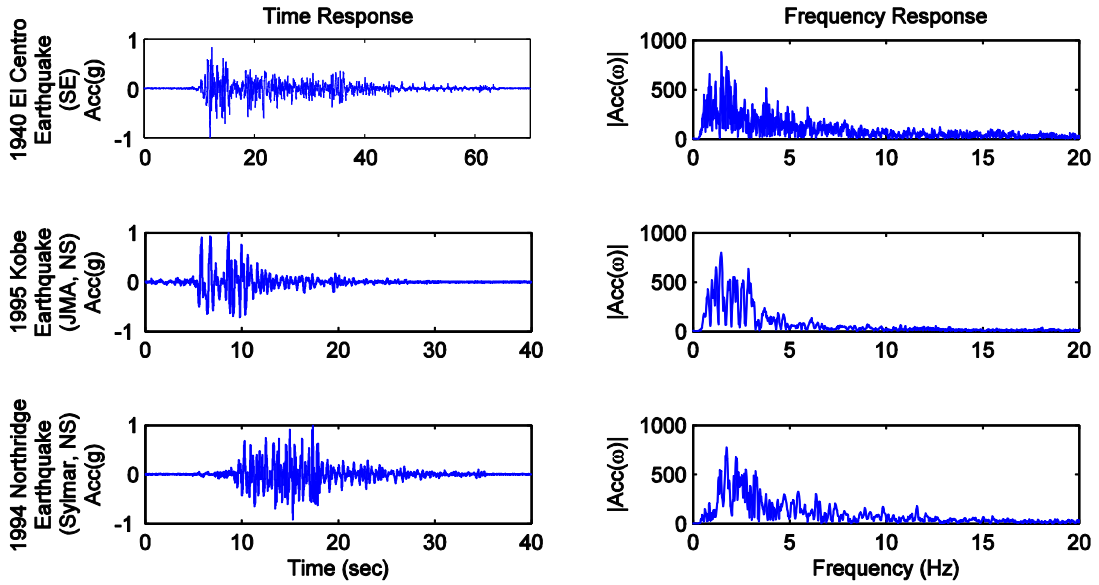

Figure 3-6. Input signals used in time domain filter bank optimization.

error decreases but more information is transmitted and therefore the compression ratio also decreases. Conversely, using too few filters will result in a large compression ratio but also a large reconstruction error. Therefore, a balance must be found between allowable information loss and acceptable (desired) compression rates.

3.3.1. Customization of the Cochlea-Inspired Sensor System for Infrastructure Monitoring

The reconstruction capabilities of the band-pass filter bank are extremely dependent on the input signal and therefore, must be tuned according to the constraints of the application. Because this study is focused on structural monitoring and control applications, the filter bank will be tuned to common signals found in these applications: pure seismic excitations and structure response to such seismic events. Three common earthquake signals will be used as ideal signals during the optimization (1940 El Centro (SE), 1995 Kobe (JMA, NS), and 1994 Northridge (Sylmar County Hospital, NS) earthquakes) all normalized to ±1g peak ground accelerations (PGAs) (Figure 3-6). These earthquakes were chosen because they are fairly representative of large seismic events of potential concern in structural monitoring applications.

As previously mentioned, the design of the filter bank relies on three variables: the number of filters in the filter bank, the bandwidth of the filters (which is assumed to be constant for all filters) and the spacing of the filters (which is assumed to be constant across the entire bank). Increasing the number of filters will always decrease the reconstruction error but also decrease the compression rate. Therefore, this variable was held constant and multiple optimizations (with variations in bandwidth and filter spacing) were conducted. Because the reconstruction is signal dependent and the desired input signals are seismic events that cannot be easily represented in analytical form, a greedy search algorithm (Black 2005) was used to determine the optimal filter bank configuration based on minimizing the objective function, *J*, for the parameters filter bandwidth and filter spacing. The objective function is defined as the minimal reconstruction error ratio of all three earthquakes,

$$J = \left[\frac{\|u_{EC}(t)\text{-}r_{EC}(t)\|}{\|u_{EC}(t)\|} + \frac{\|u_K(t)\text{-}r_K(t)\|}{\|u_K(t)\|} + \frac{\|u_{NR}(t)\text{-}r_{NR}(t)\|}{\|u_{NR}(t)\|}\right] \cdot \frac{1}{3}, \\ = [e_{EC} + e_K + e_{NR}] \cdot \frac{1}{3} \tag{3.11}$$

where u_X is the original signal, r_X is the cochlea-inspired sensor process, and the subscript index *X* corresponds to the El Centro (*EC*), Kobe (*K*), and Northridge (*NR*) earthquakes. Once the minimum reconstruction error for all three earthquakes, *J*, was determined for a variety of number of filters then the optimal configuration was then chosen based on achieving a balance between reconstruction error and the resulting compressibility averaged across all three earthquakes, CR_{AVG},

$$CR_{AVG} = \frac{CR_{EC} + CR_K + CR_{NR}}{3}. \tag{3.12}$$

It should be noted that when implementing the peak picking algorithm, minimum detected peak values were limited to values of ±0.005g to decrease compression ratios without significantly inhibiting reconstruction capabilities.

For the greedy search algorithm, the optimization variables are bandwidth (bounded between 0.01 and 1.0Hz, in 0.01Hz increments) and filter spacing (bounded

between 0.1 and 1.0Hz, in 0.05Hz increments), thereby creating 1,900 possible solutions. The algorithm was initialized with random initial conditions for both bandwidth and filter spacing and the total reconstruction error, *J*, for all three earthquakes at this point was calculated. Next, the reconstructed errors of the 48 nearest neighbors of the point (including diagonals) were considered and the neighbor with the smallest reconstruction error was chosen as the point of interest for the next iteration. This continued until a minimum value was found. This optimization was run twice for a defined number of filters using two distinct initial conditions to ensure convergence to the optimal solution from various starting locations. As can be seen by the optimization plane of 11 filters (Figure 3-7), there is a global minimum within the boundaries of the optimization. However, small localized minima (within 1% of optimal solution) do occur near the optimal solution, which can prematurely end the greedy search algorithm. By increasing the number of neighbors within the search algorithm, a larger footprint is considered and these localized minima can be bypassed.

The greedy search algorithm was applied over an incremented number of total filters in the filter bank (Figure 3-8). From this analysis it can be seen that there is a large drop in reconstruction error when increasing from 13 to 14 filters but only a minimal drop when increasing from 14 to 15 filters. Therefore, 14 filters is chosen as the optimal number of filters, with a bandwidth of 0.53Hz and a uniform filter spacing of 0.7Hz (Figure 3-8b, Figure 3-9). This resulted in a compression ratio, CR_{AVG}, averaged across the three input signals of 0.8788 (or 12.12% of the original content was transmitted) and a cumulative reconstruction error ratio of 0.4174.

To demonstrate the behavior of the band-pass filter bank, consider the El Centro earthquake as an example input signal. The signal is passed through the filter bank and each filter decomposes the signal according to its characteristic frequency (Figure 3-10). As the signal is passed through the filter bank, the output of each filter is read by two different processing units: one that only considers positive values of the filter output and one that uses only negative values of the filter output. Two processing units are used to analyze peaks to achieve higher resolution in the encoding process. Each processing core detects peak values in real-time and once detected, linearly encodes the value into a spike train which is transmitted to a centralized location (Figure 3-11); all filters follow this

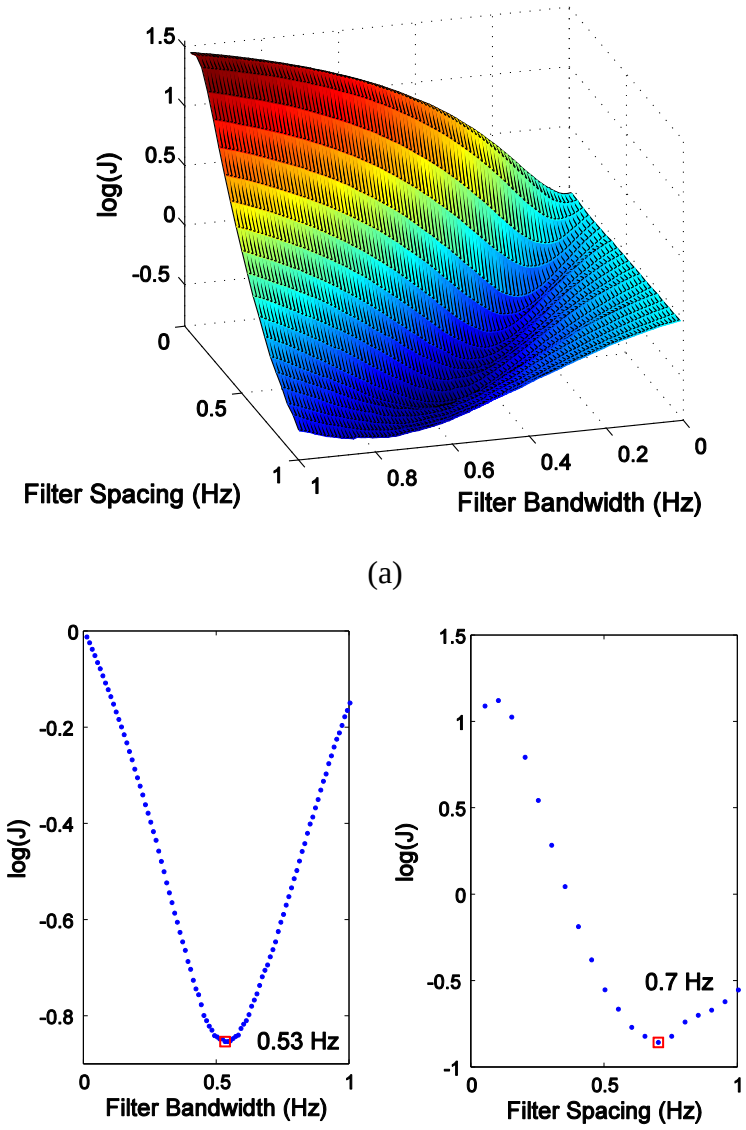

Figure 3-7. Optimization plane (using total reconstruction error, *J*) for a filter bank with 11 filters (a), cross-section of plane at filter spacing equal to 0.7Hz (b), and cross-section of plane at filter bandwidth equal to 0.53Hz (c).

protocol. For the El Centro record, this results in 6,815 detected peak values, or 28,048 transmitted bits of information (= 7,012 peaks x 4 spikes/peak x 1 bit/spike) (Table 3-2). If the original signal was sampled at the traditional 200Hz and transmitted as integer values output by a traditional 16-bit ADC, 13,001 2-byte (16 bits) values would be sent, or 208,016 bits. Thus, by encoding the information into binary spike trains, the amount

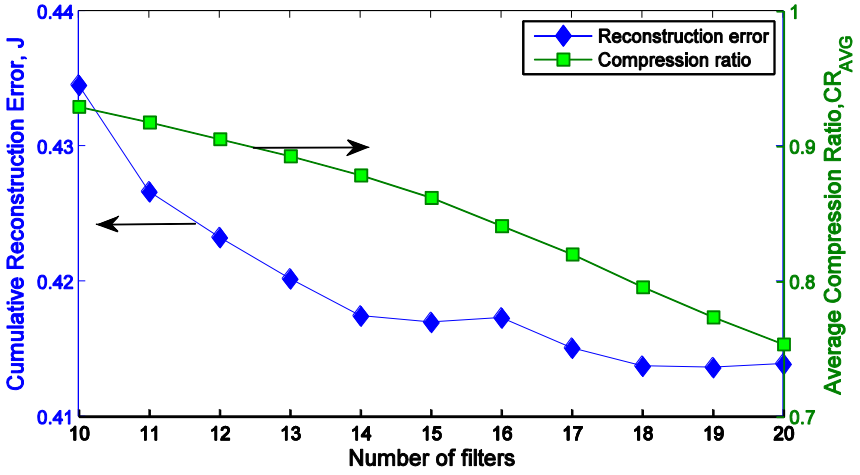

(a)

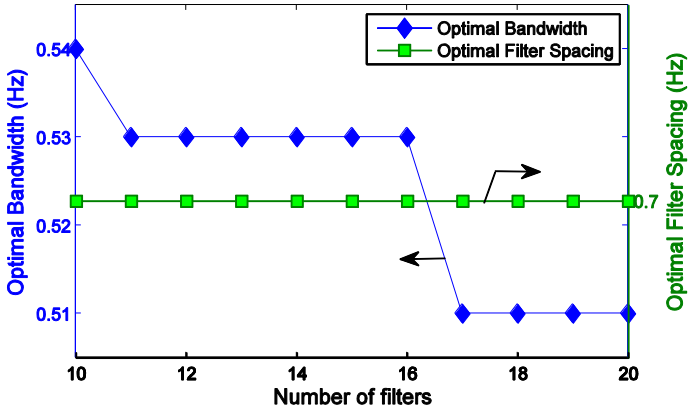

(b)

Figure 3-8. Optimization of number of filters based on reconstruction error and compression ratios (a) with associated optimal bandwidth (Hz) and filter spacing (Hz) (b).

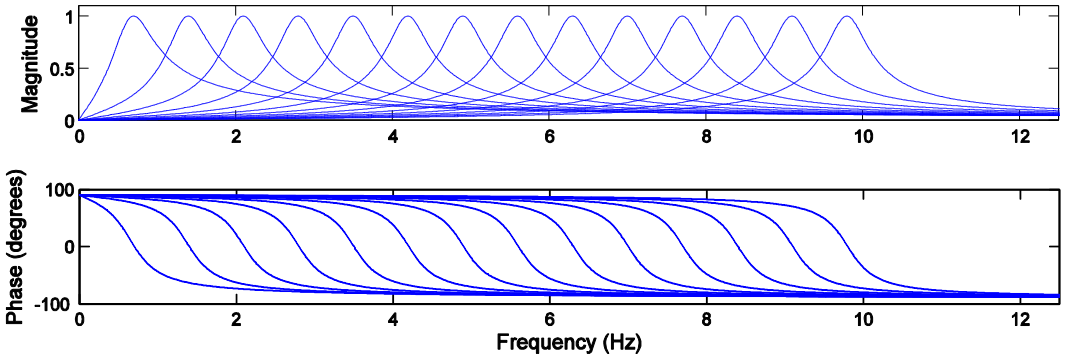

Figure 3-9. Frequency response of optimal filter bank (14 filters with 0.53Hz bandwidth and 0.7Hz uniform spacing).

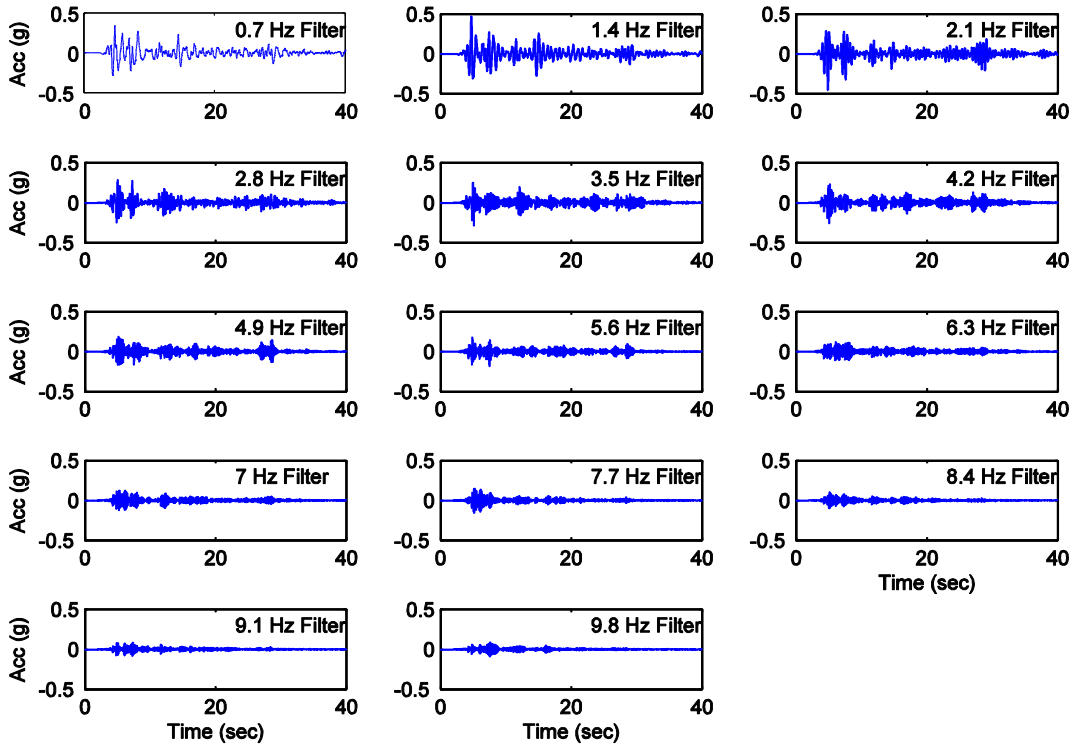

Figure 3-10. Frequency decomposition of El Centro earthquake using filter bank (14 filters with 0.53Hz bandwidth and 0.7Hz uniform spacing).

Table 3-2. Reconstruction error and compression rates for the optimal number of filters, 14 filters.

Input Signal	# of bits for input signal, NB_S	# of bits for encoded filter bank, NB_C	Compression ratio, *CR*	Reconstruction error, *e*
El Centro EQ	208 016	28 048	0.134	0.4860
Kobe EQ	128 016	12 808	0.100	0.3585
Northridge EQ	128 016	16 480	0.129	0.4078

of data flow was reduced to a ratio of 0.866 (or 13.4% of original content was transmitted) with a reconstruction error of 0.486 (Figure 3-12a, b). This process can be repeated for a variety of vibratory signals (including Kobe and Northridge earthquakes, Figure 3-12c-f), resulting in high compression rates without significant signal degradation.

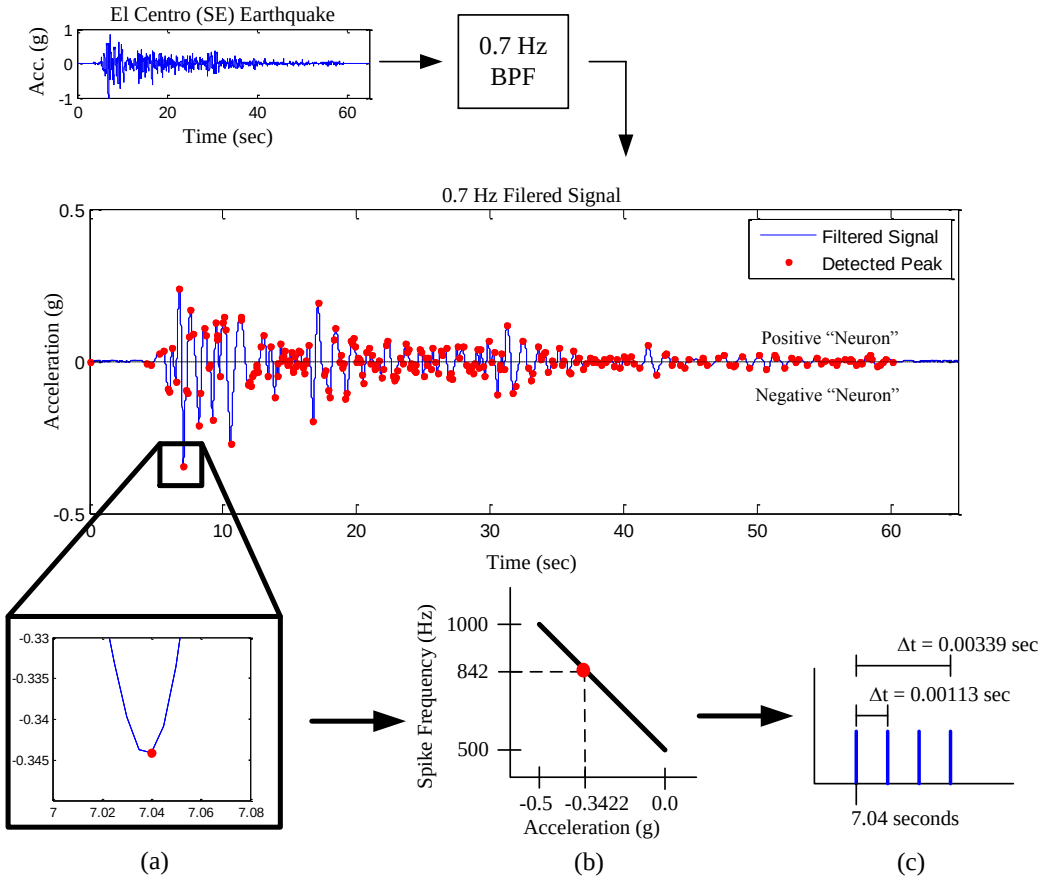

Figure 3-11. Cochlea-inspired data compression: peak picking (a), linear encoding (b) and data transmission at spike trains (c).

3.4. Alternative Data Compression Techniques

Several other techniques have been used for data compression in structural monitoring applications. These have included, but are not limited to, wavelet transforms and compressed sensing. Both methods have had success in such applications but are computationally expensive and can generally not be implemented in real-time. To fully assess the success of the cochlea-inspired sensor system, its performance is compared against the performance of the wavelet transform and compressed sensing methods which have been previously used for lossy compression of vibratory signals. Two vibratory signals will be used in the comparison of the three compression techniques, thus highlighting the performance of the cochlea-inspired sensor system. These signals

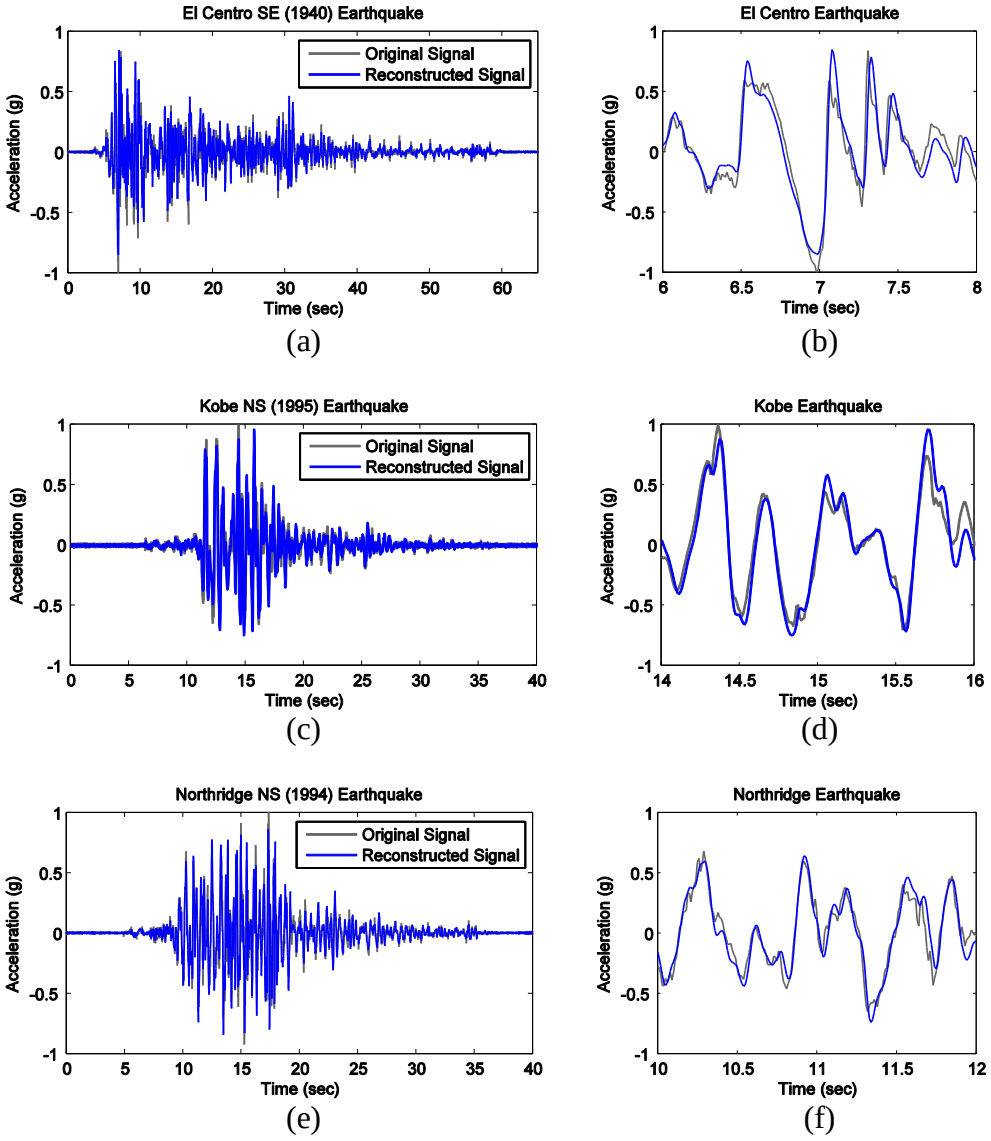

Figure 3-12. Signal reconstruction after passing through cochlea-inspired system for the El Centro earthquake, shown on a full time scale (a) and a sub-section of time (b), the Kobe earthquake, shown on a full time scale (c) and a sub-section of time (d), and the Northridge earthquake, shown on a full time scale (e) and a sub-section of time (f).

include an earthquake signal (chosen as the El Centro earthquake) and the response of a single degree-of-freedom structure (with natural frequency of 4Hz and damping ratio of 5%) subject to the earthquake signal (Figure 3-13). Note that both signals have a duration of 65 seconds and therefore, would result in 13,001 2-byte values if acquired using traditional Nyquist sampling (at 200Hz sampling frequency).

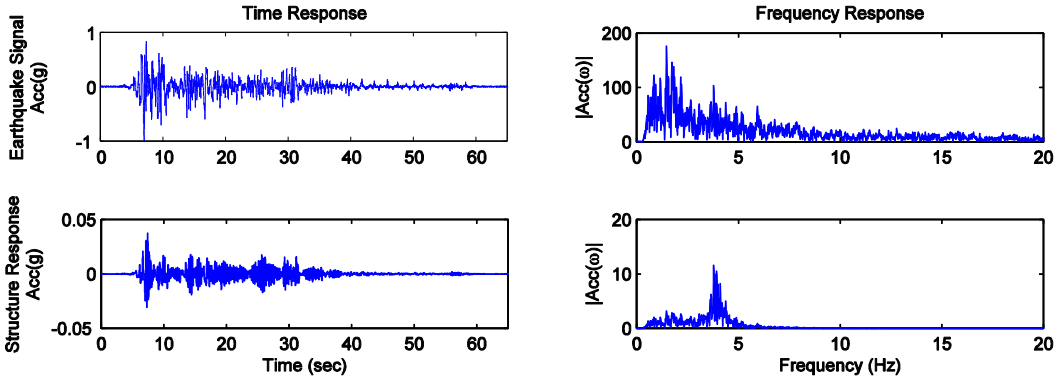

Figure 3-13. Vibratory input signals used in compression analysis.

3.4.1. Wavelet Compression

The construction of the wavelet transform lends itself well to high data compression in vibratory signals. All wavelet transforms are based on a single parent wavelet that serves as a basis function, with all other generations of wavelets derived from this parent through translation or scaling (Daubechies 1992). This creates a multi-resolution (in time and frequency) basis from which the input signal can be characterized. Through this representation, the resulting wavelet coefficients quantify the strength of a wavelet at a specific location and scale. As a result, small valued coefficients can typically be removed from the analysis without losing significant information about the original signal, thus enabling compression of the original signal.

In this study, the discrete wavelet transform (DWT) is used. The DWT is based on a pyramidal algorithm that decomposes a signal using successive steps of low- and high-pass filtering and down-sampling, thus resulting in multi-resolution of both time and frequency (Mallat 1989). At the first step of the algorithm, the signal is decomposed into two sub-bands through convolution with the scaling function (or low-pass filter), $\varphi[n]$, and the orthogonal wavelet function (the scaling function's conjugate filter), $\psi[n]$. For each level of decomposition, j, both functions are dilated by a factor of 2 from the subsequent level, resulting in an orthonormal basis of family functions. Therefore, when an input signal is convolved with the dilated filters, the signal's resolution is downsampled by 2 from the previous decomposition. This step ensures that extra data is

not created through the decomposition. The discrete approximation coefficients at the j^{th} decomposition level, or the low frequency components, of an input signal, $u(t)$, are found through convolution with the dilated and scaled scaling function and are represented as, $a_j[n]$,

$$a_j[n] = \sum_{k=0}^{K} u[k\Delta t]\varphi_j[n-k] \tag{3.13}$$

where K is the length of $u(t)$ when sampled at an interval Δt. Conversely, the signal detail coefficients at the j^{th} decomposition level, or the high frequency components, of an input signal are found through convolution with the dilated and scaled wavelet function and are represented as, $d_j[n]$,

$$d_j[n] = \sum_{k=0}^{K} u[k\Delta t]\psi_j[n-k] \tag{3.14}$$

For all subsequent steps, the newly constructed sub-band containing the approximate coefficients, $a_j[n]$, is further decomposed into the next level of approximate and detail coefficients. This continues until a desired resolution in the frequency domain has been met or until computational resources have been exhausted. At this point, if J iterations of the decomposition have occurred then the signal is decomposed into J sub-bands of detail coefficients ($d_1[n]$, …, $d_J[n]$) and one sub-band of approximate coefficients, $a_J[n]$. The algorithm is typically implemented as a post-processing technique on a signal that is acquired through Nyquist uniform sampling. A more in-depth overview of the method can be found in Mallat (1989; 2008).

To compress the original signal, small valued wavelet coefficients (both detail and approximate) can be removed without losing significant information and as such, all coefficients below a specific threshold are considered to be zero terms and are removed from the decomposed signal. However, in order to reconstruct the signal, it is imperative to know the index of the zeroed coefficients and therefore, an encoding map similar to one proposed by Shapiro (1993) must also be included in the transmission. The map is a binary representation of the wavelet coefficients with a one indicating that the coefficient was above the threshold and zero representing a zeroed coefficient. As such, the total

achieved compression of the wavelet transform must include the non-zero wavelet coefficients plus the encoding map.

To best capture the non-linearities of the input signal, while maintaining an orthogonal wavelet family, a high-order Daubechies wavelet transform was used. The transform was chosen as Daubechies-24 (D24), yielding 24 non-zero coefficients, because it is able to represent high-order polynomials with reasonable accuracy and therefore, can capture the rapid fluctuations of the earthquake signals. The scaling function for the Daubechies wavelet transform in its general form is

$$\varphi_j[n]=\sum_{k=0}^{M-1} c_k \varphi_{j+1}[2n-k] \tag{3.15}$$

where M is the specified number of nonzero coefficients for the chosen Daubechies transform and c_k are the associated coefficients. Further details on the wavelet and the derivation of the coefficients can be found in Daubechies (1988). The wavelet function is given by

$$\psi_j[n]=\sum_{k=0}^{M-1} (-1)^k c_{M-1-k} \varphi_{j+1}[2n-k] \tag{3.16}$$

Using this wavelet transform, the two input signals were analyzed for compressibility and reconstruction capabilities. The wavelet transform can be compressed to large extremes with minimal reconstruction error but at the expense of computational time.

For comparison, the compression of the D24 was limited to the compression achieved by the cochlea-inspired sensor system. The threshold value of the wavelet transform was set to retain only 7.25% of the wavelet coefficients (or 0.9275 compression ratio), therefore leaving 1,040 two-byte values (of the original 13,001 two-bytes values), or 16,640 bits of data. In addition to these coefficients, the reconstruction also requires an encoding map which consists of 13,001 one-bit values. As a result, 28,082 bits of data are transmitted which is 13.5% of the original 208,016 bit information flow, or a compression ratio of 86.5%. For the structure response, however, the compression ratio achieved by the cochlea-inspired sensor system cannot be maintained

by the wavelet transform because of the inclusion of the encoding map which requires a minimum of 13,001 bits or 6.25% of the uncompressed data signal. Therefore, the reconstruction error of the wavelet transform was designed to match the reconstruction error (within 1%) of the cochlea inspired sensor system by varying the compression ratio. This resulted in a total compression ratio of 0.9007.

3.4.2. Compressive Sensing using Fourier Basis Functions

A second form of compressive data transmission that has been explored for structural monitoring applications is compressive sensing (CS), which relies on asynchronous sampling techniques to remove redundant or insignificant data (Donoho 2006). CS proposes a new paradigm in data collection that strays from the traditional uniform Nyquist sampling rate by instead collecting data at random intervals so as to better utilize available resources and reduce the amount of data flow. It is this combination of front-end, non-traditional sampling paired with compression techniques that shares strong similarity to the proposed cochlea-inspired sensor system. Recently, researchers have shown that if a signal is sparse, or compressible, with respect to a specific basis it is possible to represent the signal through an incomplete representation of that basis with minimal reconstruction error (Candès and Tao 2005; Candès *et al.* 2006; Donoho 2006). This study only touches on the derivation and application of CS; a more thorough overview is provided by Candès and Wakin (2008).

Suppose there is an unknown signal, $x \in \mathbb{R}^n$, that is *k*-sparse (*i.e.*, it has $k << n$ nonzero entries) with respect to a specific basis. The signal can be approximated through a small number, *m* (where $k < m << n$), of linear measurements, $y \in \mathrm{R}^m$, such that

$$y_i = \langle x, \phi_i \rangle, \quad i = 1, \ldots, m \tag{3.17}$$

or

$$y = \Phi x, \tag{3.18}$$

where $\Phi \in \mathrm{R}^{m \times n}$ is the measurement matrix with the i^{th} row of the matrix represented by the linear basis vector $\phi_i \in \mathrm{R}^n$. Because the number of measurements is smaller than the number of samples in the original signal, solving for the unknown signal becomes an ill-

posed problem with infinite solutions. If, however, x is sparse within a known basis then an exact or approximate recovery is possible by solving a l_1-norm convex optimization problem. For a signal with noise, σ (*i.e.*, $y = \Phi x + \sigma$), the solution to

$$\min_{\tilde{x} \in \mathrm{R}^n} \|\tilde{x}\|_1 \text{ subject to } \|\Phi\tilde{x} - y\| \leq \varepsilon \tag{3.19}$$

reconstructs x, where $\tilde{x}$ is the approximation of the original signal, ε is a bound on the amount of noise in the signal measurement, $\|\cdot\|_1$ is the l_1-norm and $\|\cdot\|$ is the l_2-norm.

A necessary condition to achieve a good approximation of x is when Φ meets the restricted isometry property (RIP) (Candès and Tao 2005). A matrix obeys the RIP of order s when the isometry constant, δ_s, is the smallest value that satisfies

$$(1-\delta_s)\|x\|^2 \leq \|\Phi x\|^2 \leq (1+\delta_s)\|x\|^2 \tag{3.20}$$

for all (s/2)-sparse $x \in \mathrm{R}^n$. Thus, to acquire k-sparse signals, a small restricted isometry constant δ_{2k} is sought with as few samples as possible, where $s = 2k$ in Equation 3.20. Random Gaussian matrices, random Bernoulli matrices, and partial Fourier transform matrices have been shown to satisfy RIP conditions with high probability (Candès and Wakin 2008) on the condition that an appropriate number, m, of linear measurements are obtained. The number of required measurements is dependent on the basis used for the measurement matrix. For this study, the Fourier coefficients of an unknown signal are approximated through asynchronous random sampling of an input acceleration signal. As such, the measurement matrix is comprised of entries of the partial inverse Fourier transform and the number of measurements, m, should exceed (Needell and Tropp 2009)

$$m \geq C \cdot k \cdot \log^5(n) \cdot \log(\varepsilon^{-1})\varepsilon^{-2} \tag{3.21}$$

where C is a positive universal constant and $\delta_{2k} \leq \varepsilon$.

The CoSaMP algorithm, as proposed by Needell and Tropp (2009), is used for signal reconstruction. This algorithm is based on an iterative greedy pursuit of a near-optimal solution. In the CoSaMP algorithm the desired compression rate, or assumed sparsity level, is an input to the algorithm and therefore, is always fixed. As such, the

Table 3-3. Comparison of cochlea-inspired sensor system to traditional compressive techniques.

Input Signal	Performance Metric	Cochlea-Inspired Sensor System	'Daubechies' Wavelet Transform (D24)	Compressed Sensing (CS)
Earthquake Signal	Normalized Reconstruction Error, J	0.504	0.239	0.756
	Compression Ratio, CR_{AVG}	0.865	0.865	0.865
Structure Response	Normalized Reconstruction Error, J	0.299	0.300	0.307
	Compression Ratio, CR_{AVG}	0.988	0.901	0.880

compression rate was assigned based on the rates achieved by the cochlea-inspired sensor system. The chosen input signals, however, may only have modest sparsity in the frequency domain and therefore, when using CoSaMP, better approximations of the input signals may be achieved if the compression constraint is relaxed. The earthquake signal is considered as an example which as previously mentioned is described by 13,001 two-byte values (or 208,016 bits) in its uncompressed state. When considering CS, however, compression rates are clearly defined by a sub-Nyquist random sampling scheme and therefore, a compression ratio of 0.865 is achieved by sampling 1,820 2-byte values (of the original 13,001 two-byte values), or 28,082 bits of data. Again, when considering compression for the structural response, the CS algorithm is unable to achieve the high compression ratios seen in the cochlea-inspired sensor system and therefore, the normalized reconstruction error is matched, while varying the compression ratio, resulting in a compression ratio of 0.880.

3.5. Results

The reconstruction capabilities and the compressibility of the two established compression techniques are compared to the cochlea-inspired sensor strategy (Table 3-3). When considering a convoluted signal, such as the earthquake signal, the cochlea-inspired sensor is able to achieve high compression ratios but it incurs more error

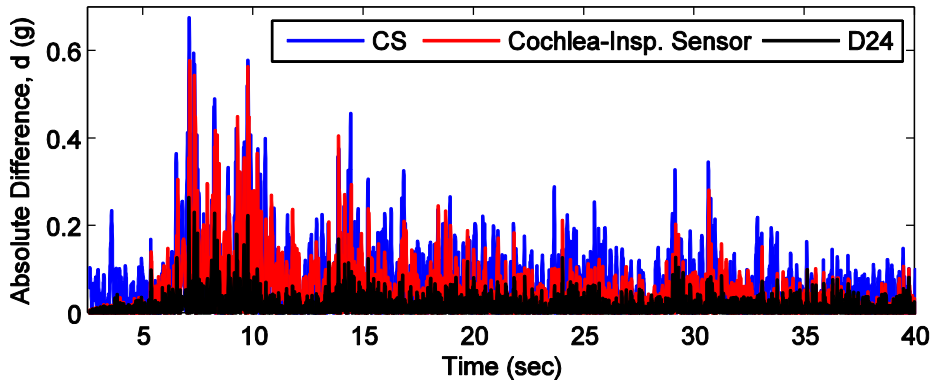

(a)

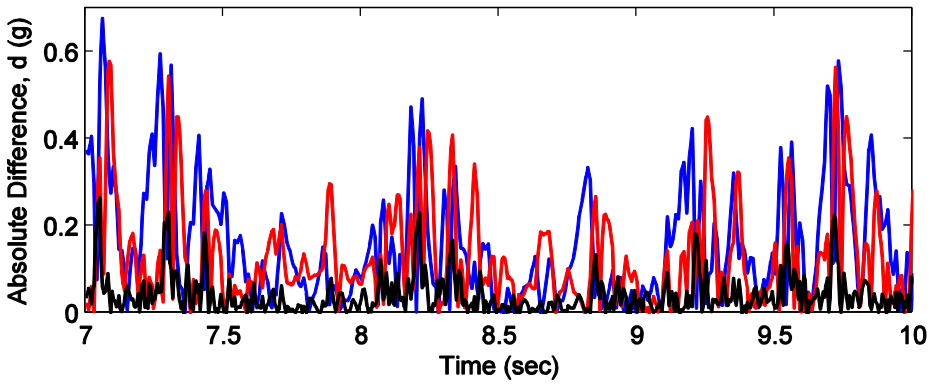

(b)

Figure 3-14. Absolute difference between the input signal, El Centro earthquake, and each reconstructed signal in the full time domain (a) and a sub-section of the time domain (b).

(approximately two times) during the reconstruction process as compared to the wavelet transform. The time history difference, d, and Fourier difference, d_f, between the two signals are shown in Figure 3-14 and Figure 3-15, where $d = u(t)\text{-}r_C(t)$ given that $r_C(t)$ is the reconstructed signal and the subscript C corresponds to the compressive technique (wavelet transform, compressed sensing, or cochlea-inspired sensor system). Additionally, $d_f = U(f)\text{-}R_C(f)$ given that $U(f)$ is the Fourier transform of the input signal, $R_C(f)$ is Fourier transform of the reconstructed signal, and f is frequency (Hz). The seismic ground motion is not completely sparse in the frequency domain and the CS algorithm is unable to approximate the input signal for the desired compression rates, resulting in poor reconstruction capabilities. When considering narrowband signals, such

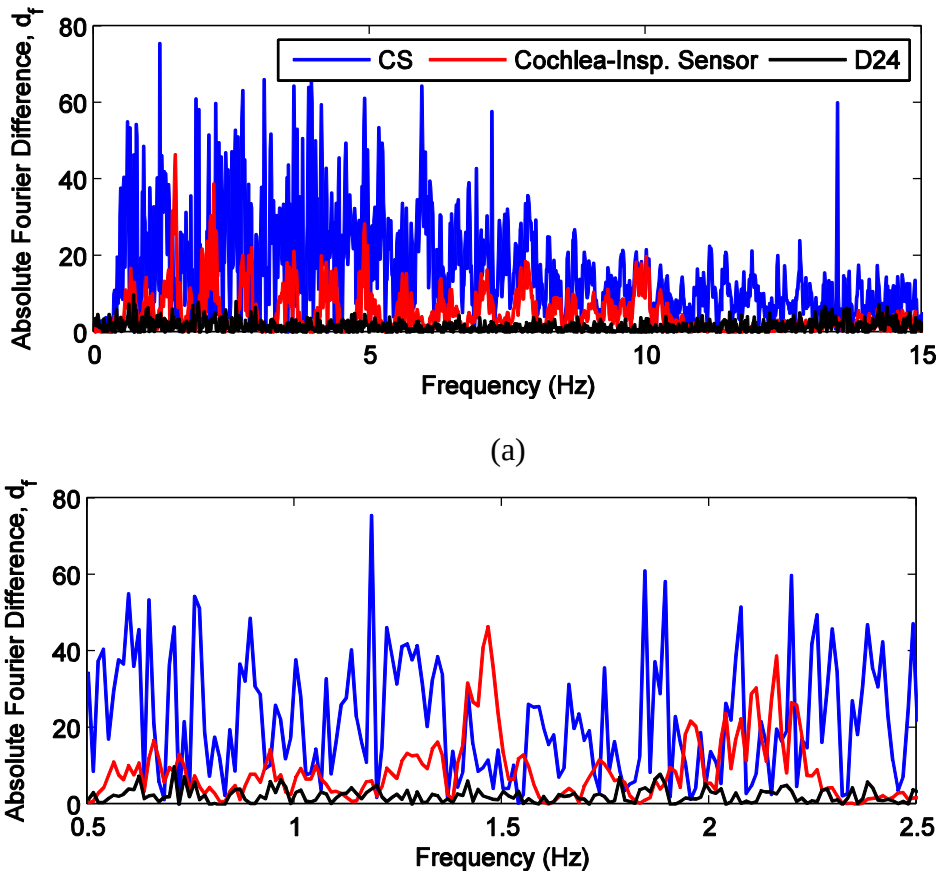

Figure 3-15. Absolute difference between the input signal, El Centro earthquake, and each reconstructed signal in the full frequency domain (a) and a sub-section of the frequency domain (b).

as the structural response, however, the cochlea-inspired sensor outperforms the wavelet transform by achieving extremely high compression ratios (0.988) with acceptable reconstruction error (Figure 3-16, Figure 3-17). Because the structural response signal is sparser in the frequency domain, the CS algorithm is able to better compress the signal, as compared to the seismic signal, while still capturing important characteristics of the signal. However, both alternative compression techniques are unable to achieve the high compression ratios that were established by the cochlea-inspired sensor node and only achieved similar reconstruction errors when decreasing their compression ratios eight to ten times less than the cochlea-inspired sensor system's compression ratio.

The improved reconstruction capabilities of the cochlea-inspired technique for structural response data can be attributed to the filter bank design. The filter bank

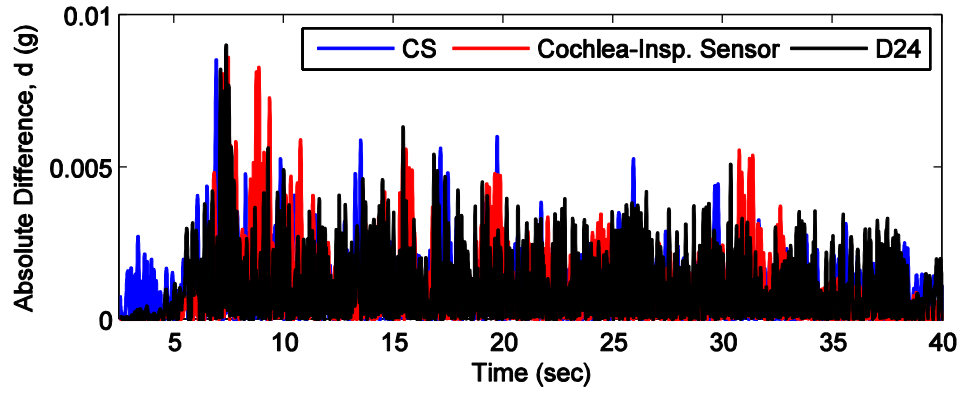

(a)

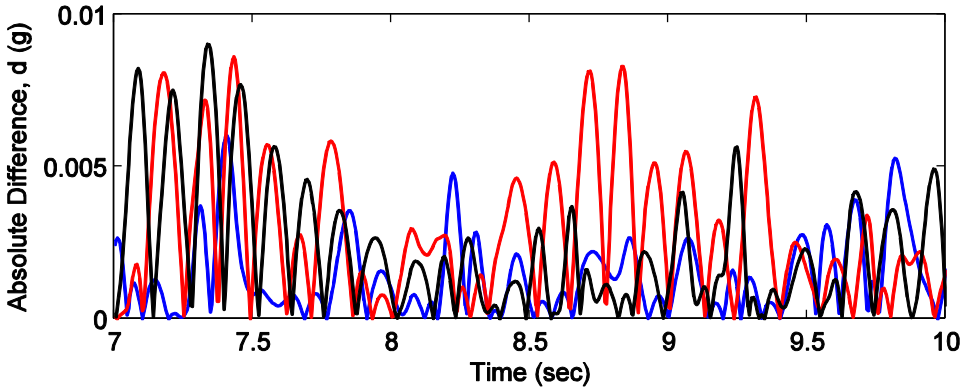

(b)

Figure 3-16. Absolute difference between the input signal, a single degree of freedom structure subject to El Centro earthquake, and each reconstructed signal in the full time domain (a) and a sub-section of the time domain (b).

includes one filter with a characteristic frequency of 3.5Hz and one filter with a characteristic frequency at 4.2Hz, both near the natural frequency of the structure (4.0Hz). Therefore, the majority of the response of the structure is captured by these two filters and surrounding filters contribute little additional information. The filter bank for the cochlea-inspired sensor system was designed such that it could be applied to a variety of input signals, including structures with natural frequencies falling within the range of common earthquake signals. Therefore, it is important to understand the reconstruction capabilities of the sensor system when the natural frequency of the structure does not occur at a characteristic frequency of a specific filter but instead falls between two filters, as shown with the previous example. To consider the impact of the structure's natural

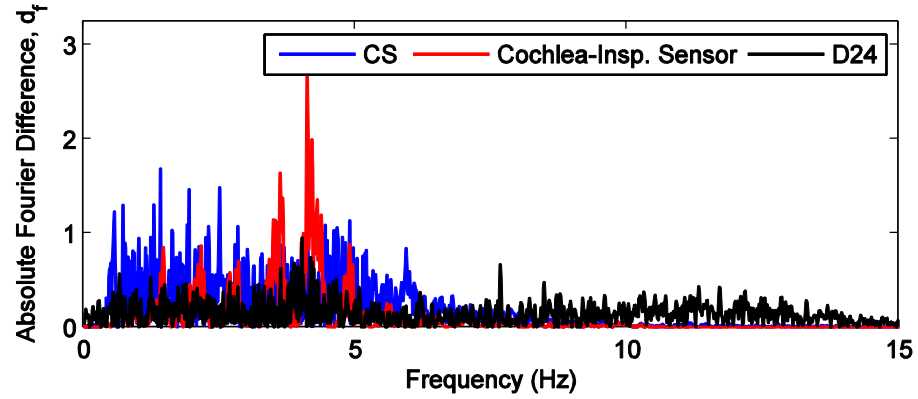

(a)

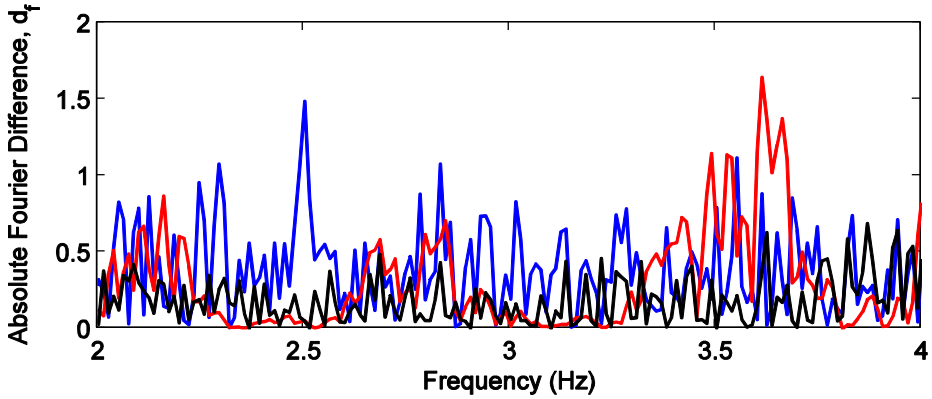

(b)

Figure 3-17. Absolute difference between the input signal, a single degree of freedom structure subject to El Centro earthquake, and each reconstructed signal in the full frequency domain (c) and a sub-section of the frequency domain (d).

frequency, the reconstruction errors, *e* (Equation 3.9), of the response of a single degree-of-freedom structure with varying natural frequencies (ranging from 0.02 to 10.50Hz) subject to the El Centro earthquake are calculated. It is expected that reconstruction errors would be minimized at the characteristic frequencies of the filters and maximized at midpoints between two filters. However, when considering the optimal filter bank (14 filters with a bandwidth of 0.53Hz and spaced at 0.7Hz), this pattern is observed at very low frequency filters (Filters 2 through 4) and is non-existent for higher frequency filters (Figure 3-18a). In Figure 3-18a, the reconstruction errors are shown as they relate to the ratio between the natural frequency of the filter bank's input signal (*i.e.*, structural response) and each filter's characteristic frequency. For example, when considering Filter

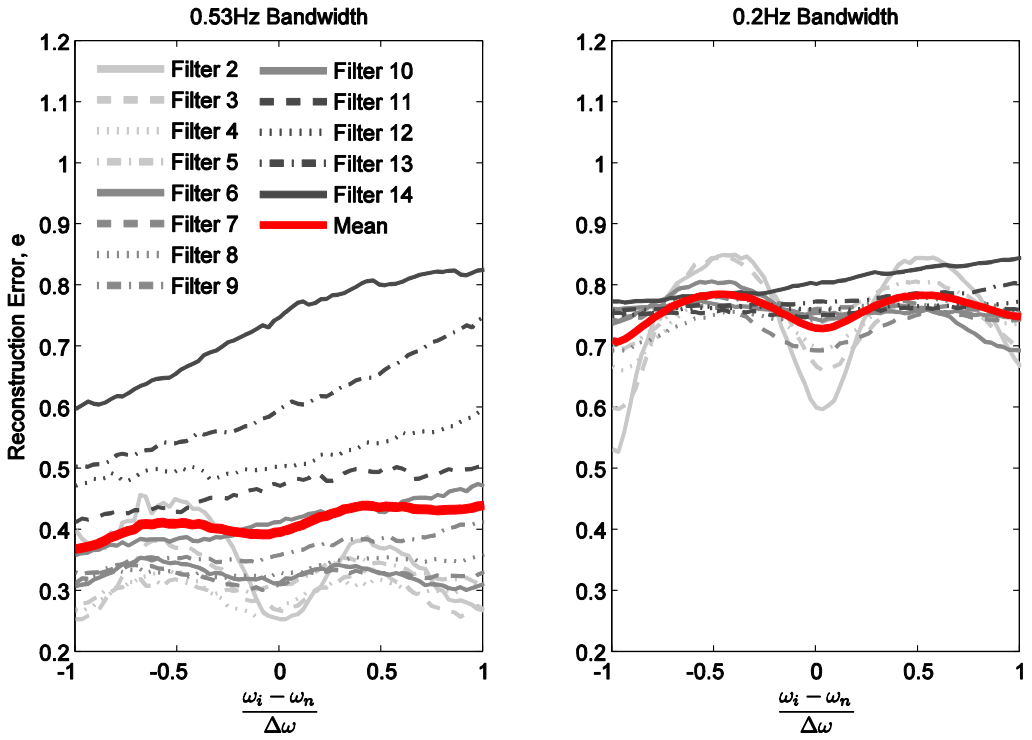

Figure 3-18. The reconstruction capabilities of the filter bank, shown with respect to the filter *i* (characteristic frequency = ω_i) for an optimal filter bank (0.53Hz bandwidth, $\Delta\omega$ = 0.7Hz) (a) and a sub-optimal filter bank (0.20Hz bandwidth, $\Delta\omega$ = 0.7Hz) (b). The input signals include a sweep of various structural responses (natural frequency = ω_n) when subject to El Centro earthquake ground motion, where ω_n varied from 0 to 10.5Hz in 0.02Hz increments.

2 which has a characteristic frequency of 1.4Hz, the reconstruction error is shown for input signals ranging from 0.7 to 2.1Hz in 0.02Hz increments. Typically, little variation in reconstruction error is seen as the structure's natural frequency shifted plus or minus one filter spacing from the filter's characteristic frequency. Thus, because the filter bank is designed for optimal reconstruction, it is able to still accurately represent signals that do not fall directly on top of a filter's characteristic frequency. This point is further exemplified by decreasing the bandwidth of each filter in the filter bank to 0.2Hz, which yields a sub-optimal filter bank with less overlap between filters. In this case, a more defined trend of minimum error at filter locations and maximum error midway between filters is observed. In both cases, it should be noted that Filter 1 (at 0.7Hz) is excluded from the analysis due to its high variability in reconstruction at frequencies less than

$\Delta\omega$ $\Delta\omega$

0.7Hz where these frequencies are only captured by one filter. Some of this variability is seen in the reconstruction response of Filter 2.

Therefore, when considering convoluted signals, such as seismic ground motions, the proposed cochlea-inspired sensor system is not able to reconstruct with the same accuracy as the wavelet transform but it can achieve signal reconstruction with acceptable distortion while maintaining real-time processing capabilities for such signals. Additionally, when considering narrowband signals, such as the structure response, the proposed sensor system's compression capabilities and therefore, reconstruction capabilities far surpass both traditional compression techniques and without significant dependency on the natural frequency of the structure. As such, the proposed sensor can be deemed as a new form of data acquisition that is highly attractive for structural monitoring and control applications.

3.6. Chapter Summary

In this study, the mechanisms employed by the auditory system were explored in the context of signal processing for structural monitoring applications. A cochlea-inspired sensor system was proposed that draws inspiration from the functionality of two methods of the auditory system: the frequency decomposition of the basilar membrane and the encoding process for data transmission. In doing this, the cochlea-inspired sensor was capable of large compression, thus increasing efficiency in data transmission. The functionality of the cochlea-inspired sensor was compared against two compressive techniques, wavelet transforms and compressed sensing, that have been successfully demonstrated on structural monitoring applications. While the wavelet transform performed better than the other two methods, it has significantly larger computational requirements than the cochlea-inspired sensor and is not capable of real-time processing. Therefore, the cochlea-inspired sensor should be considered as a new sensing paradigm that when properly utilized can demonstrate large compressive capabilities through real-time processing.

This chapter proposed the theoretical framework for a new sensing paradigm for structural monitoring. The following chapters will seek to further validate this bio-

inspired mechanism through adaptation to wireless telemetry and implementation in analog circuitry, thus enabling real-time processing with low-cost and low-power components. With the development of this sensor in hardware a specific emphasis will be placed on control applications as this technology enables real-time control through simplistic control laws.

CHAPTER 4

RESOURCE EFFICIENT WIRELESS SENSOR NETWORK ARCHITECTURE BASED ON BIO-MIMICRY OF SIGNAL PROCESSING IN THE CENTRAL NERVOUS SYSTEM

4.1. Introduction

This chapter further draws upon the mechanisms employed by the biological central nervous system (CNS) to fundamentally address the deficiencies currently found in wireless sensor networks (WSNs) in the form of an entirely new wireless sensing paradigm. In this chapter, the novel signal processing and data compression techniques employed by the mammalian auditory system and described in Chapter 3 are utilized as a source of inspiration for a new wireless sensor node. It should be noted that the central nervous system, in general, serves as a source of inspiration as all neurons utilize similar compressive methods of data aggregation and transmission which are attractive for wireless sensing and control. However, the unique pre-processing capabilities of the auditory system offer an interesting perspective for engineering systems. As such, the new wireless sensor node will follow a three step process that is similar to the process demonstrated by the mammalian auditory system. For the biological system, these steps are: 1) spectral decomposition of a convoluted sound signal by the basilar membrane, 2) simultaneous peaking picking and linear encoding by individual neurons associated with sub-sections of the basilar membrane, and 3) compressed data transmission to the auditory cortex along unique nerve fibers. A complete overview of the mammalian auditory system can be found in Chapter 3. This new sensor node will address many of the challenges faced by traditional WSNs in both monitoring and control applications.

This chapter will focus primarily on a monitoring application and Chapter 5 will consider a control application.

By adopting this methodology of signal processing it is forecasted that the current engineering bottlenecks in WNSs (*e.g.*, limited radio bandwidth, high energy consumption, etc.) will be minimized or overcome. In particular, by embracing the analog-domain approaches that are employed by the central nervous system, the new wireless sensor will be capable of complex signal processing in real-time which will ultimately lead to reductions in computational time and energy consumption. Additionally, by employing the data acquisition techniques of the auditory system, the proposed sensing system will adopt asynchronous sampling schemes thus reducing energy consumption from digitizing data. Finally, by decomposing a complex signal into its frequency components and subsequently compressing this information flow into binary spike trains, the amount of transmitted data will be reduced, thereby reducing the energy consumption and wireless bandwidth requirements of a wireless sensor. In this chapter, the theory and hardware design of a new wireless sensor node, based on the mechanisms employed by the CNS, is provided. The sensor is validated on a single degree-of-freedom structure subject to three common earthquake signals and the benefits of the new sensing node, including reduction in power consumption and radio bandwidth, are experimentally demonstrated.

4.2. Sensor Design

With existing wireless sensors limited by fixed communication bandwidth and hampered by a lack of viable long-term power solutions, functional mimicry of the auditory system can potentially resolve these two bottlenecks. As outlined in Chapter 3, data processing in the mammalian auditory system can be described through a three step process: 1) spectral decomposition by the basilar membrane, 2) linear encoding and data compression by the inner hair cells, and 3) data transmission by the nerve fibers. The proposed wireless sensor performs similar processing as the cochlea by: 1) decomposing a convoluted signal into frequency components through the use of a band-pass filter bank, 2) data compression of each filtered signal by individual microcontrollers, and 3) wireless

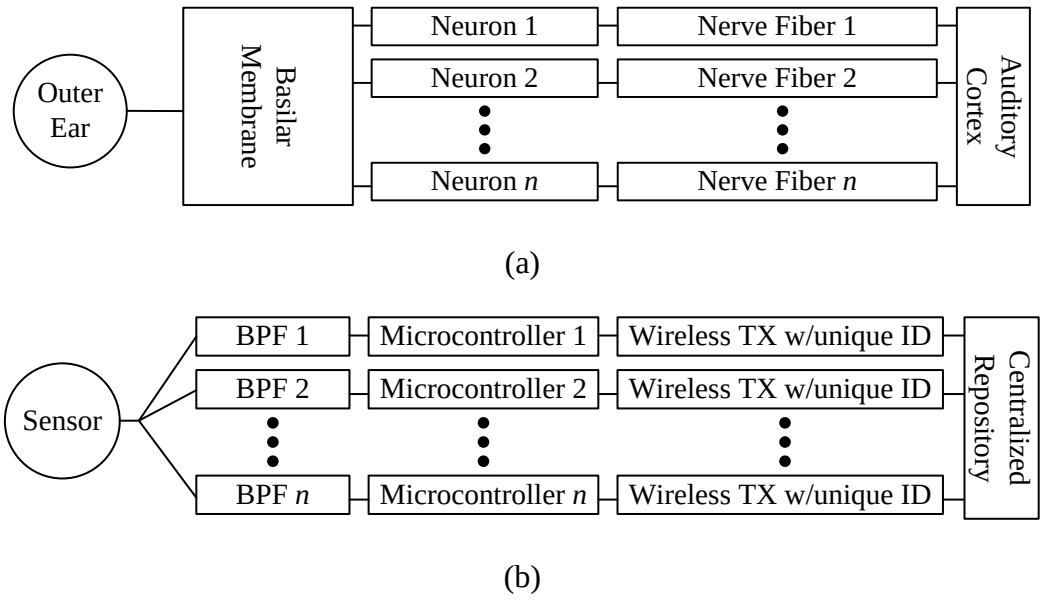

Figure 4-1. Simplified schematic of the mammalian auditory process (a) compared with the process of the proposed wireless sensor system which utilizes a band-pass filter (BPF) bank and microcontrollers to emulate the function of the cochlea's basilar membrane and neurons, respectively (b).

transmission to a centralized repository (Figure 4-1). This wireless sensing architecture inspired by these operational principles of the mammalian auditory system will be ultra-low power, capable of performing time-frequency analysis in real-time through analog-domain signal processing, and capable of communicating sensor measurements in a compressive manner for network scalability. Similar to the functionality of neurons, the proposed wireless sensor will exhibit a high degree of modularity in its hardware design, thus allowing it to be adapted according to the constraints of any given monitoring application. As such, each cochlea-inspired wireless sensor node is to be comprised of multiple "neurons" in the form of neuron boards that each represent one narrow-band channel in an analog filter bank, much like the hair-cell neurons at a specific location along the length of the basilar membrane. Stacks of modular neuron boards can be assembled to form the complete analog filter bank similar to the basilar membrane. All neuron boards within a stack share system resources (*e.g.*, power, digital clock signal, and access to a wireless transceiver) through a bussing system (Figure 4-2). Additional considerations for the sensor design will include overall power consumption and device cost, both of which will be quantified herein.

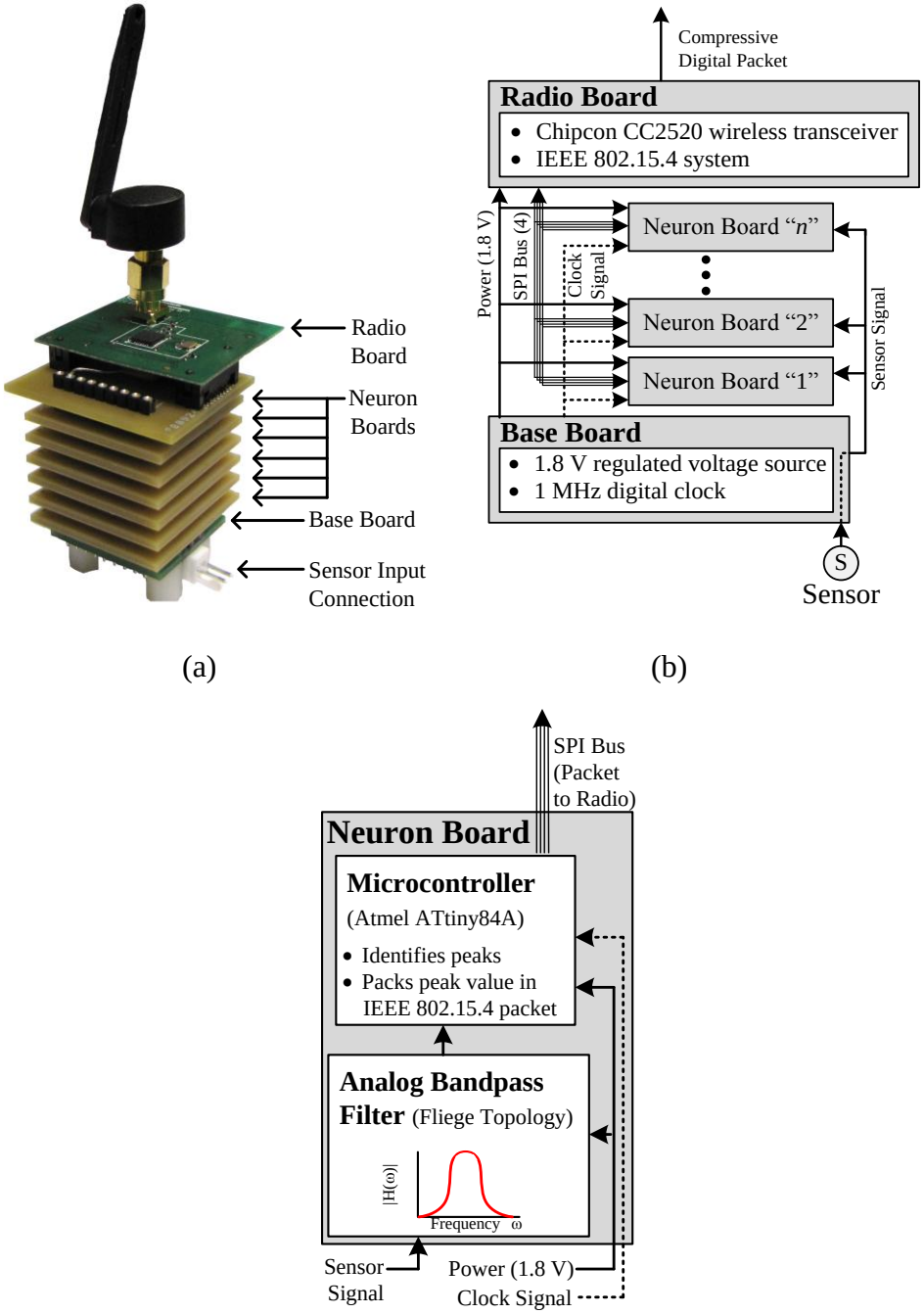

Figure 4-2. Cochlea-inspired wireless sensor node with a radio board, multiple neuron boards, and base board (a), schematic of complete sensing node with "*n*" neuron boards (b) and functional schematic of a typical neuron board (c).

.

Table 4-1. Signals transmitted through bus connections.

Symbol	Signal	Symbol	Signal
B1	Analog Signal (direct from sensor)	*B10*	Supply Voltage (1.8V)
B2	Ground Signal	*B11*	Half Supply Voltage (0.9V)
B3	SPI Clock	*B12*	Reset
B4	Microcontroller Programming Pin	*B13*	SPI Chip Select
B5	SPI Output	*B14*	Digital Clock (1 MHz)
B6	Microcontroller Programming Pin	*B15*	Contention Pin
B7	SPI Input	*B16*	Radio GPIO
B8	Microcontroller Programming Pin	*B17*	Radio GPIO
B9	Enable Radio		

4.2.1. Base Board

To decrease the overall power consumption of the modular sensing node, each neuron board is designed to be ultra low-power. To achieve this goal, certain node resources and signals are shared amongst all of the neuron boards through a bussing system (Table 4-1), thus reducing the number of hardware components on each neuron board and the overall power consumption of the system. These signals are generated on a base board (Figure 4-3a) and bussed through shared connection lines (pins *B1* through *B17*) to all of the neuron boards (Table 4-1). The base board connects to an external sensor and routes the analog sensor signal, a 1MHz digital clock signal (using Linear Technologies LTC6930CMS8-8.00#PBF scaled to 1MHz output) and a stable 1.8V power supply delivered from a Torex Semiconductor Limited voltage regulator (XC6221B182MR-G) to the stack of neuron boards. The bussing system also contains lines for radio communication which will be discussed in further detail with the radio board. This base board is designed as a four-layer printed circuit board (PCB) with a footprint that is roughly 2.5cm x 2.5cm. The fully assembled base board consumes approximately 700μW of power (0.39mA at 1.8V) and costs approximately $20. By limiting these resources to a single board, rather than requiring all sensor boards to maintain independent clocking and power, the overall power consumption and cost of the sensing node is significantly reduced.

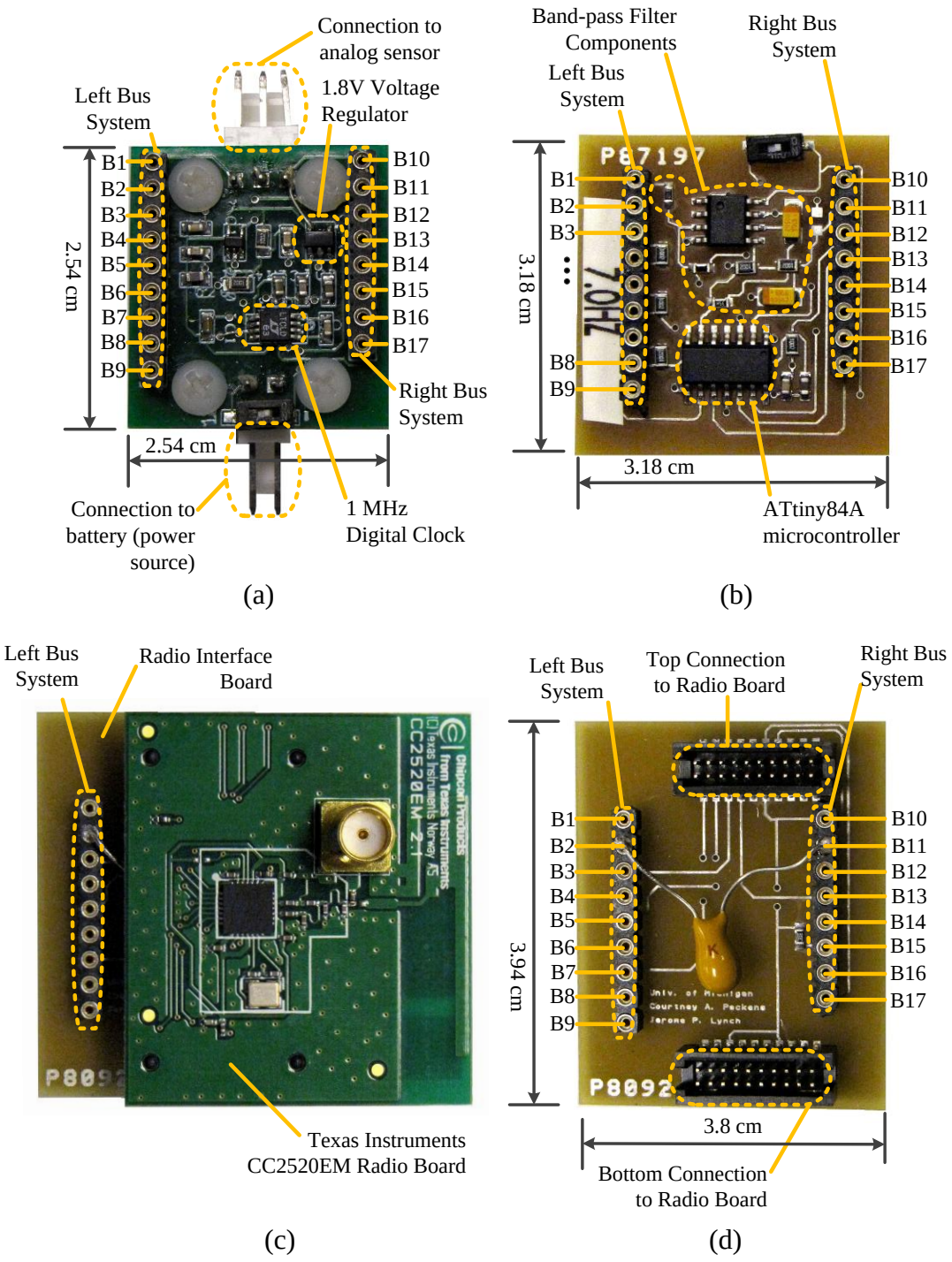

Figure 4-3. Circuit prototype of baseboard (a), neuron board (b), Texas Instruments' CC2520 radio board on radio interface board (c), and radio interface board (d).

4.2.2. Neuron Board

To achieve the advantages of the mammalian auditory system, each neuron board (Figure 4-2b, c) follows a similar three step process to that found in the biological system: 1) real-time frequency decomposition by the basilar membrane, 2) peak value encoding by the inner hair cells, and 3) efficient data transmission through nerve fibers. In the proposed neuron board, these three steps are encapsulated through signal decomposition using a bank of analog band-pass filters, peak picking using a low-power computing core, and information transmission to a wireless transceiver. In the proposed sensor, the real-time spectral decomposition of the basilar membrane is replicated through a band-pass filter bank where each channel in the bank represents a sub-section of the basilar membrane, thus enabling parallel processing in real-time. To allow versatility, the filter bank is designed in a modular manner such that users can easily reconfigure the analog filter bank characteristics (such as filter spacing, filter bandwidth, *etc*.) simply by assembling different neuron boards together.

When choosing the parameters for the filter bank (*e.g*., filter spacing, filter bandwidth, number of filters) it is important to maximize the reconstruction capabilities of the filter bank by minimizing the signal distortion incurred through the filtering process. In other words, it is desired that when reconstructing a signal that has been decomposed by the filter bank that $u(t) \approx y(t)$, where $u(t)$ is the input signal and $y(t)$ is the reconstructed signal determined by

$$y(t) = \sum_{i=1}^{N} y_i(t) \tag{4.1}$$

such that $y_i(t)$ is the output of the i^{th} band-pass filter and N is the number of filters in the filter bank. The characteristics of each i^{th} filter are controlled by two parameters: a central frequency, f_i (Hz), and the Q-factor (where $Q = (2\xi_i)^{-1}$ and ξ_i is the damping ratio of the filter). To simplify the design in this study, all filters are assumed to be equally spaced ($\Delta f = f_i - f_{i-1}$) and to have a constant bandwidth. The output of each filter is found through convolution of the original input signal with the filter's impulse response function, $h_i(t)$, as follows:

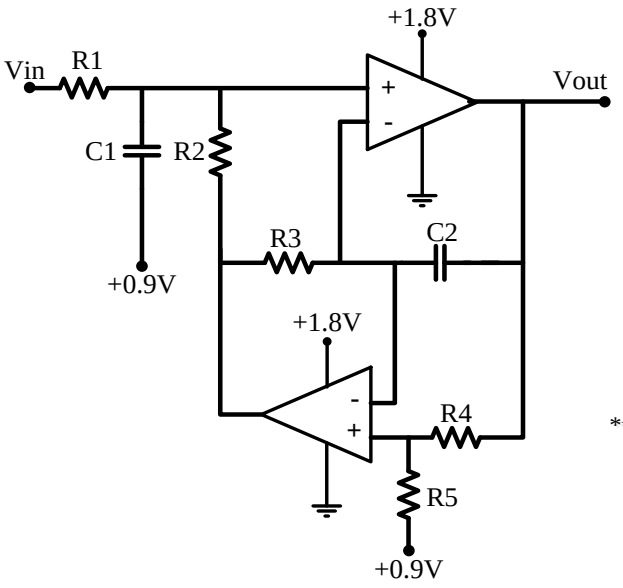

Component	Symbol	Value
General Capacitor*	*C*	10μF
Capacitor 1	*C1*	*C*
Capacitor 2	*C2*	*C*
General Resistor*	*R*	$(2\pi\omega_i C)^{-1}$
Resistor 1	*R1*	$R(2\xi_i)^{-1}$
Resistor 2	*R2*	*R*
Resistor 3	*R3*	*R*
Resistor 4	*R4*	10kΩ
Resistor 5	*R5*	10kΩ

*used for component design purposes only

Figure 4-4. Fliege band-pass filter topology.

$$y_i(t) = \int_0^t u(t)h_i(t-\tau)d\tau \tag{4.2}$$

where

$$h_i(t) = -2\xi_i\omega_i\left(\sqrt{1-\xi_i^2}\right)^{-1} e^{-\xi_i\omega_i t}\sin\left[\left(\omega_i\sqrt{1-\xi_i^2}\right)t - \tan^{-1}\left(\xi_i^{-1}\sqrt{1-\xi_i^2}\right)\right] \tag{4.3}$$

and $\omega_i = f_i/2\pi$. By varying the three parameters N, Δf, and ξ_i, the reconstruction capabilities of the filter bank can be optimized according to the constraints dictated by the desired application for the sensor.

Each neuron board contains one unique filter from the filter bank, thus allowing the wireless sensor node to be easily modified by inserting or removing new boards or modifying the characteristics of the filters. The Fliege filter topology (Figure 4-4) is chosen for the analog band-pass filter due to its stability at high Q values and its constant gain value of 2 (Carter 2000). With this topology, a constant capacitor value, C, is chosen by the designer which then dictates the resistor and capacitor values that are used in hardware. To maintain capacitors in the micro-Farad range and resistors in the kilo-Ohm range, C is chosen as 10μF and Resistors 1, 2, and 3 are designed based on this constraint to achieve the desired characteristic frequencies and bandwidths of the filters.

Resistors 4 and 5 are non-critical components whose only design constraint is that they are equal in value and therefore, they are chosen to be 10kΩ to maintain the same magnitude as the other three resistors. With the Fliege topology, the bandwidth and characteristic frequency of a filter can easily be changed by modifying resistors *R1*, *R2*, and *R3*.

The filter output is fed to a low-power microprocessor whose function is similar to the inner hair cells on the cochlea in that it encodes the filtered signal into a compressed "neural" signal. The computing core for the neuron board is chosen as Atmel's ATtiny84a due to its low power consumption (210μA in active mode at 1.8V and 1MHz clock speed). The filtered signal is sampled at 200Hz by the microprocessor's internal 10-bit analog-to-digital converter (ADC). With each sample, the microprocessor runs a real-time peak picking algorithm. In this algorithm, the microprocessor continually stores the current sampled value as well as the two previously sampled values. With these three data points, the microprocessor calculates the slope between concurrent sampled values and uses these to predict the slope of the next sampled value. If the predicted slope value has a different sign than the previous slope then a peak value is detected. Otherwise, the microprocessor continues sampling while refreshing its buffer of the past two samples. Due to the low resolution of the ADC, peak values on gradually sloping signals may go undetected using this algorithm. As such, a secondary peak picking algorithm is implemented that checks if the second sampled value is greater than (or less than) both the first and third sampled values. If this occurs then the second sample is detected as a peak value. This secondary check only occurs if a peak was not found during the previous iteration of sampling. This entire peak picking algorithm occurs in less than 5msec, thus ensuring that the sampling time is greater than the computational time of the algorithm and therefore, there is no opportunity to miss peak values.

Once a peak is detected, the microprocessor further compresses the data by linearly encoding the detected peak value into a one-byte value. However, rather than further degrade the resolution of the sampled value, the full 1,024 bit output range of the 10-bit ADC is instead supervised by four "neurons", each monitoring a unique set of 256 bits (*e.g.*, neuron zero is activated if a peak falls within the 0 to 255 bits of the ADC,

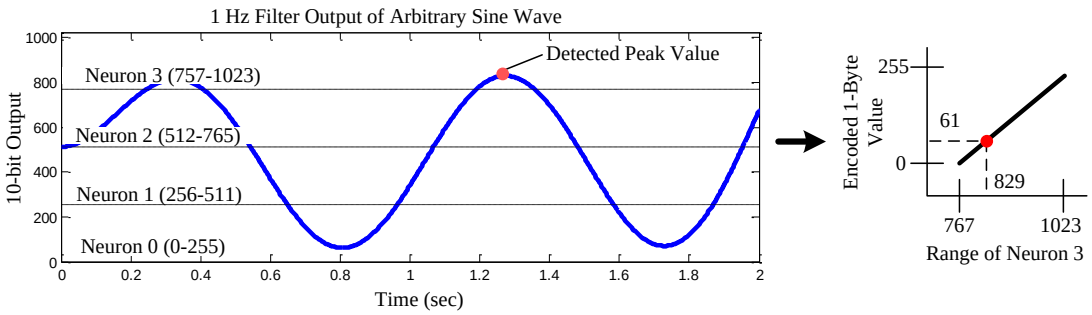

Figure 4-5. Example of encoding process for 1 Hz filter output.

neuron one within 256 to 511, etc.). Therefore, once the microprocessor has detected a peak value, P, that is in the ADC's integer form, it calculates which neuron, N_e, to activate:

$$N_e = \left\lfloor \frac{P}{256} \right\rfloor \tag{4.4}$$

where $\lfloor \cdot \rfloor$ is the floor function that rounds the quotient down to the nearest integer. Based on the activated neuron, the peak value is encoded into a one-byte value, P_e, where $P_e = P\text{-}256 \cdot N_e$. In addition to this one byte of data, the neuron board also transmits a "neural code" such that the previously encoded peak value can be properly decoded at the centralized location. The "neural code", NC, encapsulates information about the activated neuron as well as the neuron board's unique identification number, ID, that is used when decoding the received data at a centralized location, $NC = 4 \cdot ID + N_e$. As an example of this process, consider the output of a 1Hz filter (with an identification number, ID, of 1) when filtering an arbitrary sine wave (Figure 4-5). Neuron 3 on this board detects a peak value of 829 at 1.27 seconds. The microcontroller linearly encodes this value into a one-byte value of 61 and computes the "neural code" as 7 ($NC = 4 \cdot 1+3$). These two bytes of data are packaged by the microcontroller for transmission through the wireless transceiver.

The wireless transceiver uses IEEE 802.15.4 communication standards and as such, these two bytes of data are transmitted using the IEEE 802.15.4 Frame Format (Texas Instruments 2007). This format includes a 9-byte media access control (MAC) header that includes the Frame Control Field, the Data Sequence Number, and the

	MAC Header					MAC Payload
	Frame Control Field (2 Bytes)	Data Sequence Number (1)	Address Information			Frame Payload (1)
			Destination PAN ID (2)	Destination Address (2)	Source Address (2)	
Example:	0x4188	0x01	0xFFFF	0xFFFF	0x0007	0x61

Figure 4-6. Packet structure used in wireless data transmission.

Address Information (Figure 4-6). All fields within this header are initialized upon power-up of the sensing node, except for the source address. The two bytes designated for the source address are filled with the neural code, *NC*, as established by the neuron board that is sending the data. Each packet also includes one byte of data (*i.e.*, the encoded peak value) that is transmitted as the payload when the wireless transceiver communicates this packet over the wireless sensor network. Once the microcontroller has assembled the packet it communicates its information to the wireless transceiver using a shared Serial Peripheral Interface (SPI) bus (*B3*, *B5*, *B7*, and *B13* from Table 4-1). This process will be further discussed when considering the design of the radio board.

Each neuron board is designed on a two-layer PCB that is roughly 3.18cm x 3.18cm (Figure 4-3b). The two vertical header pins shown on both the left side (*B1* through *B9*) and right side (*B10* through *B17*) of the neuron board correspond to the same pins shown in Figure 4-3a. Because each neuron board does not have to support an internal clock or other peripherals, it consumes approximately 1.1mW of power (0.6mA at 1.8V and 1MHz) when active and costs approximately $10 (per board). As each neuron board represents a small sub-set of the entire filter bank, multiple units can be stacked together through the bussing lines to capture the full frequency spectrum of the input signal. While adding more neuron boards in the assembly of a wireless sensor node linearly increases cost and power for the entire sensing node, the complete sensing node still remains extremely low power and low cost. This enables feasible scale up to large filter banks consisting of 10's of neuron boards.

4.2.3. Radio Board

The neuron boards interface with a single Texas Instruments CC2520 radio (Figure 4-3c) that operates using the IEEE 802.15.4 communication standard (Texas Instruments 2007). A radio interface board (Figure 4-3d) provides a connection transition to the CC2520EM radio board obtained from Texas Instruments (2009). Information is sent independently from each neuron board using a shared Serial Peripheral Interface (SPI) bus (*B3*, *B5*, *B7*, and *B13* from Table 4-1). However, because each neuron board is sharing (and therefore competing for) the radio, an additional communication line (*B15*) is included to prohibit communication contention between boards. If a board intends to send information to the radio it must first check the contention line. If the contention line is free (*i.e.*, high) then no other boards are accessing the radio and the microcontroller on that board can transmit its information by first pulling the contention line low and then connecting with the radio. Once the board has completed the transmission it releases the contention line (pulling it high), thus allowing other boards to access the radio. This entire process completes in approximately 1.67msec if no contention is encountered. However, if a board checks the contention pin and it is low indicating that the radio is in-use, then the board backs off for a random time period before re-checking the line. If the contention line does not become free within a specified amount of time (2.5msec which is half of the sampling period) then the unit abandons its transmission and continues with its peak-peaking. While that peak is lost, this strategy is necessary to limit the amount of delay in the overall system and to prevent system grid-locks. The random back-off is created by generating a random integer through the microcontroller's built-in random number generator. This integer is used to create a single random delay that ranges from 20 to 90μsec. After this delay the microcontroller rechecks the contention pin. Because all of the neuron boards operate on the same digital clock and power source, each of the filter boards is initialized to the same default seed for the random number function generator. Therefore, in order to reduce the likelihood of two boards simultaneously detecting peak values and re-attempting to access the contention pin at the same time, upon initialization the random number generator on each unique board is seeded based on the neuron board's unique identification number.

Table 4-2. Power consumption and cost of each board. *X* is an arbitrary number of Neuron Boards that linearly scales the total cost and power consumption.

Board	Power Consumption (mW)	Cost
Base Board	0.7	$20
Neuron Board	1.1	$10
Radio Board	46.4	$50
Base + *X* Neuron + Radio	47.1 + 1.1*X*	$70 + $10*X*

The radio interface board is a 2-layer PCB that is roughly 3.94cm x 3.18cm (Figure 4-3d). The two vertical header pins shown on both the left side (*B1* through *B9*) and right side (*B10* through *B17*) of the interface board correspond to the same pins shown in Figure 4-3a and b. The two 20-pin horizontal headers interface with the Texas Instrument's CC2520EM radio board and map to specific pins on the vertical headers (Table 4-1) to enable direct access to the wireless transceiver. In its transmitting state the radio board consumes 46.4mW of power (26mA of power at 1.8V) but less than 2μW of power (1.1μW of power at 1.8V) in power down mode per the manufacturer's specifications. To reduce power consumption, the transceiver is kept powered down and only made active when a neuron board transmits data.

4.2.4. Summary of Hardware Design

The new wireless sensor node is designed such that it can easily be adapted to new applications by modifying both the number of neuron boards as well as the characteristics of filters on board the neuron boards. A complete sensing node is created by combining a single base board with a variable number of neuron boards and a wireless transceiver (Figure 4-2a). With this modularity comes a variable height for the sensing node that is linearly related to the number of neuron boards. The base board and each neuron board have a height of 0.044cm. Additionally, the power consumption of the sensing node increases on a linear scale (Table 4-2). For example, 10 boards consume 58.1mW of power at 1.8V and cost $170 while 20 boards consume 67.1mW of power at 1.8V and cost $270. It should be noted that this is an academic prototype and in

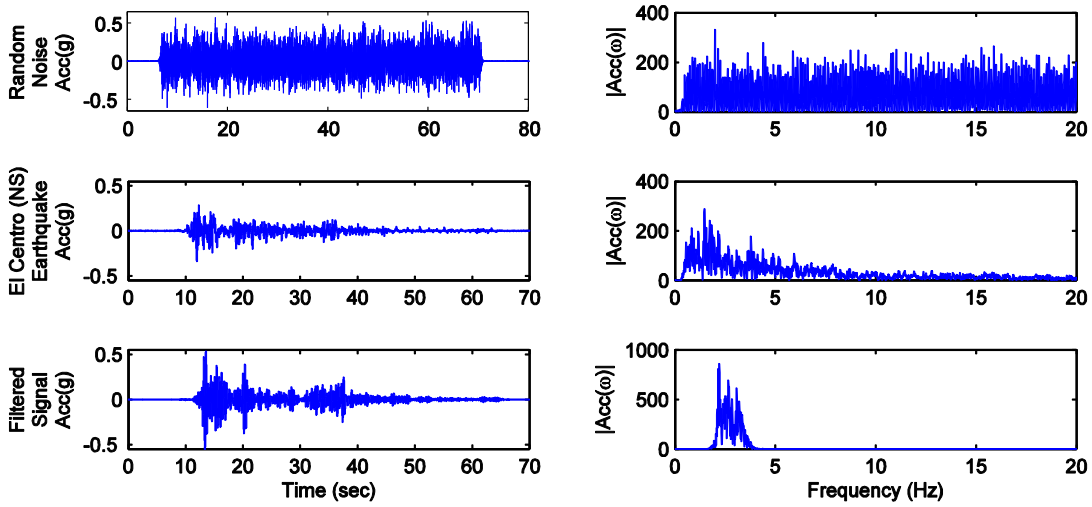

(a) (b)

Figure 4-7. Three input signals used to determine characteristics of stochastic communication in time (a) and frequency (b) domains.

commercial applications the sensing node could be made significantly more cost-effective and smaller.

4.3. Laboratory Study on Effects of Stochastic Communication

Due to the random back-off and possibility of contention between neural boards, the communication from each wireless sensor node is a stochastic process that has strong relation to the input signal. This variability is assessed in a controlled environment for three different input signals that are related to the intended application of monitoring civil infrastructure: 1) a broadband-white signal (0.4g root mean square (RMS) random noise), a wideband-seismic signal (1940 0.4g El Centro earthquake NS), and a narrowband-seismic signal (band-pass filtered El Centro earthquake at 2.75Hz with bandwidth of approximately 1Hz) (Figure 4-7). These signals are created on a function generator and fed into the sensor to ensure repeatability of the input signal. The filters on the neuron boards are arbitrarily chosen to be spaced every 0.5Hz with 0.35Hz bandwidth. The characteristic frequency of the first filter board starts at 0.5Hz and each new board's frequency is 0.5Hz greater than the previous, thus widening the total bandwidth of the

filter bank with each new board. Each signal is input to the cochlea-inspired wireless sensor node 100 times for a varying number of filter boards (from 5 to 25 neuron boards). Specifically, the broadband-white and wideband-seismic signals are tested using 5, 10, 15, 20, and 25 boards while the narrowband-seismic signal is tested using 5, 10, 15, and 20 boards. The narrowband-seismic signal is not tested with 25 boards because higher frequency boards have little response when using 20 filters and therefore it is deemed unnecessary to add additional boards. During these tests, packets are sent from the wireless sensor node to a nearby (<5m) centralized repository and the number of skipped packets due to radio contention is monitored for each test. Due to the controlled environment it is assumed that the wireless channel is 100% reliable in this set of tests and therefore packets are lost only due to radio contention. The input signal is reconstructed at the centralized repository using the received peak values from the wireless node. To assess the reconstruction capabilities of the wireless sensor node, a reconstruction error based on the root mean square error, E_{RMS}, is used:

$$E_{RMS} = \sqrt{\left[\sum_{k=1}^{K}\left(u(k\Delta t)\text{-}y(k\Delta t)\right)^2\right]\cdot K^{-1}}\cdot(\max|u(k\Delta t)|)^{-1} \tag{4.5}$$

where K is the length of $u(t)$ when sampled at an interval Δt. Similarly, the reconstruction error in the frequency domain is defined as, F_{RMS},

$$F_{RMS} = \sqrt{\left[\sum_{k=1}^{K/2}\left(U(f_k)\text{-}Y(f_k)\right)^2\right]\cdot\left(\frac{K}{2}\right)^{-1}}\cdot\left(\max\left|U(f_k)\right|\right)^{-1} \tag{4.6}$$

where U(f) and Y(f) are the discrete Fourier transforms of $u(t)$ and $y(t)$, respectively.

The probability density functions for the percentage of skipped packets for all three signals are approximately described by Gaussian distributions (Figure 4-8). For the wideband-seismic and broadband-white signals, when a small number of neuron boards are used (*i.e.*, 5 filters), the filter bank does not capture the frequency spectrum of the signal well and a minimal number of packets are sent, resulting in little-to-no radio

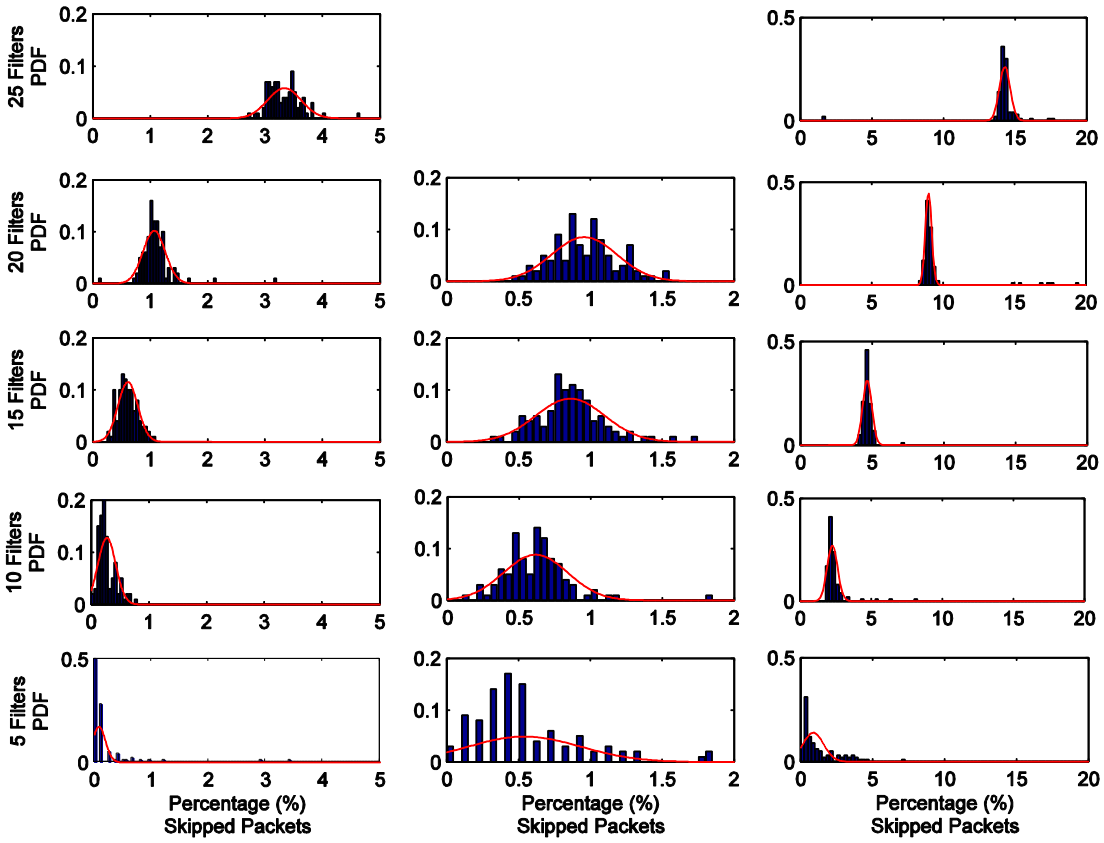

(a) (b) (c)

Figure 4-8. Probability density function (PDF) of percentage of skipped packets for wideband-seismic (a), narrowband-seismic (b), and broadband-white (c) signals.

contention. Both the wideband and broadband signals' average percentage of skipped packets increases exponentially as the number of boards are increased linearly (Figure 4-9a). The average percentage of skipped packets for the narrowband-seismic signal, on the other hand, remains linear with a minimal slope as the number of boards increases. Because the energy of the signal is primarily contained in the spectrum below 5Hz, adding boards whose frequency extends beyond this range has little effect and few additional packets are sent. When considering the wideband-seismic signal, however, while its energy content is concentrated below 7Hz, higher frequencies are still present in the signal. Therefore, the addition of higher frequency boards results in attempted communication from these boards, thus resulting in a higher percentage of skipped packets from increased contention. Similarly, because the broadband-white signal has

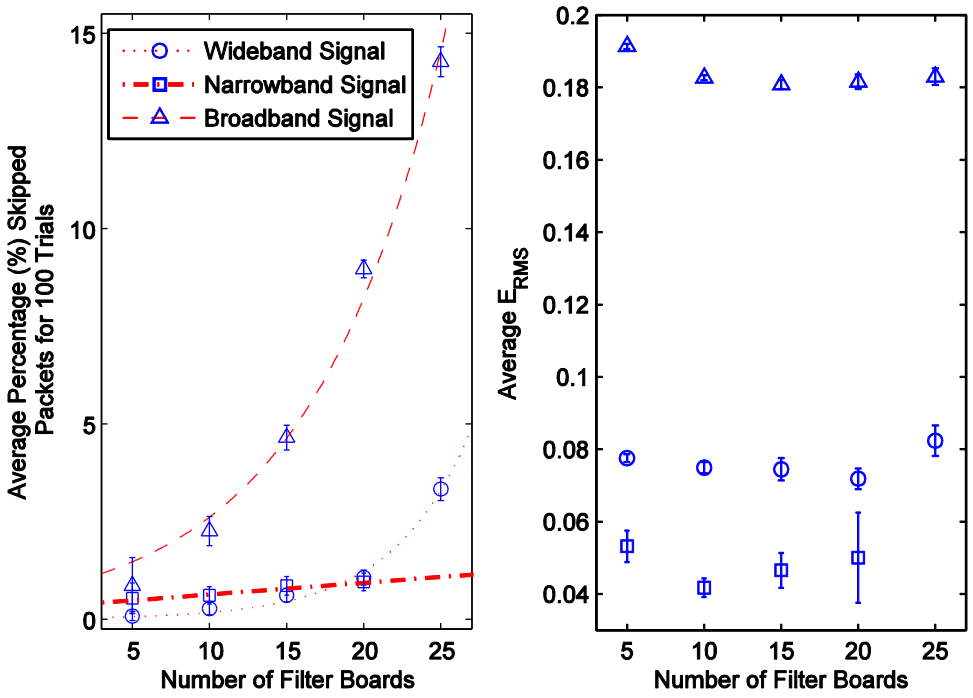

(a) (b)

Figure 4-9. Average percentage of skipped points (a) and reconstruction error (b) as the number of filter boards increases in the wireless sensor node for a wideband-seismic signal (El Centro earthquake), a narrowband-seismic signal (filtered El Centro earthquake), and a broadband-white signal (random noise).

higher amplitude frequencies across a wider frequency spectrum, it experiences this same radio contention but at higher percentages and with fewer boards. Therefore, it can be concluded that as the bandwidth of the input signal increases, the contention in the node also increases but with fewer neuron boards.

When considering the reconstruction error, adding more filter boards has varying effects (Figure 4-9b). For the wideband-seismic signal, increasing the number of boards decreases the reconstruction error until 25 boards are reached. At 20 boards, the filter bank can represent the frequency spectrum of the signal and there is a minimal number of skipped packets (< 1%). However, adding 5 more boards increases the radio contention and potentially transmits peaks from low-priority high frequency filter boards that have low amplitude signals instead of high-priority low frequency filter boards with high amplitude signals, thus increasing the reconstruction error. For the narrowband-seismic

signal, on the other hand, while adding more boards enables more frequencies to be represented, it is unnecessary because the energy content of the signal can be adequately captured by the 10 boards and extending the number of boards beyond 10 filters actually increases the reconstruction error. Higher frequencies are not extremely dominant in the narrowband signal and occasionally a higher frequency board will seek to transmit data which could prevent a lower frequency board from sending more significant data.

Therefore, as demonstrated by this study on radio contention, as the number of filter boards increases in the cochlea-inspired wireless sensor node, the percentage of skipped packets also increases. This percentage of skipped packets does have dependency on the signal with very wideband signals resulting in large contention and a loss of packets. In general, the loss of packets does not significantly impact the reconstruction capabilities of the system with the reconstruction error not showing large dependency on the number of skipped packets for any of the signals. The number of filter boards, however, does have an impact on the reconstruction capabilities of the system and the optimal number of filters is signal dependent based on the energy content of the signal. As such, each wireless sensor node should be designed according to its application so as to minimize the potential for radio contention while also minimizing the reconstruction error. This study also highlights an important limitation of the cochlea-inspired wireless sensor node in that it is unable to adequately capture broadband signals, such as random noise. For such signals, all neuron boards attempt to continuously communicate detected peak values, resulting in large contention across the radio, a large number of skipped packets, and an inability to adequately reconstruct the input signal. By decreasing the number of boards, less radio contention occurs but the node is unable to capture the wide frequency content. Therefore, from this study it can also be concluded that the cochlea-inspired sensor node is not well-suited for extremely broadband signals. This finding is expected due to the finite radio bandwidth of the sensing node and wide frequency spectrum of the input signal.

4.4. Experimental Validation with Seismic Monitoring Application

The proposed cochlea-inspired wireless sensor is validated on a seismic monitoring application of a short-span bridge test-bed. Civil infrastructure, and in particular bridges, are unavoidably exposed to time-critical events, such as earthquakes or typhoons. This is particularly challenging in that the functionality of these structures is often imperative during such events and therefore it is important to have methods of assessing the bridge performance during and after the event. In recent years, numerous bridges worldwide have been instrumented with monitoring systems, both wired and wireless, thus enabling periodic assessment of the structure subject to various loadings (*i.e.*, ambient vibrations, seismic events, extreme wind loads) (Ko and Ni 2005). Wired systems do not face the same power constraints as wireless systems and therefore are able to collect data more regularly and also use trigger systems to increase data collection during these time-critical events (Fujino *et al.* 2000; Wong *et al.* 2000). Wireless systems, on the other hand, have higher power constraints and therefore rely on extreme power management, such as extensive sleep modes (Park *et al.* 2010) or schedule-based data collection (Kurata *et al.* 2013), to maintain continual operation. Such techniques, however, come at the risk of missing events and therefore, ultra-low power wireless sensor nodes which require minimal sleep time are needed. The proposed cochlea-inspired wireless sensor is validated with this application in mind by monitoring the response of a short-span bridge subject to seismic ground motion.

The test-bed for validating the proposed sensor is a small-scale single span bridge (Figure 4-10) that sits on a 5m x 5m shake table at the Korea Construction Engineering Development (KOCED) Multi-Platform Seismic Simulation Center at Pusan University, Pusan, Korea. The deck of the bridge is a reinforced concrete slab (1.8m x 2.3m x 0.1m) and is affixed to two wide flange girders (depth of 0.294m and width of 0.2m) evenly spaced 0.45m from the center line of the concrete. These two girders sit on four wide flange posts (0.3m deep and 0.4m wide) that are reinforced with steel plates perpendicular to the web to prevent weak axis bending of the posts. The entire mass of the bridge specimen is 1,282kg. The bridge sits on four rubber bearings (horizontal stiffness of 167kN/m, vertical stiffness of 3,292kN/m) which simulate the behavior of

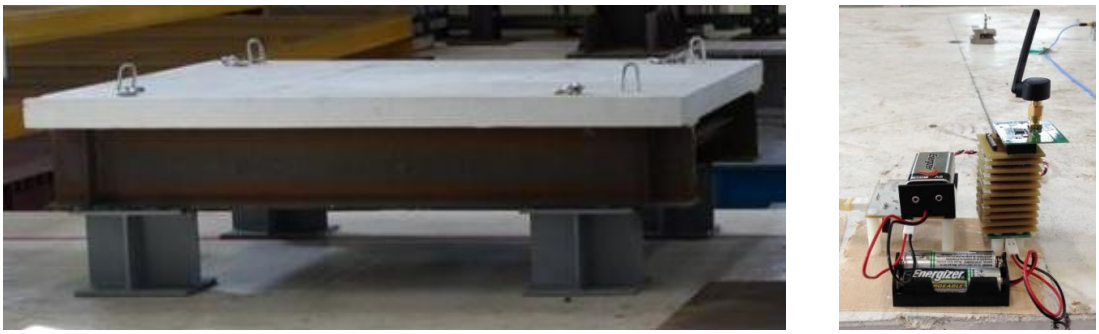

Figure 4-10. Single span bridge used for validation of wireless sensor (a), cochlea-inspired wireless sensor node on test-bed (b), side view schematic of bridge with instrumentation (c), front view schematic of bridge (d), and frequency response function of single-span bridge when subject to random excitation (e).

columns for the bridge. The first modal frequency of the structure is identified through a random noise analysis as 3.6Hz (Figure 4-10e). The structure and the shake table are instrumented with the cochlea-inspired wireless sensor, as well as a traditional wired laboratory data acquisition system to validate the results found from the new sensor. The objectives of the experimental testing are to assess the reconstruction capabilities (Equation 4.5) versus achievable compression ratios (Equation 4.7) when: 1) increasing the number of neuron boards (and filters) in a single sensor node, 2) varying the frequency spacing between filters in a single sensor node, 3) varying the bandwidth in the filters in a single sensor node, and 4) varying the maximum amplitude of the input signal.

The achievable compression ratio, *CR*, is defined in Equation 3.10 and restated here as,

$$CR = 1 - \frac{NB_C}{NB_S} \tag{4.7}$$

where NB_C is the number of bits transmitted through the cochlea-inspired wireless sensor and NB_S is the number of bits transmitted for a traditional Nyquist-sampled 16-bit data acquisition system. Because the signals of interest in this study are typically concentrated at low frequencies (<10Hz), it is assumed that the Nyquist-sampled signal is sampled at 20Hz by a traditional wireless sensor. However, to enable real-time processing of the signal, it is assumed that once the traditionally sampled signal receives a new data point it immediately broadcasts the data across the network and to the network's base station. As such, both the cochlea-inspired wireless sensor and the traditional wireless sensor have the same packet overhead for each data point and only the packet payloads are considered. Additionally, it is assumed that the traditionally sampled signal is sent as two-byte integers (based on a 16-bit analog-to-digital converter) while the cochlea-inspired sensor node sends one encoded byte of data.

When designing the optimal filter bank, it is desirable to minimize the reconstruction error while maximizing the compression ratio. Intuitively, however, these two metrics are competing in that adding more neuron boards to the sensing node should result in a better approximation of the input signal (to a certain point), thus reducing the

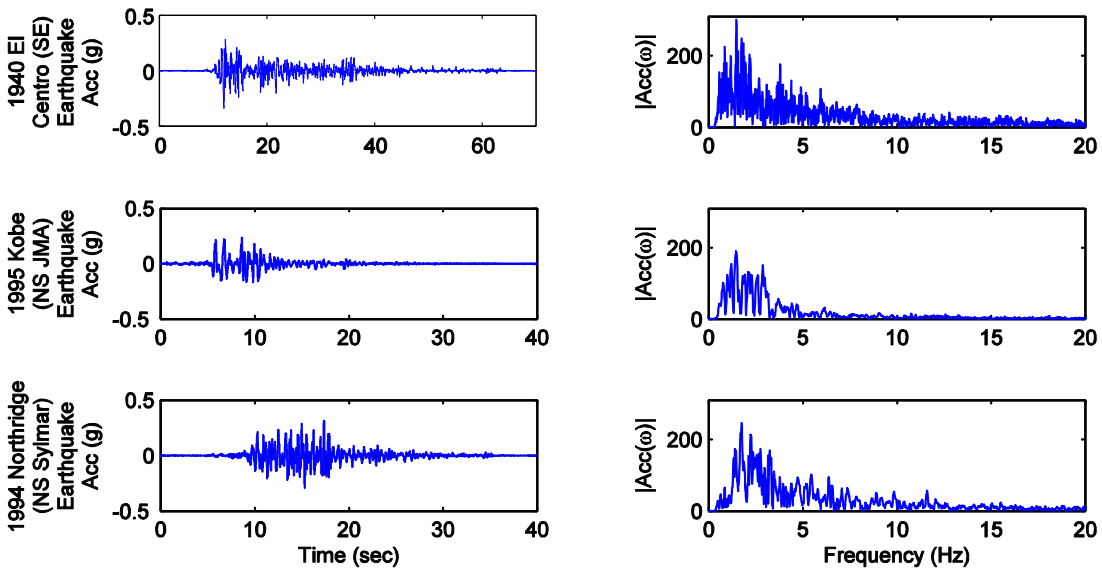

(a) (b)

Figure 4-11. Seismic signals used as input in optimization of wireless sensor node on test-bed in time (a) and frequency (b) domains.

reconstruction error, but also increases the data flow and reduces the compression ratio. Therefore, a balance must be found between these two competing parameters.

4.4.1. Monitoring Seismic Ground Motion

A cochlea-inspired wireless sensor node is installed directly on the shake table to monitor the peak ground accelerations for each input signal. Parameters of this sensing node are varied to determine the effect of these modifications on the reconstruction error and compression ratio. Three signals (1940 El Centro earthquake - 0.4g peak ground acceleration (PGA), SE, 1995 Kobe earthquake - 0.25g PGA, JMA NS, and 1994 Northridge earthquake - 0.25g PGA, Sylmar County Hospital NS) are input to the shake table test-bed to simulate seismic ground motion (Figure 4-11). If these signals are acquired using traditional Nyquist-sampling at 20 Hz with a 16-bit ADC, this results in 1,200 2-byte integers for the El Centro earthquake (60 seconds), 600 2-byte integers for the Kobe earthquake (30 seconds), and 600 2-byte integers for the Northridge earthquake (30 seconds). These values are used when comparing against the number of bytes

transmitted for the cochlea-inspired wireless sensor node in order to determine the compression ratio.

To determine the effect of the number of filter boards on the reconstruction error and compression ratio, the number of filter boards in the wireless sensor node are varied while maintaining a constant bandwidth and filter spacing of 0.35Hz and 0.5Hz, respectively. The number of neuron boards (and therefore, the number of filters) is varied from 4 to 25 for each of the three input signals to determine the optimal number of filter boards for seismic monitoring. Neuron boards are added in consecutive order, thus increasing the total bandwidth of the entire filter bank with each addition. When considering all three input signals, a parabolic relationship is seen between the number of boards and the reconstruction error, with having too few of boards or too many boards resulting in larger errors (Figure 4-12a). As seen in the radio contention analysis, adding more boards at higher frequencies increases radio contention and risks transmitting low amplitude peaks over larger detected values from other boards. Having too few of boards risks not capturing the full frequency spectrum of the input signal.

This effect is exemplified by considering reconstruction error as a function of the earthquake's cumulative spectral energy density, $E_s(f)$,

$$E_s(f)=\left(\sum_{i=1}^{f}|U(f_i)|^2\right)\cdot\left(\sum_{i=1}^{N/2}|U(f_i)|^2\right)^{-1} \tag{4.8}$$

where $U(f)$ is the discrete Fourier transform of $u(t)$, N is length of $u(t)$ when sampled at an interval Δt, and the frequency, f, indexes from 1 to $N/2$. For each test, the spectral energy density of the earthquake is calculated at the center frequency of the highest frequency filter, F_{max}, and compared with the corresponding reconstruction error (Figure 4-12b, Table 4-3). For example, when using 8 boards the largest on-board center frequency of all the filters, F_{max}, is 4Hz and the El Centro earthquake has a cumulative spectral density of 0.75 at this frequency. From this comparison it is clear that adding boards beyond 95% or having fewer boards than 85% of the earthquake's frequency content only has detrimental effects on the reconstruction capabilities.

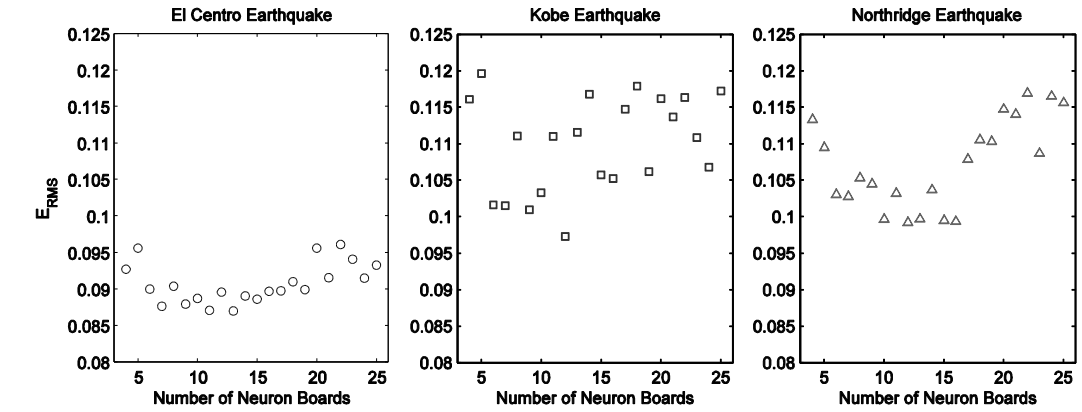

(a)

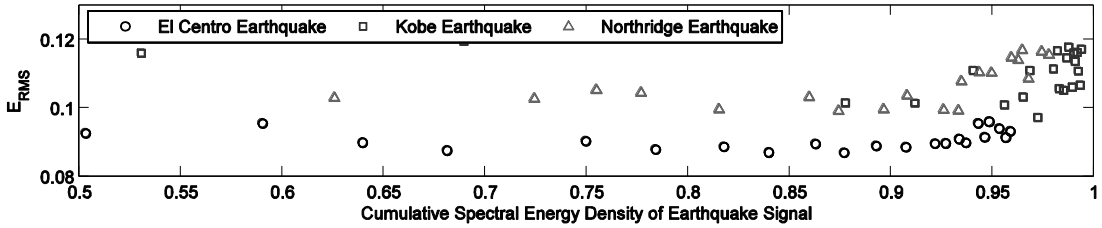

(b)

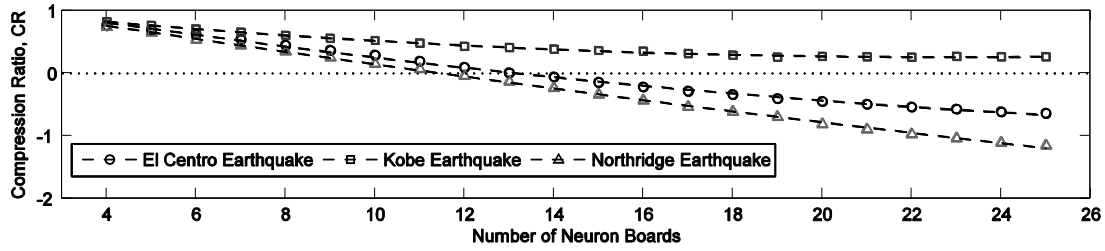

(c)

Figure 4-12. Effect of number of neuron boards on reconstruction error (a), the relation of the reconstruction error to the energy density of the signal (b), and the compression ratio (c) when monitoring three seismic ground motions. Results are based on neuron boards spaced at 0.5Hz with bandwidth of 0.35Hz.

Increasing the number of boards also has a detrimental effect on the overall compression ratio of the system as this results in more boards sending information to the centralized location (Figure 4-12c). Therefore, designing the wireless sensor node such that its maximum frequency range falls within 85% to 95% of the input signals frequency content while limiting the compression ratio is optimal. To comply with these two constraints, 12 boards are chosen as the optimal design, giving F_{max} equal to 6Hz. This

Table 4-3. Cumulative spectral energy density, $E_s(f)$, for variable number of filters and three earthquake signals: El Centro earthquake (*EC*), Kobe earthquake (*K*), and Northridge earthquake (*NR*).

Number of Filters	F_{max} (Hz)	$E_s(f)$ - *EC*	$E_s(f)$ - *K*	$E_s(f)$, - *NR*
4	2.0	0.503	0.531	0.302
5	2.5	0.590	0.689	0.496
6	3.0	0.640	0.877	0.626
7	3.5	0.681	0.912	0.724
8	4.0	0.750	0.940	0.755
9	4.5	0.784	0.956	0.777
10	5.0	0.818	0.965	0.815
15	7.5	0.907	0.983	0.926
20	10.0	0.943	0.990	0.959
25	12.5	0.959	0.994	0.978

does extend beyond this specified spectral range of the Kobe earthquake but this earthquake has a small frequency spectrum with 85% of its energy content below 3Hz.

Next, the effect of varying the filter spacing when monitoring ground motions is explored while holding the filter bandwidth constant. The filter spacing, Δf, is varied from 0.5Hz to 1.0Hz in 0.1Hz increments and the bandwidth of the filters, ξ, is determined by multiplying the filter spacing by 0.707 and rounding to the nearest 0.05Hz increment, so as to provide overlap between the filters without extreme redundancy. The number of filter boards, N_B, is controlled by the previously determined F_{max}, where

$$N_B = \Delta f \left\lceil \frac{F_{max}}{\Delta f} \right\rceil \tag{4.9}$$

and $\lceil \cdot \rceil$ is the ceiling function. In general, varying the filter spacing between 0.5Hz and 0.7Hz did not have a significant impact on the reconstruction error (Figure 4-13). However, for spacing above 0.7Hz, increasing the filter spacing decreases the number of filters and results in each neuron board representing a wider frequency band and giving a cruder signal approximation as shown by the increase in E_{RMS}. Additionally, due to the filter bank design, as the filter spacing increases the filter bank is unable to accurately represent frequencies below 0.7Hz and this increases the overall signal distortion, thus increasing the error. As anticipated, however, increasing the filter spacing and therefore

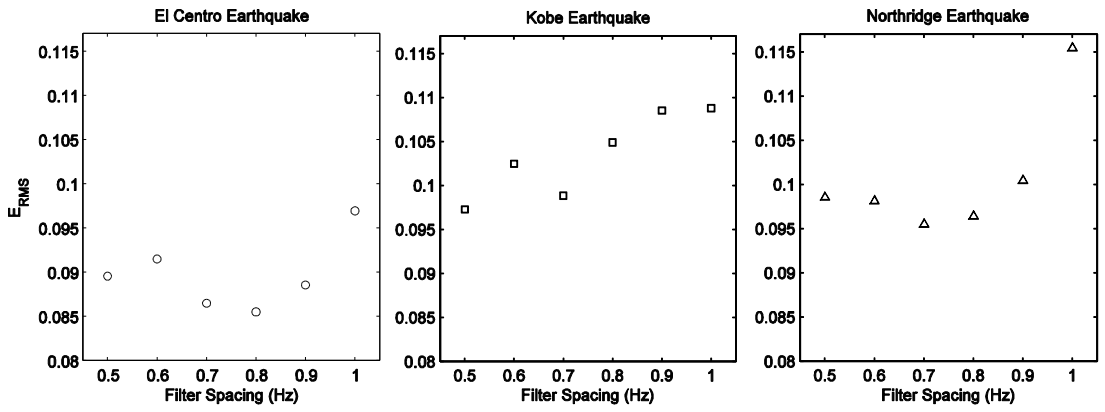

(a)

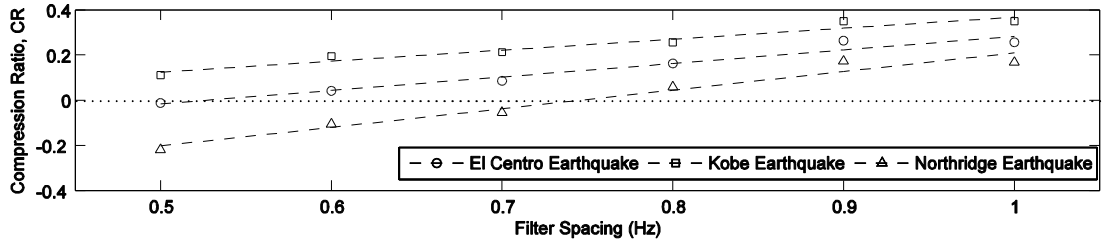

(b)

Figure 4-13. Effect of filter spacing on reconstruction error (a) and compression ratio (b) when monitoring three seismic ground motions. Bandwidth varies as a scaled function of the filter spacing and the number of boards is varied to ensure that the maximum band-pass center frequency is approximately 6Hz.

decreasing the number of boards does increase the compression ratio as less data is transmitted cumulatively from all the boards. For the three seismic signals a filter spacing of 0.7Hz produces minimal reconstruction and an acceptable compression ratio and therefore, is used as the filter spacing for the remaining tests.

Finally, using the results found from the two previous analyses (0.7Hz spacing with 9 boards spanning from 0.7 to 6.3Hz), the effect of varying the bandwidth is explored. The bandwidth is varied from half of the filter spacing, 0.35Hz, to a full filter spacing, 0.7Hz, in 0.05Hz increments. As the bandwidth is varied the reconstruction error varies with a parabolic relationship (Figure 4-14). For small bandwidths the filters do not have high overlap and therefore, may miss some frequencies but large bandwidths result in large redundancy between filters. This overlap in frequencies results in more transmitted information and therefore decreases the compression ratio of the wireless

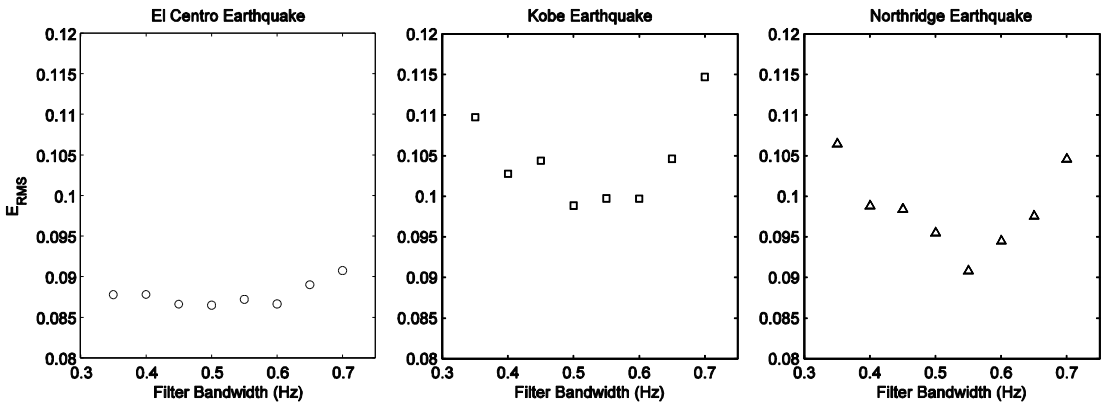

(a)

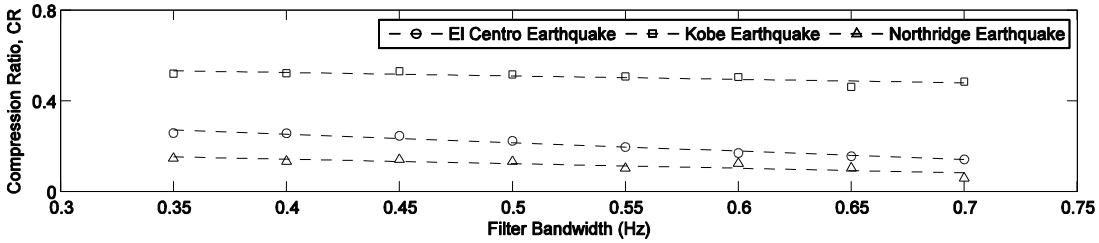

(b)

Figure 4-14. Effect of filter bandwidth on reconstruction error (a) and compression ratio (b) when monitoring three seismic ground motions. Filter spacing is held constant at 0.7Hz and number of filter boards is 9.

sensor node. Using 0.5Hz bandwidth, the filter design has optimal overlap and results in a cumulative minimum reconstruction error for all three input signals.

The 0.4g El Centro earthquake is used as an example signal for illustrating the performance of the sensors when monitoring ground accelerations (Figure 4-15). First, the compressive strategies employed by the cochlea-inspired sensor node are not lossless and therefore, perfect reconstruction of the signal is not achieved. From this compression process, a normalized reconstruction error of 0.0865 for the earthquake signal is incurred in the time domain and 0.0135 in the frequency domain. Additionally, for this signal, the 9 filter sensor detected 1,867 peak values (or 1-byte encoded values). If the signal had been sampled using traditional Nyquist sampling (at 20Hz) 1,200 two-byte integers would have been collected. Therefore, the cochlea-inspired sensor achieves a compression ratio of 22.2% when comparing the number of transmitted bits.

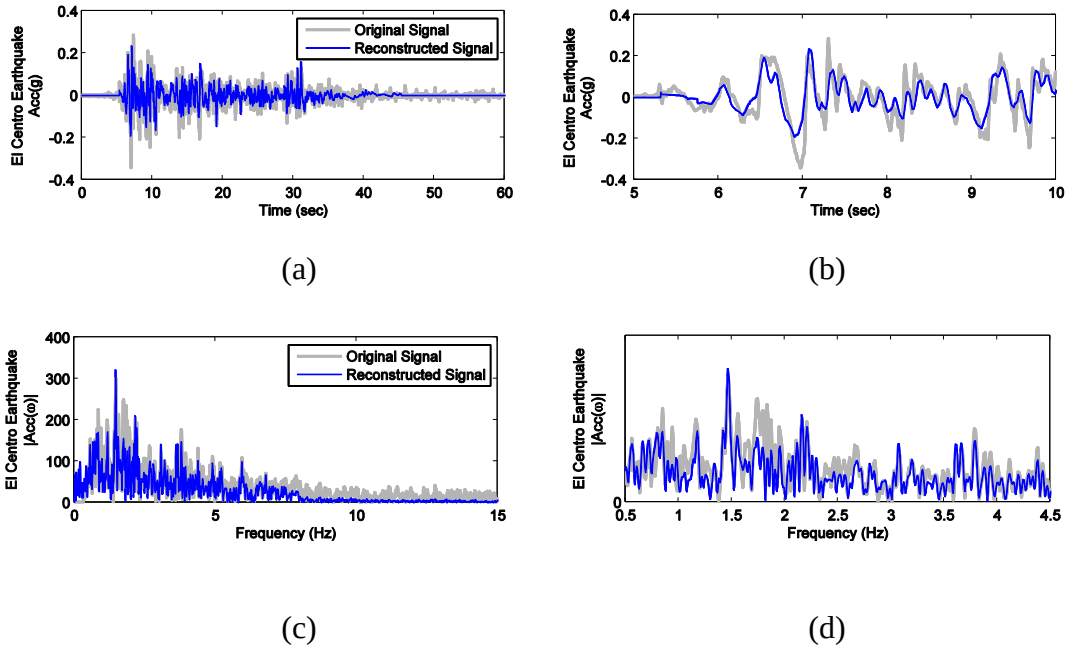

Figure 4-15. Signal reconstruction of El Centro ground acceleration using cochlea-inspired sensor in the full time-domain (a), a sub-scale in the time-domain (b), a full-scale in the frequency domain (c), and a sub-scale in the frequency domain (d).

Using the optimal filter bank (9 filters, 0.7Hz spacing, and 0.5Hz bandwidth), the effect of various peak ground accelerations (PGAs) is also explored for the three earthquake signals (El Centro earthquake: PGA of 0.4g and 0.28g, Kobe earthquake: PGA of 0.25g and 0.083g, and Northridge earthquake: PGA of 0.3g and 0.1g). For these signals when an earthquake signal's amplitude is increased the reconstruction error decreases and the compression rate decreases (Table 4-4). This is because as the input signal's amplitude decreases more peak values go undetected due to rounding errors in the 10-bit ADC as well as limitations in the peak-picking algorithm. This results in an increase in reconstruction error by 10.4% for the El Centro earthquake, 115.7% for the Kobe earthquake, and 66.0% for the Northridge earthquake when considering the difference between the reconstruction error of the two signals over the reconstruction error of the maximum amplitude signal. Correspondingly, the compression ratio increases by 53.2%, 60.9%, and 331.5% when comparing the difference between the small amplitude signals and the large amplitude signals for all three signals. While the improvement in compression ratios does result in some power savings due to a decrease in the number of sent packets it comes at the expense of reconstruction capabilities as less

information about the signal is transmitted. To alleviate some of these challenges it is important to properly outfit the cochlea-inspired wireless sensor node with appropriate transducer technology, thus taking advantage of the full-range of the microprocessor's 10-bit ADC. Alternatively, the gain of the band-pass filter can be increased in order to amplify the input signal.

Because both the traditional wireless sensor method and the new cochlea-inspired wireless sensor method use the same radio packet structure, the true power savings is considered through the number of packets sent. As such, the power consumption of the cochlea-inspired sensor node is compared to two state-of-the-art wireless sensor nodes that have been successfully deployed on numerous civil infrastructure: Crossbow's *iMote2* with peripherals developed by the University of Illinois-Champaign (Nagayama *et al.* 2007; Jang *et al.* 2010; Rice *et al.* 2010) and the *Narada* developed at the University of Michigan (Swartz *et al.* 2005; Kim and Lynch 2012; Kurata *et al.* 2013). The *iMote2* with its SHM-A peripheral consumes 756mW of power at 4.5V when in transmitting mode (Rice *et al.* 2010), while the *Narada* consumes 375mW of power at 5V in transmitting mode (Kurata *et al.* 2013). On the other hand, the cochlea-inspired sensor with 9 boards consumes 57.0mW of power at 1.8V in transmitting mode. To compare the three sensor nodes, the amount of power consumed is considered only during data transmission when energy consumption is the largest and it is assumed that a packet can be sent from any of the three sensor nodes in 2msec. As an example, if the 1,200 data points found from the El Centro earthquake are transmitted using traditional means, the *iMote2* consumes 1.81J of energy (= 756mW x 2msec/packet x 1,200 packets) while the *Narada* consumes 0.86J of energy (= 356mW x 2msec/packet x 1,200 packets). On the other hand, the cochlea-inspired sensor consumes 0.21J of energy (57.0mW x 2msec/packet x 1,867 packets), thus using only 11.7% and 24.9% of the *iMote2*'s and *Narada*'s energy consumption, respectively. This trend can be seen for all six signals with the cochlea-inspired sensor node having large power savings as compared to the traditional modes of wireless data collection (Table 4-4). Therefore, by choosing low-power components the sensor node is still able to achieve significant power savings with real-time processing.

Table 4-4. Comparison of the effect of input signal amplitude when monitoring seismic ground motion. Note that the power ratio is the power consumed by the cochlea-inspired sensing node divided by the power consumed by the respective traditional sensing node.

	Reconstruction Error, *E*	Compression Ratio, *CR*	Power Ratio compared to *iMote2*	Power Ratio compared to *Narada*
0.4g El Centro Earthquake	0.0865	22.2%	12.4%	26.4%
0.28g El Centro Earthquake	0.0955	34.0%	10.5%	23.4%
0.3g Kobe Earthquake	0.0988	51.6%	7.7%	16.4%
0.1g Kobe Earthquake	0.2131	83.0%	2.7%	5.8%
0.4g Northridge Earthquake	0.0955	13.0%	13.9%	29.5%
0.28g Northridge Earthquake	0.1585	56.1%	7.0%	14.9%

By directly monitoring seismic ground motions, the effect of varying the number of filters, the filter spacing, and the bandwidth was explored. It was shown that the number of filter boards can be chosen by designing the filter bank on the wireless sensor node to encompass approximately 85% to 95% of the energy content of the signal. Additionally, the filter spacing and filter bandwidth can be chosen by maintaining optimal overlap of the filters in the frequency domain. While these characteristics are signal dependent, slight variations in these values do not have a large impact on the reconstruction error or compression ratio and can be approximated according to a specific subset of input signals (*e.g.*, seismic events with high energy concentrations below 10Hz).

4.4.2. Monitoring Structural Response to Seismic Ground Motions

To validate the cochlea-inspired sensor for a variety of input signals, the structural response of the single-span bridge excited by seismic ground motions is also monitored

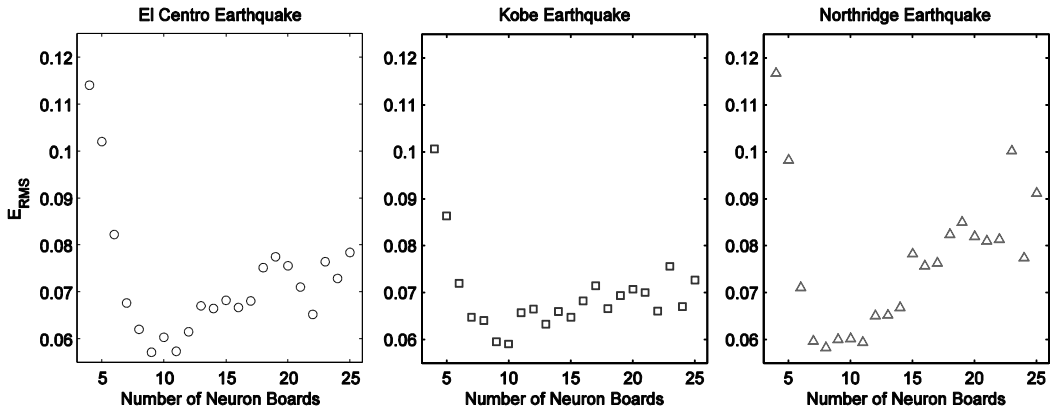

(a)

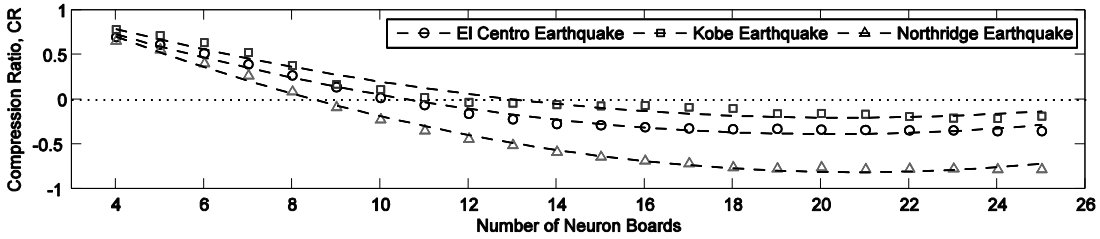

(b)

Figure 4-16. Effect of number of neuron boards on reconstruction error (a) and the compression ratio (c) when monitoring a structure's response to three seismic ground motions. Results are based on neuron boards spaced at 0.5Hz with bandwidth of 0.35Hz.

by placing a cochlea-inspired wireless sensor node on the structure (Figure 4-10c, d). Similar trends for the filter bank parameter optimization that were seen when monitoring pure seismic ground motions are found when monitoring the structural response subject to seismic ground motion (Figure 4-16, Figure 4-17, Figure 4-18). Because the signal is more narrowband than the pure seismic signals, fewer filter boards are necessary to capture the full frequency spectrum of the signal, resulting in initially 10 boards at 0.5Hz spacing being the optimal configuration when varying the number of filter boards (Figure 4-16). For the structural response, the relationship between the number of filter boards and input signals spectral energy content was not quantified due to the narrowband characteristics of all of the input signals. As with the pure seismic signal, the number of filter boards affects the maximum filter bank bandwidth and using this parameter the filter spacing was varied, resulting in an optimal spacing of 0.7Hz when using 8 boards

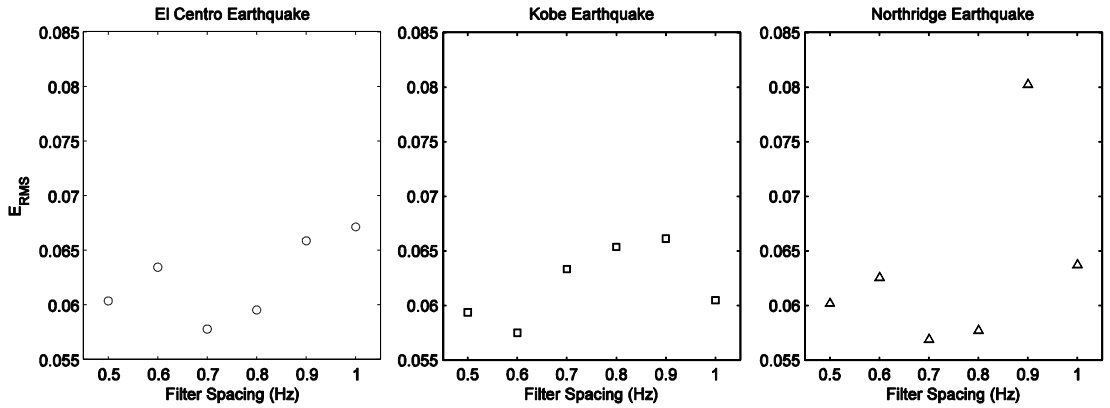

(a)

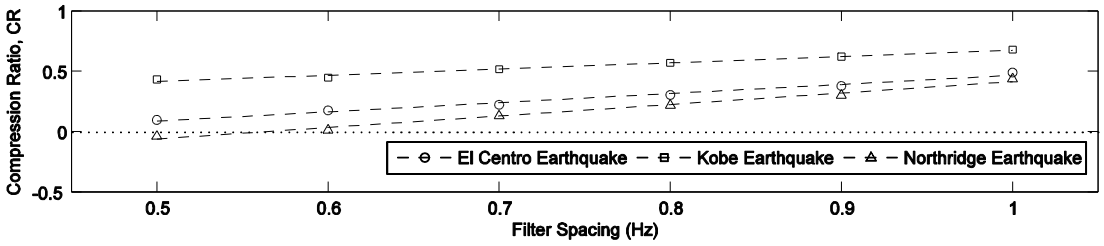

(b)

Figure 4-17. Effect of filter spacing on reconstruction error (a) and compression ratio (b) when monitoring a structure's response to three seismic ground motions. Bandwidth varies as a scaled function of the filter spacing and the number of boards is varied to ensure that the maximum band-pass center frequency is approximately 6Hz.

(Figure 4-17). Finally, the filter bandwidth was optimized to 0.5Hz (Figure 4-18), making the optimal filter bank design 8 boards that are spaced at 0.7Hz with a bandwidth of 0.5Hz. Using the 0.4g El Centro earthquake as an example signal (Figure 4-19), this wireless sensor node transmits 2,193 one-byte peak values, as compared to the 1,200 two-byte integers that would have been collected using traditional Nyquist sampling (at 20Hz). Therefore, the cochlea-inspired sensor is able to achieve a compression ratio of 8.62%. However, the compressive strategies employed by the cochlea-inspired sensor node, are not lossless and therefore, perfect reconstruction of the signal is not achieved, with 0.0578 and 0.0048 reconstruction error incurred in the time and frequency domains, respectively.

Again, all six vibratory signals are used as input signals to the sensor (using 8 filters, 0.7Hz spacing and 0.5Hz spacing) to determine the effects of signal amplitude on

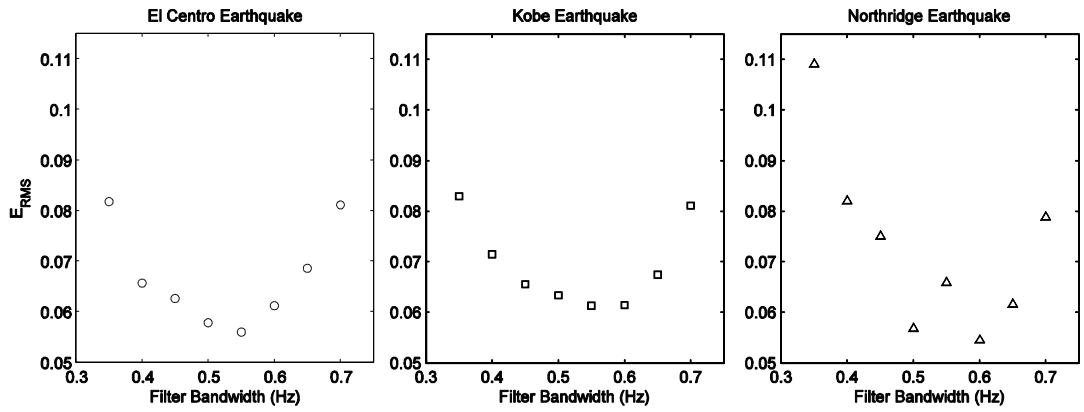

(a)

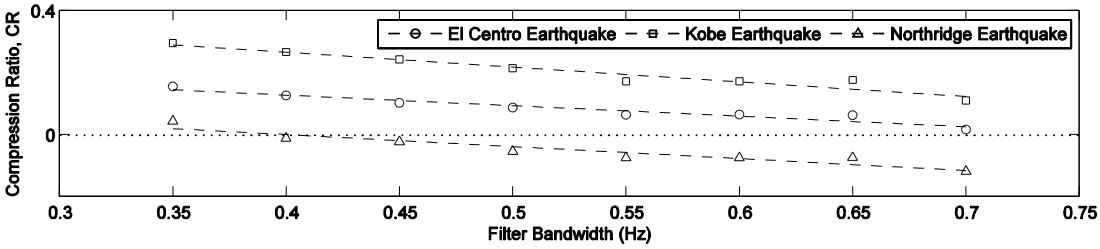

(b)

Figure 4-18. Effect of filter bandwidth on reconstruction error (a) and compression ratio (b) when monitoring a structure's response to three seismic ground motions. Filter spacing is held constant at 0.7Hz and number of filter boards is 9.

the reconstruction capabilities. When considering the input signal's maximum amplitude, it was found that decreasing the amplitude increases the reconstruction error and decreases the compression rate (Table 4-5) as seen with the pure seismic ground motions. This reconstruction error increases by 12.1% for El Centro earthquake, 316% for the Kobe earthquake, and 78.9% for the Northridge earthquake. For both the seismic signals and the structural response to seismic signals, the Kobe earthquake experiences extreme degradation when decreasing the amplitude of the signal because the resulting filtered signals have very low amplitudes, thus leaving many of the peak values undetected by the microcontroller. As such, when configuring the wireless sensor node, some *a priori* knowledge of the approximate range of the input signal is desirable in order to fully utilize the capabilities of the node. In general, the compression ratio significantly increases when decreasing the signal amplitude, as seen with the pure seismic signals. Additionally, in one case the compression ratio was negative indicating that the cochlea-

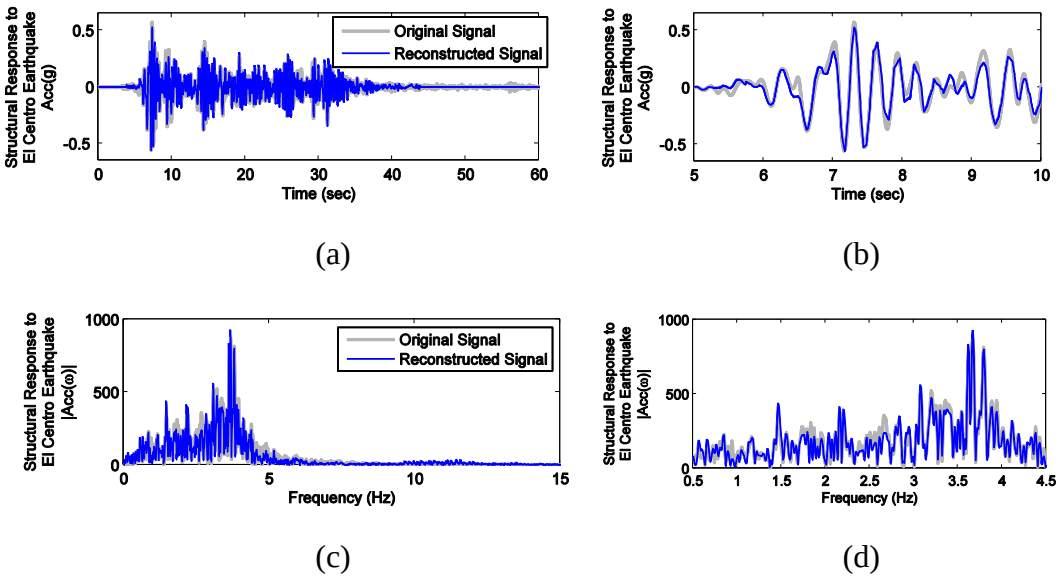

Figure 4-19. Signal reconstruction of El Centro ground acceleration using cochlea-inspired wireless sensor in the full time-domain (a), a sub-scale in the time-domain (b), a full-scale in the frequency domain (c), and a sub-scale in the frequency domain (d).

inspired sensor node transmitted more data than the Nyquist method. This increase in transmitted data, however, is again offset by reductions in overall power consumption as compared to the traditional wireless sensor nodes (Table 4-5). Using the El Centro earthquake as an example, when comparing the power consumption of the cochlea-inspired sensor node during data transmission with the *iMote2* and *Narada*, the proposed sensing node consumes 0.25mW per packets and therefore, uses only 13.5% and 28.7% of the traditional sensing nodes energy, respectively. The other five signals saw similar power savings.

4.5. Chapter Summary

In this chapter a low-power, modular sensor node was developed based on the functionality and capabilities of the mammalian cochlea. Using the mechanisms employed by the auditory system as inspiration, the sensor performs three steps in real-time: 1) decompose the signal into frequency components, 2) condense the decomposed signal through linear encoding, and 3) transmit the data wirelessly to a centralized

Table 4-5. Comparison of the effect of input signal amplitude when monitoring structural response to seismic ground motion. Note that the power ratio is the power consumed by the cochlea-inspired sensing node divided by the power consumed by the respective traditional sensing node.

	Reconstruction Error, *E*	Compression Ratio, *CR*	Power Ratio compared to *iMote2*	Power Ratio compared to *Narada*
0.4g El Centro Earthquake	0.0578	8.7%	13.5%	28.7%
0.28g El Centro Earthquake	0.0648	19.0%	12.0%	25.5%
0.3g Kobe Earthquake	0.0663	20.8%	11.7%	24.9%
0.1g Kobe Earthquake	0.2758	54.4%	6.7%	14.3%
0.4g Northridge Earthquake	0.0568	-5.5%	15.5%	33.1%
0.28g Northridge Earthquake	0.1016	29.6%	10.4%	22.1%

location. By employing these techniques, the sensor uses parallel processing to compress transmitted data in real-time with acceptable signal distortion in the time and frequency domains. This new cochlea-inspired sensor was built in hardware and was used to monitor both seismic ground accelerations and the response of a single-span bridge when subject to such accelerations. The number of filters, filter spacing, and filter bandwidth were systematically varied to determine their effect on the reconstruction error and compression ratio. The wireless sensor node performs optimally when the number of filters is large enough to encompass 85% to 95% of the energy spectrum of the input signal and when the filters have enough overlap to capture the frequency content of the signal without transmitting large amounts of redundant data. The versatility of the sensor was addressed by applying a variety of seismic signals with various amplitudes and overall the sensor was proved successful on the set of seismic signals. In general, a high degree of compression was achieved for the seismic motions studied (ranging from 8% to

80%) but in one case, more data was transmitted than in a traditional Nyquist sampling approach, resulting in a negative compression rate.

When considering power consumption, the cochlea-inspired wireless sensor demonstrated cumulative power savings over traditional wireless sensors. In this way, the proposed cochlea-inspired sensor node addresses the power limitations of current wireless sensor nodes and would be able to function for longer periods without the use of sleep modes. Of this power consumption, a considerable amount can be attributed to the digital radio, which for example, consumes 82.6% of the power on a 9-board sensing node. As such, future work will focus on interfacing the cochlea-inspired wireless sensor node with alternative non-digitized radio options in order to further reduce the power consumption of the node. By reducing this number, the proposed cochlea-inspired sensor will be more effective in the field and will be able to better address the energy concerns of wireless sensor networks.

CHAPTER 5

REAL-TIME CONTROL OF CIVIL INFRASTRUCTURE USING WIRELESS SENSOR NETWORKS BASED ON BIO-MIMICRY OF THE BIOLOGICAL SENSORY SYSTEM

5.1. Introduction

In this chapter, the cochlea-inspired wireless sensor is applied to a control application, thus leveraging the spectral decomposition capabilities of the node and enabling real-time control. Traditional control has been plagued by inherent delays within the algorithm implementation due to time requirements for data aggregation and computations. Initially, control systems relied on centralized data processing to mitigate global vibrations. For example, many researchers have explored the use of active mass dampers (AMDs) or hybrid mass dampers (HBDs) for the purposes of seismic or wind mitigation (Spencer *et al.* 1997) in buildings. These systems, however, typically relied on a series of distributed sensors and a single controller, thus requiring all information to be aggregated at a centralized location prior to any control decision being made. By relying on a single controller for the entire system, the overall control capability and effectiveness \is greatly reduced. These systems were extended to include multiple controllers and actuators but without sufficient information sharing between the controllers they were still only capable of localized actuation and cannot make global decisions (Dyke *et al.* 2003). Such initial control systems greatly advanced the application of structural control for civil infrastructure, but with their limited localized actuation and inherent delays due to data aggregation and processing at a centralized repository, alternative options for localized processing and actuation were necessary.

To overcome these challenges, the structural control community explored the use of wireless telemetry as a means of enabling communication between nodes (*i.e.*, the controller and the sensors) within a network, thus enabling global information sharing. As these new sensor nodes are typically lower cost than their tethered counterparts (Celebi 2002), a dense network of nodes could now easily be deployed, thus resulting in a rich overview of the structure's response to external and internal loads and enabling decentralized control. Even with the addition of this technology, however, structural control was still inhibited by degradation of real-time control capabilities (as also seen with the tethered systems), risk of data loss due to unreliable communication, and sub-optimal control laws due to the decentralization (Wang *et al.* 2007). While these limitations have not been entirely addressed, wireless structural control has been validated on a variety of experimental test beds (Lynch *et al.* 2008; Swartz and Lynch 2009; Wang *et al.* 2009). All of these applications, however, have been largely performed within the confines of laboratories and few have extended to real-world structures or long-term deployments. As such, in order to fully implement this technology it is imperative that the current limitations of the technology, in general, as well as its application to structural control be addressed. To overcome the deficiencies found in traditional control of civil infrastructure, whether wired or wireless, inspiration will be drawn from biological sensory and actuation systems, thus resulting in a novel bio-inspired control paradigm.

Sensing and actuation within biological systems are streamlined processes which have extremely fast reactive times. Within biological systems, information is received about external stimulus through multiple receptors (Nicholls *et al.* 2001). This information is both disseminated and aggregated across networks of neurons thus enabling rapid and sophisticated decision making through very basic techniques. Receptor neurons transmit their information to layers of processing neurons where the data is further integrated and manipulated until it reaches the motor neuron. Motor neurons receive this information and activate their associated muscles. Because neurons can only perform basic operations (addition, subtraction, multiplication, and some filtering (Herz *et al.* 2006)), based on its received information the motor neuron sends an amplified or attenuated command to the muscle thus enabling rapid actuation based on an

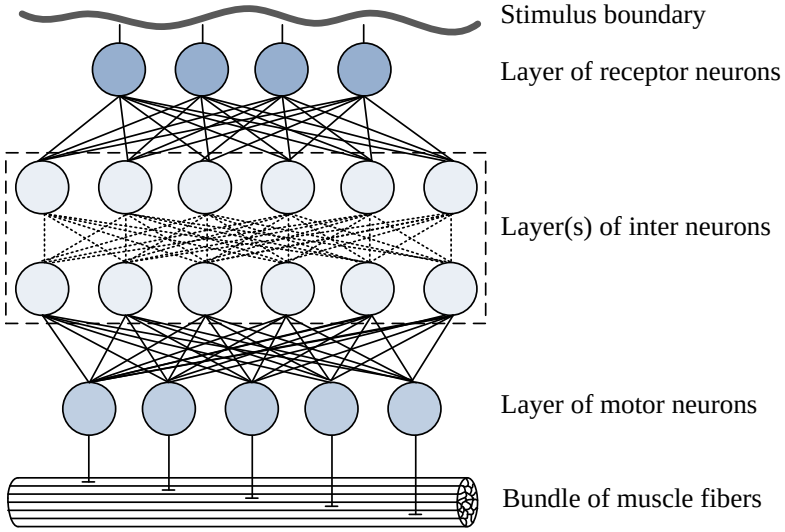

Figure 5-1. Complete sensing and actuation process in biological sensory systems.

input signal. In this chapter, inspiration is drawn from the processes utilized by biological sensory and actuation systems to overcome the limitations found in equivalent engineering systems. In particular, the previously established cochlea-inspired sensor node will be combined with the actuation techniques employed by motor neurons.

5.2. Actuation in Biological Sensory Systems

Within biological sensory systems, action against perceived stimulus occurs at reflexive speeds and largely outperforms the capabilities of engineering sensing and actuation systems. This process of sensing and actuation starts when information is perceived by various receptors. Each receptor is tuned to a specific response (*e.g.*, frequency range, pressure) and is activated according to the content of the input stimulus (Nicholls *et al.* 2001). Once activated, the receptor passes its received information in the form of electrical pulse trains to the next layer of neurons termed inter neurons. These inter-neurons aggregate information from numerous sources based on the connection type (*i.e.*, excitatory or inhibitory) between the transmitting neuron and the receiving neuron (Figure 5-1). Excitatory connections further promote decisions while inhibitory connections work to inhibit decisions and with each layer of neurons, the information becomes further integrated based on these connection type (Nicholls *et al.* 2001).

Depending on the complexity of the decision making, this process continues through several layers of neurons until reaching the level of motor neurons. For very basic organisms who have a minimal number of neurons, such as the leech or the C. Elegan worm, the hierarchy of neurons, including their inhibitory and excitatory connections, can be mapped out, thus demonstrating the overall sensing and actuation process (Gray *et al.* 2004; Kristan *et al.* 2005). As organisms become more advanced, however, this mapping becomes increasingly complex.

Motor neurons convey information directly to muscles which are responsible for actuation in biological systems (Loeb and Ghez 2000). Similar to connections between two neurons, the connection between the motor neuron and the muscle, called the end-plate, is a chemical synapse. The motor neuron excites the muscle by opening ionic channels at the end plate and initiating a very rapid action potential that runs along the length of the muscle fibers (Loeb and Ghez 2000). Muscles are comprised of bundles of muscle fibers and a single motor neuron can control thousands of these fibers at one time. The connection type between the motor neuron and each muscle fiber, however, plays a strong role in the muscle response. For example, the leech moves by bending its body back and forth (Nicholls *et al.* 2001) and if the leech senses an external pressure on its body it bends away from the perceived stimulus. It has been found that sensory cells in the leech not only transmit information to the excitatory motor neurons on the side of the leech that experiences the stimulus but to the inhibitory motor neurons on the contralateral side of the leech. In doing this, the muscles closest to the stimulus contract while the muscles on the opposite side relax thus allowing a bending motion (Marin-Burgin *et al.* 2008). Without the excitatory and inhibitory motor neurons acting simultaneously, the movement of the leech would not be as effective.

A motor neuron dictates the magnitude of the force to be exerted by using both rate coding and the size principle. First, the motor neuron uses rate coding by sending a series of actions potentials with each successive spike increasing the intensity of the muscle actuation, up to a limit (Pette and Vrbova 1985). Second, to increase the overall intensity of the muscle actuation, motor neurons are recruited in an orderly manner by the motor cortex depending on their physiological properties (Cope and Pinter 1995). As such, the overall intensity of the actuation increases as the number of activated motor

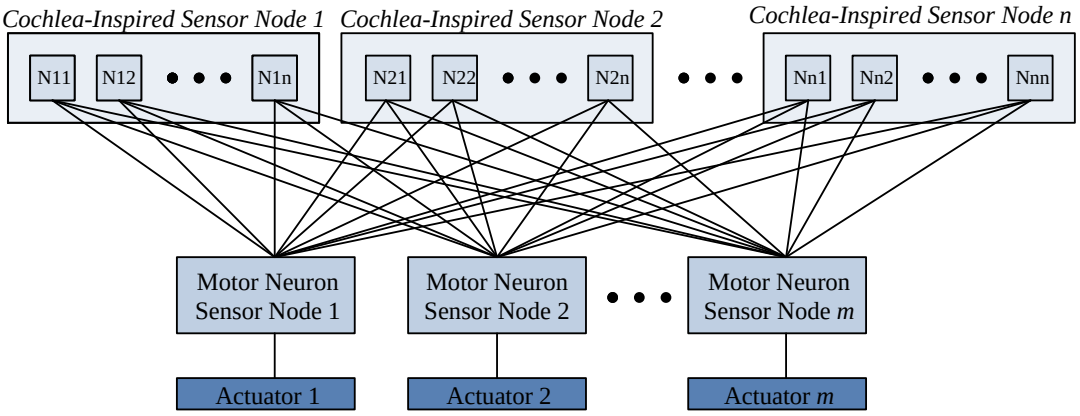

Figure 5-2. Complete sensing and actuation process in bio-inspired sensory system.

neurons increases. Once commands have been sent from motor neurons to the muscle fibers, the neuron uses feedback mechanisms to ensure that the overall desired response is achieved and to fine-tune the actuation based on this information (Wolpert and Ghahramani 2000). This enables effective actuation for a variety of input stimulus. Therefore, all muscle actuation depends on both the commands from motor neurons as well as the connection type between the neuron and the fiber. In this chapter, the simplistic basis by which organisms respond to external stimuli through muscle actuation will be mimicked. In particular, the inhibitory and excitatory connections of these systems will be adapted to establish synaptic strength connections between the previously established cochlea-inspired sensor node and "motor neuron" sensor nodes.

5.3. Bio-Inspired Control of Civil Infrastructure using Cochlea-Inspired Sensor Node

To further explore this bio-inspired actuation, the complete biological process of sensing to actuation will be mimicked in an engineered system. To achieve this, multiple cochlea-inspired sensor nodes (see Chapter 4) act as receptor neurons and perform the initial pre-processing of information (Figure 5-2). As discussed in Chapter 4, each cochlea-inspired sensor node contains multiple on-board neurons that process and transmit data simultaneously. By focusing on information extraction at these low-power nodes through real-time analog pre-processing, the entire control algorithm is highly

streamlined and can overcome the traditional computational inundation that plagues control in civil infrastructure. The control system also benefits from the high energy savings seen by the cochlea-inspired wireless sensor node. These receptor nodes transmit their decomposed information to centralized nodes, which receives this data based on the "synaptic" strength between the receptor unit and the transmitting nodes. These receiving nodes serve as motor neurons within the network of sensors and directly control actuators based on the received information.

5.3.1. Optimal Control Law for Bio-Inspired Control

While this proposed bio-inspired sensing and actuation is appropriate for a variety of applications, this study focuses on controlling the response of lightly damped civil infrastructure, such as buildings and bridges. Because these structures have small damping ratios, they exhibit high sensitivity to modal frequencies and the effect of externally applied loads such as wind or seismic can be extremely detrimental. As such, it is desirable to execute control algorithms that focus on the frequency response of the structure in order to effectively mitigate undesirable excitations due to the applied loads. Numerous algorithms have been developed within the frequency domain that are optimized based on the frequency content of the input signal as well as characteristics of the structure itself. These algorithms include, but are not limited to, the H_2 norm (Suhardjo *et al.* 1992) and the H_∞ norm (Spencer *et al.* 1994). Such algorithm have been applied to a variety of laboratory control applications (Spencer *et al.* 1994; Yang *et al.* 1996), as well as some real-world buildings (Spencer and Nagarajaiah 2003). While these algorithms have proven successful in some environments, they are still largely inhibited by the previously outlined challenges for real-time control on civil infrastructure. In this study, control within the frequency domain will be explored so as to mitigate the detrimental effects of modal excitations but a specific focus on adapting the actuation techniques employed by the biological sensory system to a new bio-inspired actuation system.

To achieve a bio-inspired actuation system, the synaptic strength (*i.e.*, amplification or attenuation factor) between the receptor neurons and the motor neurons

must be established. In biological systems such connections are typically established through years of experiential learning. Due to the rare occurrences of seismic events and their overall short durations using experiential learning to update the synaptic strength of the proposed bio-inspired actuation system would be impractical. Instead, the bio-inspired algorithm will make use of a well-established optimal control, the Linear Quadratic Regulator (LQR) (Kalman 1960), which establishes scaling factors between the input sensor data and the controller output, or actuator force. These scaling factors can be used as the synaptic strengths in the bio-inspired control algorithm. The LQR is a state-feedback controller that seeks to simultaneously minimize the response of the structure and the maximum control force. The LQR solution determines an optimal control force, $\boldsymbol{u}$, through minimizing the performance index, J,

$$J = \int_0^\infty (\boldsymbol{z}^{\mathrm{T}} \boldsymbol{Q} \boldsymbol{z} + \boldsymbol{u}^{\mathrm{T}} \boldsymbol{R}\, \boldsymbol{u}) dt \tag{5.1}$$

where $\boldsymbol{Q}$ and $\boldsymbol{R}$ are symmetric positive semi-definite weighting matrices and $\boldsymbol{z}$ is a vector of the system states. This optimization is dependent on the response of the structure which is assumed to be linear-time invariant and therefore can be modeled through the traditional state space model,

$$\dot{\boldsymbol{z}} = \boldsymbol{A}\boldsymbol{z} + \boldsymbol{B}\boldsymbol{u} \tag{5.2}$$

$$\boldsymbol{y} = \boldsymbol{C}\boldsymbol{z} + \boldsymbol{D}\boldsymbol{u} \tag{5.3}$$

where $\boldsymbol{z} \in \mathbb{R}^m$ is the state vector, $\boldsymbol{y} \in \mathbb{R}^q$ is the output vector, $\boldsymbol{u} \in \mathbb{R}^p$ is the input or control vector, $\boldsymbol{A} \in \mathbb{R}^{m \times m}$ is the system matrix, $\boldsymbol{B} \in \mathbb{R}^{m \times p}$ is the input matrix, $\boldsymbol{C} \in \mathbb{R}^{q \times m}$ is the output matrix, and $\boldsymbol{D} \in \mathbb{R}^{q \times p}$ is the feed-through matrix such that m is the number of states of the system, q is the number of outputs, and p is the number of inputs. Traditional LQR control relies on full-state feedback such that $\boldsymbol{u} = \boldsymbol{K}\boldsymbol{z}$, where $\boldsymbol{K}$ is the resulting constant feedback gain vector and K_i corresponds to the control value associated with the i^{th} state of the system. However, when considering control of civil

infrastructure it is often difficult to monitor all of the states in the system (*e.g.*, displacement, velocity, acceleration) without implementing computationally expensive observers such as the Kalman filter (Welch and Bishop 1995) and therefore, reducing the real-time capabilities of the system. As such, the traditional LQR is adapted for optimal control using output-state feedback, $\boldsymbol{u} = \boldsymbol{Ky}$ (Lewis and Syrmos 1995).

To solve for the optimal constant feedback gains, it is assumed that there exists a positive semi-definite matrix, $\boldsymbol{P}$, such that,

$$\boldsymbol{A_c}^{\mathrm{T}}\boldsymbol{P} + \boldsymbol{P}\boldsymbol{A_c} + \boldsymbol{C}^{\mathrm{T}}\boldsymbol{K}^{\mathrm{T}}\boldsymbol{R}\boldsymbol{K}\boldsymbol{C} + \boldsymbol{Q} = 0 \tag{5.4}$$

where $\boldsymbol{A_c}$ is the closed loop system matrix ($\boldsymbol{A_c} = \boldsymbol{A} - \boldsymbol{BKC}$). If $\boldsymbol{K}$ and $\boldsymbol{Q}$ are known then $\boldsymbol{P}$ can be solved for through the necessary conditions of constraints for the Hamiltonian equation, $\boldsymbol{H}$,

$$0 = \frac{\partial \boldsymbol{H}}{\partial \boldsymbol{S}} = \boldsymbol{A_C^{\mathrm{T}}}\boldsymbol{P} + \boldsymbol{P}\boldsymbol{A_C} + \boldsymbol{C}^{\mathrm{T}}\boldsymbol{K}^{\mathrm{T}}\boldsymbol{R}\boldsymbol{K}\boldsymbol{C} + \boldsymbol{Q} \tag{5.5}$$

$$0 = \frac{\partial \boldsymbol{H}}{\partial \boldsymbol{P}} = \boldsymbol{A_C}\boldsymbol{S} + \boldsymbol{S}\boldsymbol{A_C^{\mathrm{T}}} + \boldsymbol{X} \tag{5.6}$$

$$0 = \frac{1}{2}\frac{\partial \boldsymbol{H}}{\partial \boldsymbol{K}} = \boldsymbol{R}\boldsymbol{K}\boldsymbol{C}\boldsymbol{S}\boldsymbol{C}^{\mathrm{T}} - \boldsymbol{B}^{\mathrm{T}}\boldsymbol{P}\boldsymbol{S}\boldsymbol{C}^{\mathrm{T}} \tag{5.7}$$

where $\boldsymbol{S}$ is a symmetric matrix of Lagrange multipliers and $\boldsymbol{X}$ is the initial condition matrix of random variables (set to be the identity matrix). Using these three equations, $\boldsymbol{K}$ can be found through a gradient-based routine, in which Equations 5.5 and 5.6 are solved using standard Lyapunov procedure and the solution from these two equations are used to compute the gradient of $\boldsymbol{K}$. $\boldsymbol{K}$ is continually updated in this manner until convergence is met. Once the $\boldsymbol{K}$ vector is found then it is used as amplification or attenuation scaling factors that serve as the synaptic strength between the receptor nodes and the motor neuron nodes. In this way, the architecture between the input nodes and the motor neuron nodes remains streamlined and real-time control is achievable.

5.4. Validation of Bio-Inspired Control

The proposed bio-inspired control is validated on an experimental test bed and by employing this method it is anticipated that real-time control will be achieved. Because the structure response signal is pre-processed at the sensing node (*i.e.*, the cochlea-inspired wireless node) through analog circuitry, when information is received at the centralized node it can be easily applied to the actuator without additional processing. As a result, minimal delays are incurred during the control process and overall, a more effective control is achieved.

5.4.1. Experimental Test Bed

The proposed cochlea-inspired sensor node for the purposes of control is verified on a small-scale four-story structure. Each floor of the structure is comprised of a 10.8cm x 30.5cm x 2.54cm plexiglass plate that is connected to adjacent floors by four T6061 aluminum columns of size 25.4cm x 3.8cm x 0.16cm (Figure 5-3a). The structure is attached to a small-scale shake table that is subject to ground motion from an attached modal shaker (MB Dynamics model N1110). Two active mass dampers (AMDs) on Floors 2 and 3 are used to dissipate the inter-story displacement of the structure that results from this ground motion. Each AMD is an aluminum cart that is manufactured by Quanser and equipped with a high quality DC motor and a quadrature encoder, thus enabling high precision control (Quanser). The structure is outfitted with four magnetostrictive linear-position sensors (MTS sensors, C-series core sensor (MTS Sensors 2012)) that are used to measure the inter-story displacement of each floor as well as an accelerometer on the ground level (Figure 5-3b,c). With the inclusion of the two cart masses, Floors 1, 2, 3, and 4 weigh 4.6295kg, 3.8897kg, 3.8897kg, and 2.7698kg, respectively, giving modal frequencies of 1.7Hz, 4.5Hz, 6.9Hz and 8.8Hz, respectively. These frequencies were found theoretically by assuming shear structure behavior but then were also verified experimentally through the frequency response function using an input sine sweep of ground motion (Figure 5-4). The damping of the structure was estimated based on Rayleigh damping (Chopra 2000) by assuming 3.65% damping ratio. This value was experimentally verified using the half-power bandwidth method (Chopra 2000).

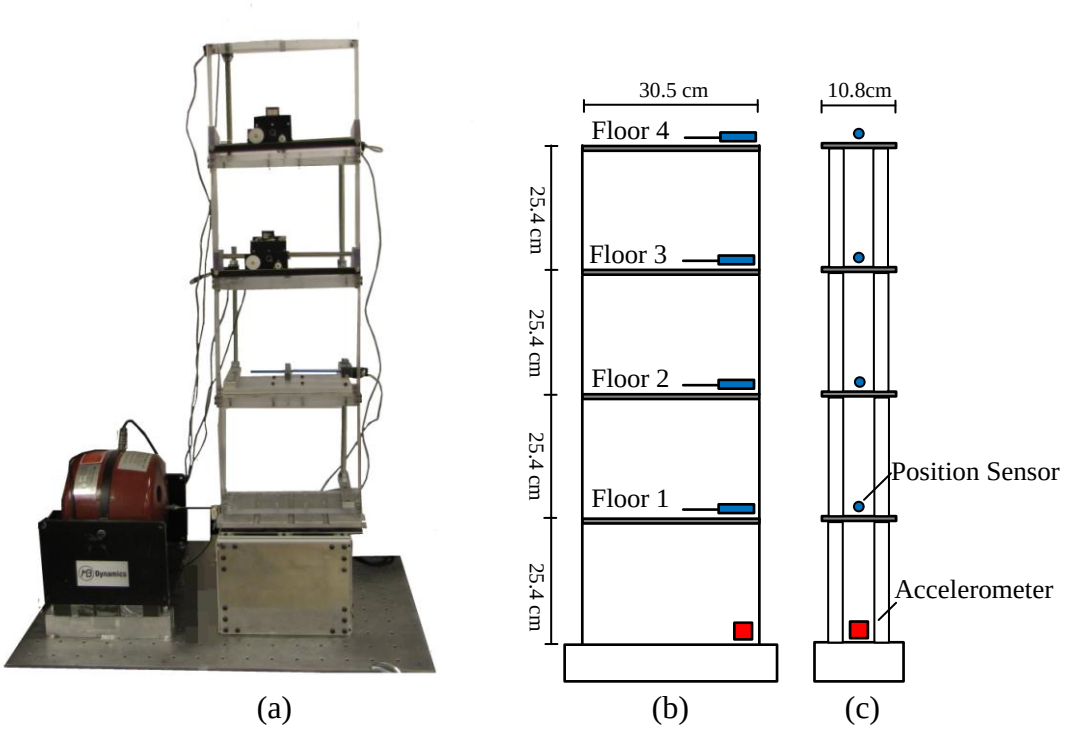

Figure 5-3. Four story test bed that is attached to shake table and MB dynamics modal shaker (a) and test structure schematic front view (b) and side view (c).

The base-excited structural system is modeled in continuous time as a four degree-of-freedom linear time-invariant, lumped mass shear structure which includes the dynamics of the actuator. This can be generalized through the equation of motion for *n* degrees of freedom and *a* actuators as

$$\boldsymbol{M}\ddot{\boldsymbol{x}}(t) + \boldsymbol{C_d}\dot{\boldsymbol{x}}(t) + \boldsymbol{K_s}\boldsymbol{x}(t) = -\boldsymbol{M}\boldsymbol{\iota}\ddot{x}_g(t) + \boldsymbol{F_c}\boldsymbol{u}(t) \tag{5.8}$$

where $\boldsymbol{M}$, $\boldsymbol{C_d}$, and $\boldsymbol{K_s} \in \mathbb{R}^{(n+a)\mathrm{x}(n+a)}$ are the mass, damping and stiffness matrices, respectively. The displacement column vector, $\boldsymbol{x} \in \mathbb{R}^{(n+a)}$, includes each degree of freedom's displacement relative the base of the structure (x_1, ..., x_n) as well as the displacement of the *a* actuators (x_1, ..., x_a). The ground displacement is x_g, $\boldsymbol{\iota} \in \mathbb{R}^{(n+a)}$ is the ground acceleration influence vector, $\boldsymbol{u} \in \mathbb{R}^{a}$ is the vector representing the actuator force that is supplied by the *a* actuators and $\boldsymbol{F_c} \in \mathbb{R}^{(n+a)\mathrm{x}(n+a)}$ is the actuator location matrix. By including the dynamics of the cart, the model encompasses controller-

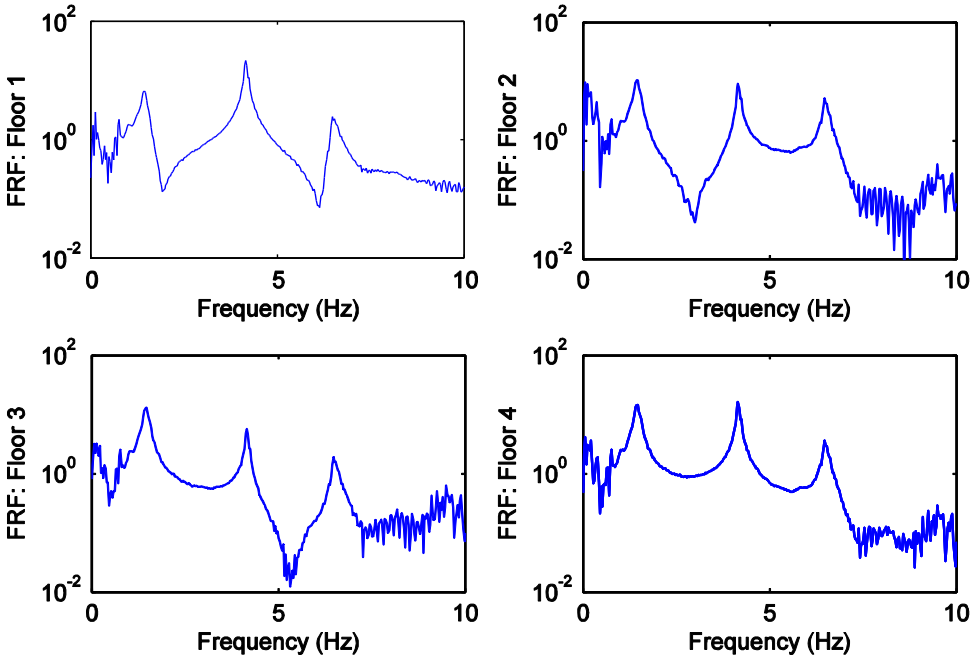

Figure 5-4. Frequency response functions (FRF) of four story structure where the input signal is frequency sweep ground motion and the output is the inter-story displacement of each floor.

structure interaction which can have a significant impact on the control capabilities of the system (Dyke *et al.* 1995). The full representation of Equation 5.8 as it pertains to the four degree-of-freedom system used in this study can be found in the Appendix. This time-domain representation is reformulated in state space as

$$\dot{\boldsymbol{z}}(t) = \boldsymbol{A}\boldsymbol{z}(t) + \boldsymbol{B}\boldsymbol{u}(t) + \boldsymbol{E}\ddot{\boldsymbol{x}}_{\boldsymbol{g}}(t) \tag{5.9}$$

where $\boldsymbol{z}^{\mathrm{T}} = [\boldsymbol{x}^{\mathrm{T}} \quad \dot{\boldsymbol{x}}^{\mathrm{T}}]$, $\boldsymbol{A} = \begin{bmatrix} \boldsymbol{0} & \boldsymbol{I} \\ -\boldsymbol{M}^{-1}\boldsymbol{K}_{\boldsymbol{s}} & -\boldsymbol{M}^{-1}\boldsymbol{C}_{\boldsymbol{d}} \end{bmatrix} \in \mathrm{R}^{2(n+a)\mathrm{x}2(n+a)}$,

$\boldsymbol{B} = [\boldsymbol{0} \quad \boldsymbol{M}^{-1}\mathbf{F}_{\mathbf{C}}]^{\mathrm{T}} \in \mathbb{R}^{2(n+a)\mathrm{x}a}$, $\boldsymbol{E} = [\boldsymbol{0} \quad -\boldsymbol{\iota}]^{\mathrm{T}} \in \mathbb{R}^{2(n+a)}$, $(\cdot)^{\mathrm{T}}$ is the transpose function, and $\boldsymbol{I}$ is the identity matrix.

The output vector is based on the sensors that are available to measure the response of the structure as they relate to the states, **z**, and is represented as a linear sum of the state of the system and the applied control forces,

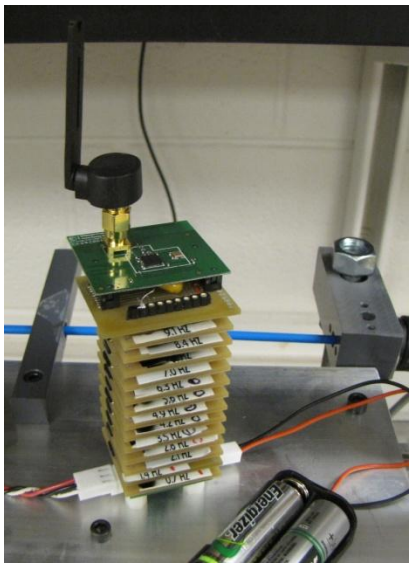

Figure 5-5. Cochlea-inspired wireless sensor node on test bed.

$$\boldsymbol{y}(t)=\boldsymbol{C}\boldsymbol{z}(t)+\boldsymbol{D}\boldsymbol{u}(t)+\boldsymbol{F}\ddot{x}_g(t) \tag{5.10}$$

where $\boldsymbol{C} \in \mathbb{R}^{q\text{x}2(n+a)}$, $\boldsymbol{D} \in \mathbb{R}^{q\text{x}a}$, and $\boldsymbol{F} \in \mathbb{R}^{q}$. Due to the definition of the state space variables, both ***D*** and ***F*** are zero matrices for the four story structure. Additionally, the output matrix, ***C***, is manipulated such that the output variables, **y**(t) represent the inter-story displacement between two successive floors.

5.4.2. Integration with Cochlea-Inspired Sensor Node

To fully exploit the real-time benefits of bio-inspired sensing and control, the test bed sensors (*i.e.*, position sensors) interface with the cochlea-inspired sensor node, thus leveraging its real-time analog pre-processing benefits. The displacement sensor on each floor is read by a unique cochlea-inspired sensor node (Figure 5-5) which then transmits its information to a sensing node that serves as the motor neuron. The *Martlet* (Kane 2013) (Figure 5-6a), developed at the University of Michigan, is chosen as the motor neuron due to its fast processing capabilities, thereby eliminating any further delays within the system. Each motor neuron, or *Martlet*, receives information from all of the neuron boards, integrates that information together and makes an informed control decision. Each *Martlet* directly interfaces with a DC motor controller (Figure 5-6b) such that it can convey the control decision to the AMD Quanser cart.

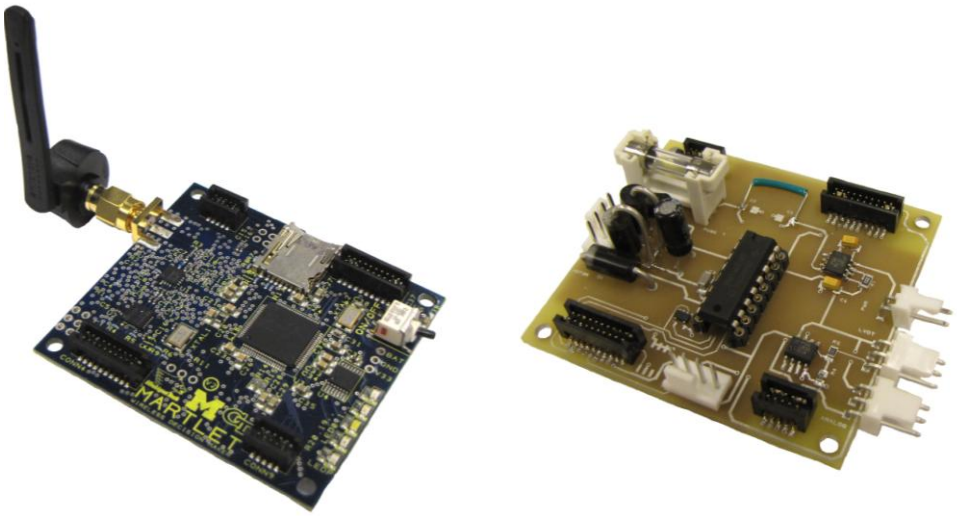

(a) (b)

Figure 5-6. *Martlet* - wireless sensor node used as motor neuron in bio-inspired control (a) and DC motor controller interface board (b).

To optimize the design of each cochlea-inspired sensor node, the bandwidth and frequency spacing of each board within an individual sensing node are designed based on the parametric optimization results of Chapter 4 and therefore are chosen to be 0.5Hz and 0.7Hz, respectively. The number of filter boards, n_f, is determined based on a parametric study that is conducted in simulation in which the number of boards in each sensor node are varied from 5 to 15, resulting in bandwidths of the entire sensor node ranging from 3.5Hz to 14Hz. In this simulation, a single sensor node receives a unique floor's structural response signal when the structure is subject to the El Centro earthquake ground motion. As outlined in Chapters 3 and 4, the sensing node decomposes the signal into its frequency components, implements a peak-picking algorithm, and transmits the resulting peak values in real-time. The peak values from all four nodes are received at a centralized location and each unique signal is reconstructed. The reconstruction error after peak-picking and data transmission for all of these filter bank configurations (*e.g.* 5 filters, 6 filters, 7 filters, *etc.*) is observed in both the time domain, e_T, and frequency, e_F, for each individual floor (Figure 5-7),

$$e_T = \frac{\|x(t)\text{-}r(t)\|}{\|x(t)\|}, \tag{5.11}$$

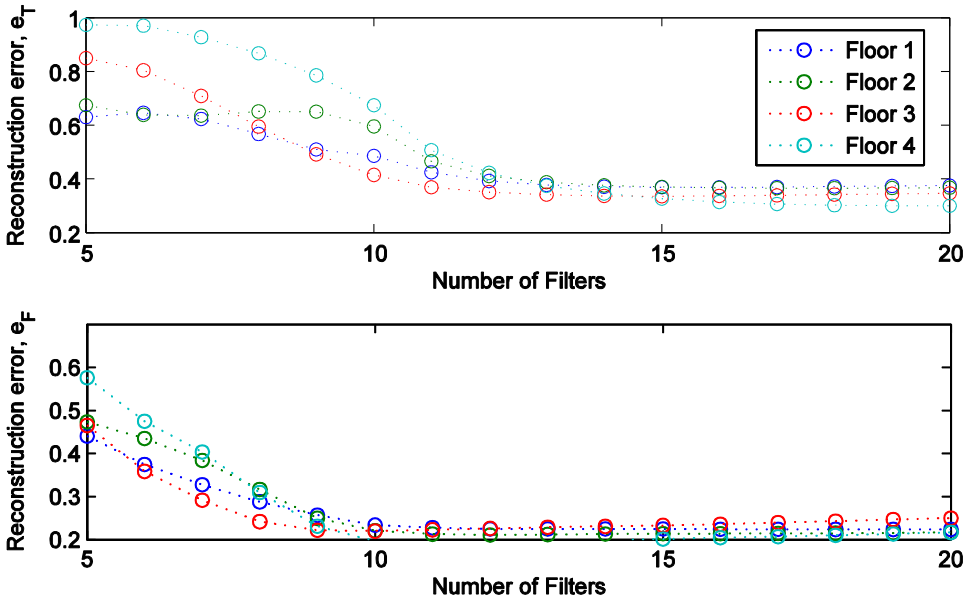

Figure 5-7. Reconstruction error in time, e_T, and frequency domains, e_F, as a function of the number of filter boards in a single sensing node.

$$e_F = \frac{\|X(f)\text{-}R(f)\|}{\|X(f)\|}, \tag{5.12}$$

where $\|\cdot\|$ is the l_2-norm and $x(t)$ is the original floor displacement, $r(t)$ is the reconstructed floor displacement after peak-picking, and $X(f)$ and $R(f)$ are the discrete Fourier transforms of $x(t)$ and $r(t)$, respectively. From this analysis, 12 boards are chosen as the optimal number of boards for each floors as adding additional boards had little impact on the reconstruction error in both the time and frequency domains.

Because the output of each filter board relies on the convolution in the time domain (see Chapter 3), it is more easily represented as a transfer function in the frequency domain, such that convolution becomes multiplication. As such, the transfer function of each i^{th} filter board can be described through the equation,

$$H_i(s) = \frac{2\xi_i\omega_i s}{s^2+2\xi_i\omega_i s+\omega_i^2} \tag{5.13}$$

where the input to the transfer function is the signal that is to be decomposed by the filter (*i.e.*, inter-story displacement), the output of the transfer function is the filtered component (by the i^{th} filter board) of the decomposed signal, ξ_i is the damping ratio of the i^{th} filter, and ω_i is the natural frequency of the i^{th} filter. The dynamics of the entire system including the structure, the actuators, and the sensor nodes can be represented by expanding the state space in Equation 5.9, to now include the states of the cochlea-inspired sensor node,

$$\dot{\boldsymbol{z}}\boldsymbol{z}(t) = \widetilde{\boldsymbol{A}}\boldsymbol{z}\boldsymbol{z}(t) + \widetilde{\boldsymbol{B}}\boldsymbol{u}(t) + \widetilde{\boldsymbol{E}}\ddot{\boldsymbol{x}}_{\boldsymbol{g}}(t) \tag{5.14}$$

$$\boldsymbol{y}\boldsymbol{y}(t)=\widetilde{\boldsymbol{C}}\boldsymbol{z}\boldsymbol{z}(t)+\widetilde{\boldsymbol{D}}\boldsymbol{u}(t)+\widetilde{\boldsymbol{F}}\ddot{x}_g(t) \tag{5.15}$$

where $\boldsymbol{z}\boldsymbol{z}^{\mathrm{T}} = \begin{bmatrix}\boldsymbol{x}^{\mathrm{T}} & \boldsymbol{x}_{\boldsymbol{cs}}{}^{\mathrm{T}} & \dot{\boldsymbol{x}}^{\mathrm{T}} & \dot{\boldsymbol{x}}_{\boldsymbol{cs}}{}^{\mathrm{T}}\end{bmatrix}$ such that x_{csi} is the state representing the output of the i^{th} filter board for i = 1,..., N, where N is the total number of filter boards across all sensor nodes, or n (the number of degrees of freedom) multiplied by n_f (the number of filter boards in a single sensor node), and $\boldsymbol{y}\boldsymbol{y} \in \mathbb{R}^N$ is a vector containing the output of each filter board on each cochlea-inspired sensor node. With the addition of the cochlea-inspired sensor nodes, the system matrix becomes

$$\widetilde{\boldsymbol{A}} = \begin{bmatrix} \mathbf{0} & \mathbf{0} & \mathbf{I} & \mathbf{0} \\ \mathbf{0} & \mathbf{0} & \mathbf{0} & \mathbf{I} \\ -\mathbf{M}^{-1}\mathbf{K_s} & \mathbf{0} & -\mathbf{M}^{-1}\mathbf{C_d} & \mathbf{0} \\ \mathbf{0} & \boldsymbol{\Omega}^2 & \boldsymbol{\Psi} & \boldsymbol{\Upsilon} \end{bmatrix} \in \mathbb{R}^{2(n+a+N)\mathrm{x}2(n+a+N)} ,$$

where $\boldsymbol{\Omega}^2 \in \mathbb{R}^{N\mathrm{x}N}$ is the output stiffness matrix, $\Psi \in \mathbb{R}^{N\mathrm{x}(n+a)}$ is the input damping matrix, and $\Upsilon \in \mathbb{R}^{N\mathrm{x}N}$ is the output damping matrix. The addition of the cochlea inspired sensor nodes does not impact the previously defined input matrices, $\boldsymbol{B}$ and $\boldsymbol{E}$, and as such $\widetilde{\boldsymbol{B}}$ and $\widetilde{\boldsymbol{E}}$ are only expanded from $\boldsymbol{B}$ and $\boldsymbol{E}$ with the entries of these matrices that are associated with the states $\boldsymbol{x}_{\boldsymbol{cs}}$ and $\dot{\boldsymbol{x}}_{\boldsymbol{cs}}$ filled with zeros. The output matrix, $\widetilde{\boldsymbol{C}}$, is manipulated to make $\boldsymbol{x}_{\boldsymbol{cs}}$ the output variables and the matrices $\widetilde{\boldsymbol{D}}$ and $\widetilde{\boldsymbol{F}}$ remain zero

matrices. The appendix shows this full state space representation with the inclusion of the cochlea-inspired sensor nodes.

5.4.3. Simulation Results

To demonstrate the proposed control method, a numerical simulation is performed in MATLAB (MathWorks 2011) using the model based on the four story test structure (Equations 5.14 and 5.15). The cochlea-inspired sensor node serves as the sensor node on each of the floors. These nodes transmit information to a centralized node, serving as the motor neuron, on the two floors that contain the actuators (Floor 2 and Floor 3). Based on the connection type and strength between the transmitting node and the motor neuron, the received information is correspondingly amplified or attenuated using the optimal control gains that are established through the LQR optimization. This simulation is compared against a traditional control algorithm in which four traditional wireless sensor nodes collect data at each floor and transmit information to the centralized nodes on Floors 2 and Floor 3.

To assess the controller performance, four cost functions, adapted from Ohtori *et al*. (2004) are used to determine the controller's ability to reduce seismic responses that are typically important to design: inter-story drift and floor acceleration. Minimization of inter-story drift is important as it reduces the likelihood of damage during a seismic event, especially to nonstructural elements such as windows and partitions, while floor accelerations have a large impact on occupancy comfort during seismic events. Both of these measurements are assessed by first determining the direct ratio between the maximum amplitude of the uncontrolled and controlled states for both the traditional LQR algorithm and the bio-inspired control algorithm ($\boldsymbol{J}_{c1} \in \mathrm{R}^n$, $\boldsymbol{J}_{c3} \in \mathrm{R}^n$),

$$\boldsymbol{J}_{c1} = \frac{\max(|\boldsymbol{d}_{\text{controlled}}|)}{\max(|\boldsymbol{d}_{\text{uncontrolled}}|)} \tag{5.16}$$

where $\boldsymbol{d} \in \mathbb{R}^{n \mathrm{x} N_s}$ is the inter-story displacement matrix, n is the number of degrees-of-freedom in the structure, and N_s is the number of time steps in the input signal and

$$\boldsymbol{J}_{c3}=\frac{\max(|\boldsymbol{a}_{\text{controlled}}|)}{\max(|\boldsymbol{a}_{\text{uncontrolled}}|)} \tag{5.17}$$

where $\boldsymbol{a} \in \mathbb{R}^{n\text{x}N_s}$ is the inter-story acceleration matrix. Additionally, these two measurements are also compared as a ratio of the norm of the uncontrolled and controlled states ($\boldsymbol{J}_{c2} \in \text{R}^n$, $\boldsymbol{J}_{c4} \in \text{R}^n$). These metrics are represented through the equations

$$\boldsymbol{J}_{\text{c2}}=\frac{\|\boldsymbol{d}_{controlled}\|}{\|\boldsymbol{d}_{uncontrolled}\|} \tag{5.18}$$

and

$$\boldsymbol{J}_{\text{c4}}=\frac{\|\boldsymbol{a}_{controlled}\|}{\|\boldsymbol{a}_{uncontrolled}\|} \tag{5.19}$$

where $\|\cdot\|$ is the l_2 norm.

Based on the design of the cochlea-inspired sensor node, each filter board within each node transmits peak values to a centralized location. As such, there are several methods by which the actuating node can utilize the received information for the purposes of control. The actuating node can hold the received peak value constant until the next peak value is received or it can potentially improve the control performance by interpolating the received peak value to an assumed next peak value (equal and opposite in value to the current detected peak value) based on the characteristic frequency of the transmitting board using Equation 5.20.

$$u_i = u_{i\text{-}1} - \left(4p_i \frac{\omega_i}{2\pi}\Delta t_c\right) k_i \tag{5.20}$$

where u_i is the current control force contribution of the i^{th} filter board, p_i is the detected peak value of the i^{th} filter board, ω_i is the characteristic frequency of the i^{th} filter board, Δt_c is the rate of control for the actuation nodes, and k_i is the scaling factor associated with the i^{th} filter board. With each control step the current peak value is interpolated to a projected peak value (Figure 5-8) until the next peak is detected. When the next peak is detected, the actuating node abandons its interpolation and follows control trajectory of

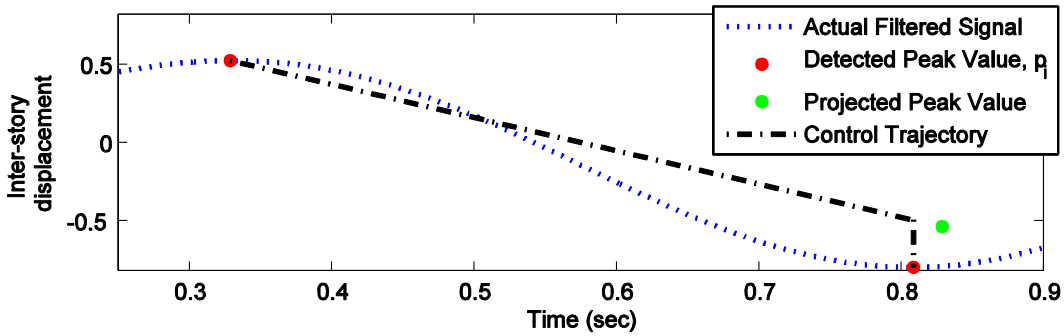

Figure 5-8. Interpolation between peak values for bio-inspired control for 1Hz filter board.

the new peak value. Additionally, the algorithm on each sensor node can be modified such that instead of transmitting only peak values, each filter board also detects and transmits zero crossings from each filtered signal. Correspondingly, at the actuating node, the control law can be developed such that it maintains a constant value in between peaks and zero crossings or it can interpolate in between this received information based on the characteristic frequency of transmitting filter board. As such, five possible scenarios arise for the bio-inspired control that can be tested in simulation to determine the optimal configuration for the cochlea-inspired sensor nodes:

- Continuous filtered signals (BC) - assumes no peak-picking algorithm (not physically feasible but will be used as a baseline);
- Peak picking (PP) - assumes that the control contribution from a filter board is held constant until the next peak value is received;
- Peak picking + interpolation (PI) - assumes that the actuating node interpolates from the current peak value to the next peak value based on the characteristic frequency of filter board;
- Peak picking + zero crossings (PZ) - assumes that the control contribution from a filter board is held constant until the next zero crossing or peak value is received;
- Peak picking + zero crossings + interpolation (PZI) - assumes that the actuating node interpolates from the current peak value (or zero crossing) to the next peak value based on the characteristic frequency of the filter board.

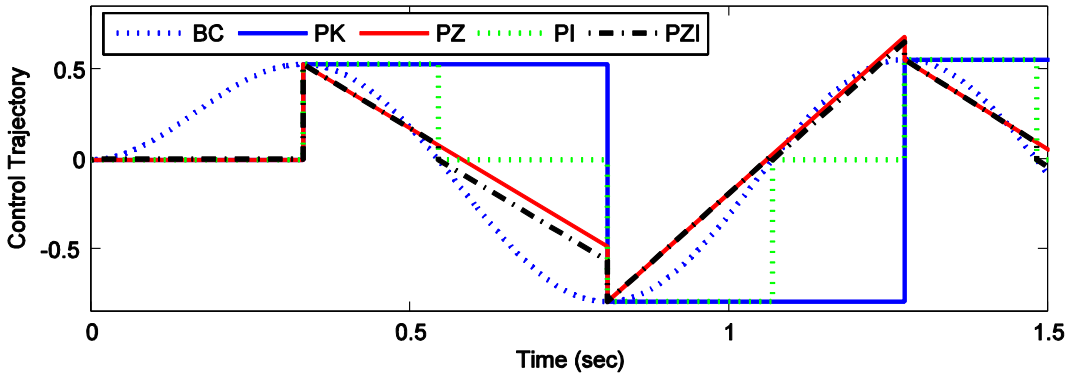

Figure 5-9. Various control options for the bio-inspired control algorithm. Note that BC is the continuous filtered case, PP is the peaking picking case, PI is the peak-picking plus interpolation case, PZ is the peak-picking plus zero-crossing case and PZI is the peak-picking plus zero-crossing plus interpolation case.

For a single neuron board from a single cochlea-inspired sensor node, these five cases can be seen in Figure 5-9. As more filter boards are added in the effects of the different boards makes the signal more convoluted and it is more difficult to interpret; the trends, however, are the same as those seen when only observing a single board.

These five bio-inspired control options were compared against the traditional output feedback LQR algorithm in MATLAB using the El Centro earthquake (±0.5g, NS direction) and the Kobe earthquake (±0.4g) as input ground motions. The four cost functions from these simulations are shown in Figure 5-10 and Figure 5-11 for the El Centro and Kobe earthquakes, respectively. Several conclusions can be made from this analysis. First, when comparing the five bio-inspired control techniques, using a continuous time signal without peak picking (Option BC) produces the best results. This is as expected as the other bio-inspired control algorithms have some error incurred through the peak picking process. This bio-inspired option, however, it unattainable without resorting back to traditional Nyquist sampling and data transmission or relying on a tethered system. In comparing the four remaining bio-inspired techniques, transmitting both peak values and zeros (PZ) results in the highest reduction of energy for all four cost functions and for both earthquakes. As such, this bio-inspired control algorithm will be used for further analyses.

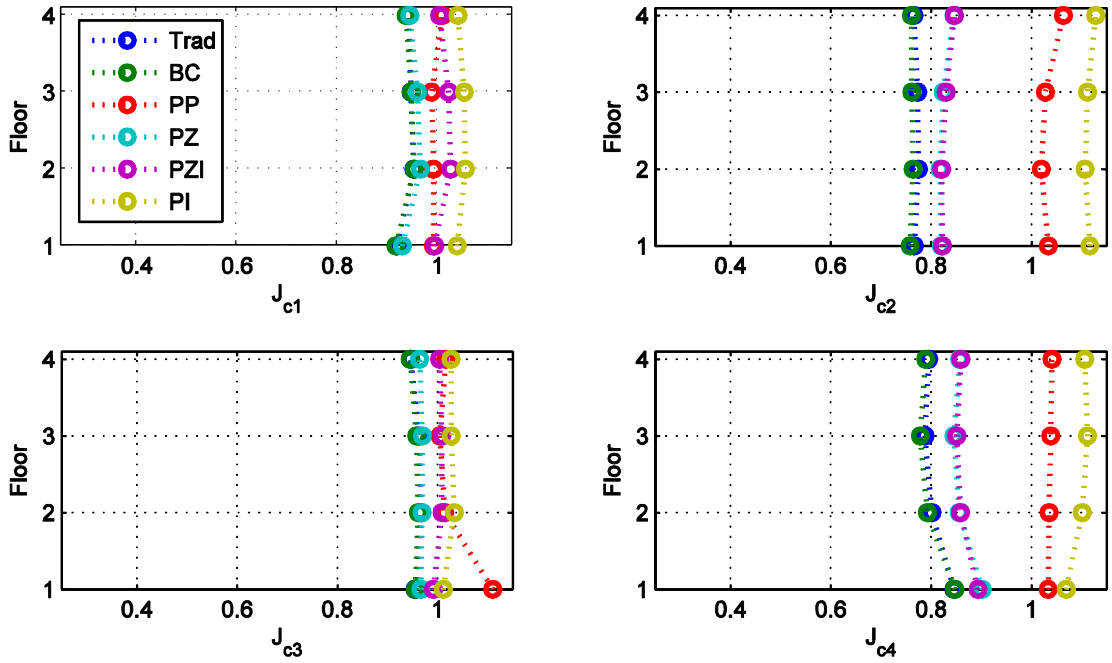

Figure 5-10. Controlled to uncontrolled ratios for the El Centro earthquake (±0.5g) simulation results when considering maximum inter-story displacement ($\boldsymbol{J}_{c1}$), norm of inter-story displacement ($\boldsymbol{J}_{c2}$), maximum acceleration ($\boldsymbol{J}_{c3}$), and norm of acceleration ($\boldsymbol{J}_{c4}$) for the traditional LQR controller and five bio-inspired control algorithms (BC, PP, PZ, PZI and PI).

From this analysis it is also observed that the traditional LQR does outperform the bio-inspired control algorithm for the majority of the cost functions. To allow for better comparisons between the two techniques, each cost function is averaged across the four floors for both the traditional LQR and the bio-inspired algorithms,

$$A_{X,j}=\left(\sum_{i=1}^{4} J_{Cj,i}\right)/4 \tag{5.21}$$

where $A_{X,j}$ is the average j^{th} cost function, J_{Cj}, for the four floors using the X control method such that X equals T is the traditional LQR algorithm and X equals B is the bio-inspired technique. The percent difference, D_j,

$$D_j = (A_{T,j} - A_{B,j})/A_{T,j} \tag{5.22}$$

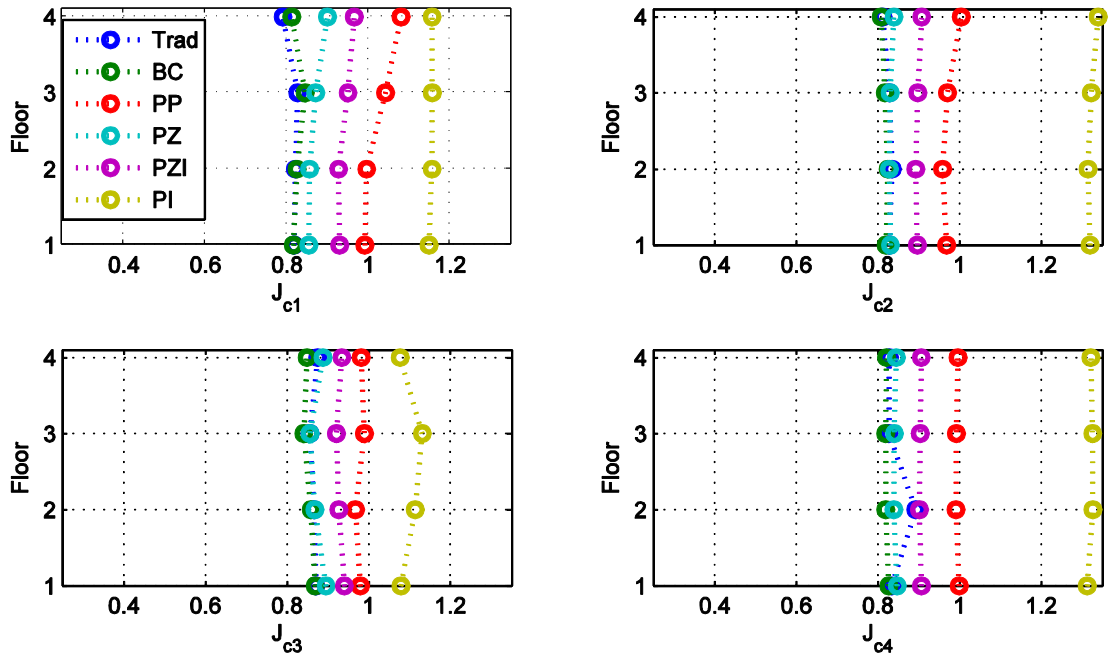

Figure 5-11. Controlled to uncontrolled ratios for the Kobe earthquake (±0.4g) simulation results when considering maximum inter-story displacement ($\boldsymbol{J}_{c1}$), norm of inter-story displacement ($\boldsymbol{J}_{c2}$), maximum acceleration ($\boldsymbol{J}_{c3}$), and norm of acceleration ($\boldsymbol{J}_{c4}$) for the traditional LQR controller and five bio-inspired control algorithms (BC, PP, PZ, PZI and PI).

demonstrates the difference in control capabilities between the two techniques for the j^{th} cost function. From this analysis it is shown that the bio-inspired control algorithm is able to achieve similar control capabilities (within 10%) as the traditional LQR algorithm for all four cost functions (Table 5-1).

For both control cases (*i.e.*, LQR or bio-inspired), however, the controller is not able to significantly reduce the inter-story displacement, with the best reduction being only approximately 20% for any of the four cost functions for either seismic excitation. If the behavior of the actuator is observed, it is clear that the actuator is saturated at its actuation capacity for the majority of the control period and therefore, is unable to adequately minimize the structure response. If the constraint on the actuator response is removed such that the controller is allowed to demand infinite control force from the actuator, then the overall control algorithm is more effective for both the LQR and bio-inspired control laws with improvements ranging from 2% to 23% (Table 5-2).

Table 5-1. Comparison of the control capabilities when using the traditional LQR algorithm and the bio-inspired control algorithm for both the El Centro and Kobe earthquakes and a constrained actuator.

	Cost Function	Traditional LQR Average Ratio, A_T	Bio-Inspired Average Ratio, A_B	% Difference, D
El Centro Earthquake	$\boldsymbol{J}_{c1}$	0.9405	0.9499	-1.00%
	$\boldsymbol{J}_{c2}$	0.7699	0.8271	-7.43%
	$\boldsymbol{J}_{c3}$	0.9578	0.9672	-0.98%
	$\boldsymbol{J}_{c4}$	0.8076	0.8650	-7.11%
Kobe Earthquake	$\boldsymbol{J}_{c1}$	0.8130	0.8690	-6.89%
	$\boldsymbol{J}_{c2}$	0.8255	0.8320	-0.79%
	$\boldsymbol{J}_{c3}$	0.8667	0.8767	-1.15%
	$\boldsymbol{J}_{c4}$	0.8428	0.8452	-0.28%

Table 5-2. Comparison of the control capabilities when using the traditional LQR algorithm and the bio-inspired control algorithm for both the El Centro and Kobe earthquakes and an unconstrained actuator.

	Cost Function	Traditional LQR Average Ratio, A_T	Bio-Inspired Average Ratio, A_B	% Difference, D
El Centro Earthquake	$\boldsymbol{J}_{c1}$	0.9023	0.9204	-2.00%
	$\boldsymbol{J}_{c2}$	0.6966	0.7229	-3.78%
	$\boldsymbol{J}_{c3}$	0.9025	0.9399	-4.14%
	$\boldsymbol{J}_{c4}$	0.7438	0.7785	-4.67%
Kobe Earthquake	$\boldsymbol{J}_{c1}$	0.7916	0.7171	+9.41%
	$\boldsymbol{J}_{c2}$	0.7288	0.6440	+11.64%
	$\boldsymbol{J}_{c3}$	0.7565	0.7444	+1.60%
	$\boldsymbol{J}_{c4}$	0.7243	0.6664	+7.99%

Additionally, when comparing the two control laws, the bio-inspired algorithm outperforms the traditional LQR algorithm when the structure is subject to the Kobe earthquake. From this analysis it can be concluded that the experimental set-up of this test bed may be a limiting factor in that the two actuators do not have enough control capability to adequately achieve the desired reduction in displacements and accelerations.

5.4.4. Energy Analysis

While a reduction in inter-story displacement is desirable, the overall energy consumption of the control system is also a concern. For the traditional LQR algorithm it is assumed that a state-of-the art wireless sensor node, the *Narada* (Swartz *et al.* 2005), is used as the sensor node. As seen in Chapter 4, the *Narada* consumes 375mW of power at 5V. If this unit collects data for the control algorithm at a rate of 50Hz then a total of 3000 data packets are transmitted across the network from each sensing unit for the 60 second El Centro earthquake signal. If each packet can be sent in 2msec, as assumed in Chapter 4, this data transmission consumes 9.0J of energy (= 4 nodes x 3000 packets x 375mW x 2msec/packet). For the bio-inspired algorithm, on the other, across all four sensing nodes, 61,096 packets of data are transmitted (including peak values and zero crossings). If each 12-board neural sensing node consumes 60.3mW of power (per Chapter 4), then the entire transmission consumes 7.37J of energy (= 61,096 packets x 60.3mW x 2msec/packet) which is only 81.9% of the total energy transmitted by traditional sensor. For the 40 second Kobe earthquake, the traditional sensing node consumes 6.0J of energy while the bio-inspired algorithm transmits 37,628 packets and therefore, consumes 4.5J of energy, or 75% of the total energy consumed by the traditional sensor.

Furthermore, some of the synaptic strength values on the individual boards within each sensor node may not have a significant contribution to the overall control algorithm and therefore could potentially be pruned from the system without significantly impacting the controllability. If these original values are considered (Figure 5-12), it is evident that there is a large range of synaptic strengths and some must have a larger role than others in the control results. Therefore, synaptic strengths in the bio-inspired control

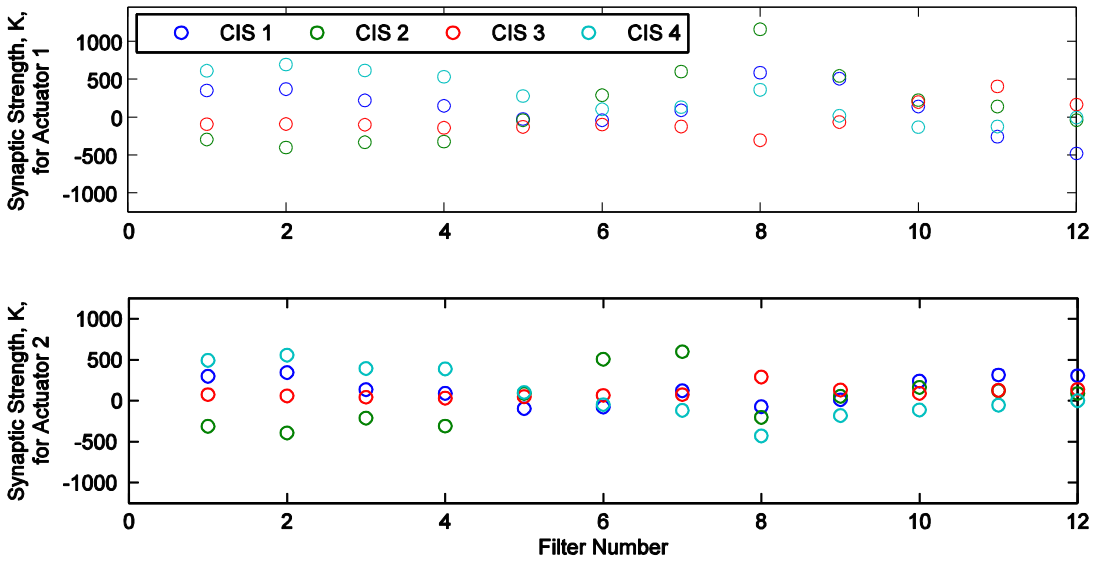

Figure 5-12. Optimal synaptic strengths between each filter board on each floor and the centralized motor neuron unit which control actuator 1 and actuator 2. Note that '*CIS X*' depicts the filter boards associated with the cochlea-inspired sensing node that is located on the floor *X*.

law are pruned from the system based on a simple threshold; if the absolute value of the synaptic strength is greater than a threshold value then it remains in the control algorithm, otherwise it is eliminated (*i.e.*, becomes zero). Because a single board communicates information to both actuators, a board is only removed from the system once the connection to both motor neurons is eliminated through this threshold technique. The pruning threshold value is incremented in gains of 50 from 0 to 650 and the impact of removing these weights is considered for both the El Centro earthquake and the Kobe earthquake (Figure 5-13, Figure 5-14). For a small amount of pruning, there is no significant change in the control capabilities of the system for either earthquake record but the overall energy consumption of the system does decrease because less data is transmitted. However, as the number of eliminated boards increases there is a threshold that has a large negative effect on the control capabilities of the system and all four cost functions increase. With more pruning, though, the cost functions again decrease to acceptable levels. While this behavior is unexpected, it is thought that the effect of certain weighting values across all the sensing boards are counterbalanced by other weighting values within the network. As such, when some of these weights are

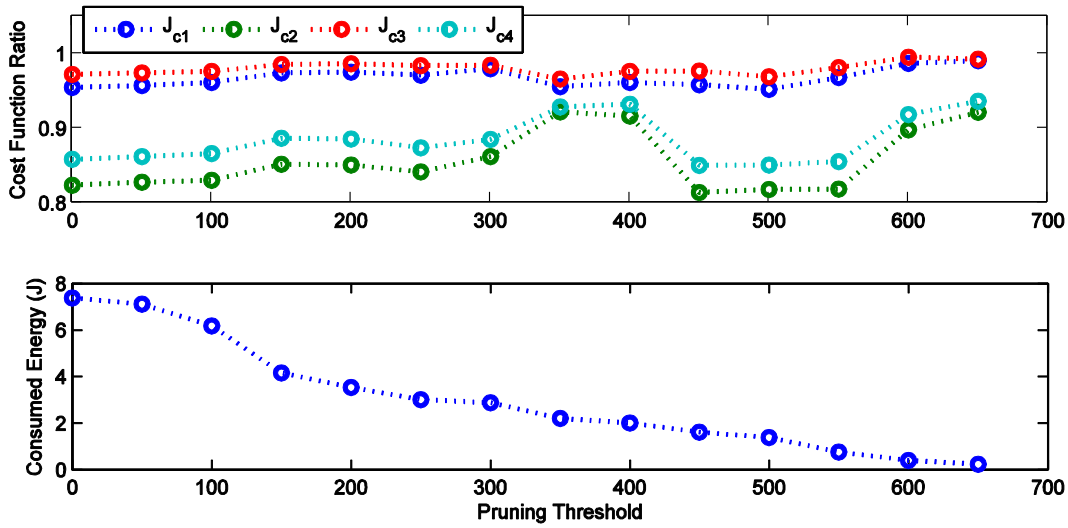

Figure 5-13. Effect of pruning synaptic connections between the cochlea-inspired sensing node and the motor neuron node for the El Centro earthquake.

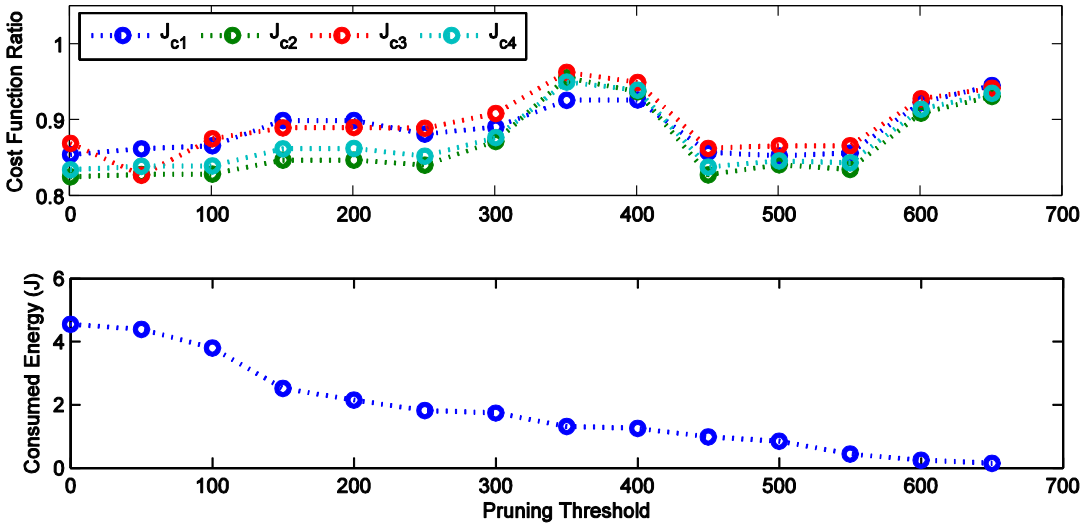

Figure 5-14. Effect of pruning synaptic connections between the cochlea-inspired sensing node and the motor neuron node for the Kobe earthquake.

eliminated, the remaining weights become unbalanced and there is a large decrease in the control capabilities. The balance is restored by further pruning of the remaining weights.

Therefore, the threshold value for the pruning analysis is set to 450, which results in the elimination of 42 boards across the four cochlea-inspired wireless sensor nodes. With this pruning the average cost functions $A_{B,1}$, $A_{B,2}$, $A_{B,3}$, and $A_{B,4}$ increased by 0.35%,

-1.2% (indicated a better performance with pruning), 0.47%, and -0.97%, respectively, for the El Centro earthquake and 0.37%, 0.34%, -0.78%, and 0.38%, respectively, for the Kobe earthquake. With this pruning the overall energy consumption of the bio-inspired control law was reduced by 78.1% for the El Centro earthquake and 78.6% for the Kobe earthquake thereby resulting in further energy improvements as compared to the traditional control law. .

Therefore, the bio-inspired control algorithm was able to adequately control both the inter-story drift and the acceleration of the test bed in simulation while working within the limits of the actuator capabilities for both the El Centro earthquake and the Kobe earthquake. These results were comparable in magnitude to the control achieved when using a traditional LQR algorithm with standard wireless sensor nodes. The bio-inspired algorithm, however, is able to consume less power throughout the entire control procedure, which is only heightened with additional pruning, thus making it a more attractive alternative than the traditional methods.

5.5. Chapter Summary

In this chapter, a bio-inspired control algorithm was proposed that derived inspiration from the mechanisms employed by biological sensory systems and the interactions between neurons and muscles. In this algorithm, the information received from sensing nodes was amplified or attenuated based on the connection type and synaptic strength between the sending neuron and the receiving neuron and this resulting value was directly applied as a control force. Because of this, the typical computational delays that are seen in wireless sensor control systems are eliminated.

The proposed bio-inspired control algorithm was validated in simulation on a four-story shear structure. The cochlea-inspired sensor node from Chapter 4 was used as the sensing node which transmitted data to receiving nodes that either amplified or attenuated the received data and then applied the corresponding control force. The bio-inspired control algorithm was able to achieve similar control capabilities as a traditional control algorithm when considering both inter-story displacements and accelerations. Additionally, the bio-inspired algorithm saw large power savings as compared to the traditional wireless sensor node and this was only compounded upon when the cochlea-

inspired sensor nodes were optimized for control of a four story shear structure by removing boards that were less significant for control.

Therefore, this chapter addressed the challenges that the control community faces when employing traditional wireless sensor nodes for the purposes of control. The bio-inspired algorithm is a streamlined real-time algorithm that is able to minimize the inter-story displacement of a structure thus addressing the typical computational inundation of wireless sensor nodes. Additionally, the cochlea-inspired sensor nodes exhibits vast power savings as compared to traditional wireless sensor nodes and therefore alleviates some of the power constraints on the system. As such, this proposed bio-inspired sensing and control algorithm is able to address many of the limitations currently found in wireless sensing and should be considered as a new paradigm for sensing and control.

CHAPTER 6

CONCLUSIONS

6.1. Summary of Results

The main focus of this dissertation is to present the design and validation of a new bio-inspired sensor node for the purposes of wireless structural monitoring and control. While traditional wireless sensor nodes are beginning to see wide-spread use and deployments in both monitoring and control applications, they are inhibited by several performance bottlenecks which include power, computation, and communication constraints. This dissertation draws upon the principles seen in biological sensory systems to overcome many of these deficiencies, thus establishing new sensing and control paradigms for the smart structure field. While previous researchers have attempted to encapsulate the functionality of biological sensory systems within signal processing algorithms (*e.g.*, artificial neural networks (ANNs)), these algorithms do not fully leverage many of the benefits of biological sensory systems. Therefore, this dissertation takes a deeper look at biological sensory systems and directly draws from their unique signal processing and data transmission processes to inspire new sensing, computing, and communication techniques for wireless sensing and control systems.

In Chapter 2, the well-established bio-inspired signal processing algorithm termed artificial neural networks was explored in an attempt to understand their benefits and limitations as they pertain to implementation in a wireless sensor environment. For this study, a particular ANN architecture was chosen, the Volterra-Weiner Neural Network (VWNN) due to its limited connectivity between the input and hidden nodes, which

therefore has potential to alleviate some communication requirements across the wireless sensor network (WSN). This ANN has also been proven to be an effective tool for model prediction which is critical for both structural monitoring and control applications. The VWNN was decentralized across a wireless sensing network, thus fusing the parallel processing capabilities of both ANNs and WSNs together. Through this study, it was found that leveraging the parallel processing attributes inherent to ANNs does lead to more efficient power consumption across the WSN. These gains in power efficiency, however, were largely offset by increased power requirements for inter-node communication which is necessary for implementation of an ANN on a WSN. Therefore, while ANNs do more efficiently utilize the computational resources of WSNs, they generally cannot overcome the power constraints imposed by power-hungry radios and by the limited radio bandwidth which is available to a WSNs.

Based on the findings from Chapter 2, Chapter 3 took a deeper look at biological sensory systems in order to use them as a source of inspiration for establishing a new sensing paradigm for wireless sensors. In this chapter, particular attention was given to the mammalian auditory system due to its unique signal processing mechanisms that are attractive for structural monitoring and control. As such, a new sensing paradigm was proposed that: 1) performed real-time spectral decomposition of a convoluted input signal, 2) implemented pick-picking of the resulting frequency components so as to achieve high data transmission efficiency, and 3) transmitted the resulting compressed form of signal information to the WSN for storage in a centralized location. This new sensing technique achieved high data compression rates that were comparable to traditional compressive techniques (*e.g.*, wavelet transforms, compressive sensing). The high data compression achieved translates into large energy savings for wireless sensor nodes. Additionally, it was shown that this algorithm could be executed in real-time which is typically unattainable by other compression algorithms.

In Chapter 4, the proposed bio-inspired sensing paradigm from Chapter 3 was built in hardware and validated on a real-world seismic monitoring application. The sensing node was comprised of multiple low-power modular building blocks each responsible for implementing a portion of the new sensing paradigm. Each circuit unit filtered a convoluted sensor signal using a unique characteristic frequency, implemented

a real-time peak-picking algorithm (thus compressing the data), and transmitted its data wirelessly to the centralized WSN. Each of these building block units by itself was only capable of implementing a small portion of the entire bio-inspired sensing framework; however, by combining multiple units together, the complete sensing paradigm was achieved. This new sensor was used to monitor the response of a single degree-of-freedom (SDOF) structure at the Korea Construction Engineering Development (KOCED) Multi-Platform Seismic Simulation Center at Pusan University, Pusan, Korea and during these tests the sensor node parameters (*i.e.*, number of filter boards, filter bandwidth, filter spacing) were varied for optimization of the device design. From these tests, typically large data compression was achieved (ranging from 8% to 80% less transmitted data) with minimal reconstruction error when monitoring both pure seismic signals as well as the seismic response of the SDOF structure. The sensor node was also compared to traditional wireless sensor nodes and it was found that the new sensor node consumed significantly less energy (67% to 93%) than its state-of-the-art counterparts (*i.e., iMote2, Narada*). Additionally, it was found that because there is some overlap between sensor units on the bio-inspired sensor node and due to the manner of deconstruction of the original signal, lost data is not as significant of a concern for the sensor node. Therefore, the new bio-inspired sensor node is able to address the typical power issues associated with wireless sensor nodes while maintaining an accurate representation of the original signal.

In Chapter 5, a new bio-inspired control algorithm was proposed based on the interactions seen in biological systems, specifically sensory neurons, motor neurons, and muscles. Information flow between these three components is either amplified or attenuated based on the connection type (*i.e.*, excitatory or inhibitory) and the magnitude of this amplification or attenuation is based on the synaptic strength. As such, a bio-inspired control algorithm is proposed for wireless sensing and control that applies a variable gain to signal information as it flows from the sensors to the actuators. The proposed bio-inspired algorithm is validated in simulation on a four-story shear structure. In the control algorithm, four cochlea-inspired sensor nodes transmitted the inter-story displacement from each of the floors to a centralized processing node, which served as the motor neuron. This node then directly commanded the actuators through a control

force that was derived through amplification or attenuation of the received data from the sensing nodes in the WSN. Based on the results, the bio-inspired control algorithm was able to reduce the inter-story displacement of the structure through real-time processing techniques. Again, the cochlea-inspired sensor node exhibited extreme energy savings as compared to a traditional wireless sensor node.

Therefore, in this thesis a new sensing paradigm was proposed that derived inspiration from the biological sensory system. This new sensing paradigm was able to achieve high data compression while taking advantage of parallel processing for real-time execution. The new bio-inspired sensor node was built in hardware and validated in both a monitoring application and a control application. Through these applications, the new sensor node proved that it effectively addressed many of the limitations and bottlenecks that are inherent to traditional wireless sensor nodes for the purposes of monitoring and control of civil infrastructure.

6.2. Contributions

While the structural health monitoring and control communities have been making significant advancements in recent years, the field is still challenged by several bottlenecks which prohibit easy and affordable deployments on real-world structures. Wireless sensor technology was one avenue by which to address these issues but this too came with its own set of technical challenges that further stymied the advancement of the field. The main contribution of this dissertation is the illustration of a novel sensing paradigm that addresses the traditional limitations of current monitoring and control systems, with a particular emphasis on the challenges faced by the wireless community. Some of these challenges include tendency toward computation inundation, large power consumption during processing at the node or communication, and limited radio bandwidth thus opening a WSN to the risk of lost data during wireless transmissions.

This dissertation sought a solution to these challenges found in wireless sensors through a novel sensing paradigm that drew inspiration from the mechanisms employed by biological sensory systems. Biological sensory systems are exceptionally robust and adaptive systems whose parallel processing capabilities and rapid response times exceed

similarly functioning engineering systems. An exceptionally important contribution that this thesis made was the creation of a low-power wireless sensor node that embodied the functional principles of the mammalian cochlea to compress sensor data for lower power operation. The new sensor node leverages the capabilities of multiple low-power, crude processing neuron units that rapidly transmit vast amounts of information. While each of these pieces of information has some significance, due to the large amount of transmitted data, losing a single bit of data does not have a large impact on the reconstruction capability of WSN. In this way, the sensing node overcomes the constraints of limited radio bandwidth by eliminating reliance on packing long time history records into a single packet of data that can be lost. Additionally, through the use of multiple crude processing units, the sensing node leverages the parallel processing capabilities of biological systems, thus reducing computation inundation. Therefore, the proposed wireless sensor node addresses many of the current bottlenecks seen in the wireless sensing community for civil infrastructure and is attractive for real-world deployments.

As demonstrated in this dissertation, this new sensing paradigm has potential to revolutionize the structural monitoring and control communities by pairing the already recognized benefits of wireless sensor nodes (*i.e.*, low-cost, easy to install) with the benefits of biological systems (*i.e.*, real-time operation through parallel processing, exceptional system resiliency through large redundancy). The application of this sensor node to several experimental test beds highlights the robustness of the sensor node outside of a controlled laboratory environment. Additionally, while the applications in this dissertation were limited to civil infrastructure, the implications of this new sensing paradigm extend well beyond structural monitoring and control. The techniques by which the sensing node decomposes signals into frequency components is attractive for a variety of different engineering disciplines and their associated problems.

6.3. Future Work

6.3.1. Short-Term Future Research

In the near future, the proposed bio-inspired sensing node should be validated on a full scale test structure exposed to seismic ground motion and controlled using common

actuations (*e.g.*, MR dampers). This will further demonstrate the real-time control capabilities but in a harsher environment than that afforded by the controlled laboratory experiments presented in this thesis. The applicability of the proposed sensor node will be verified for both structural monitoring and control applications during such tests.

While the cochlea-inspired sensor node has proved to be successful, these studies have also highlighted several areas for improvement upon which future research should be focused. First, while the sensor node does achieve greater power savings than the state-of-the art wireless sensor node used for comparison in this thesis, the digital radio consumes over 80% of the entire sensor node's energy. As such, future work should seek more energy efficient alternatives that deviate from traditional packetized approaches. In particular, the future radio should seek to modulate information in binary spike trains, as seen with biological systems, thus eliminating unnecessary overhead that is incurred through the use of a packetized radio. Second, the hardware architecture of the sensor node should be reformatted such that the filter boards within each sensor node are able to autonomously adapt according to the constraints of the application. The current hardware design uses discrete circuit components (*e.g.*, resistors and capacitors) to characterize each filter board and any changes to this characterization requires the components to be manually changed. By allowing this process to become digitally autonomous, the sensor node will be able to "learn" its own characteristics based on input signals, similar to the processes seen in biological systems.

6.3.2. Long-Term Research Objectives

While the cochlea-inspired sensor node provides a strong foundation for bio-inspired sensing and control, there is still significant inspiration that can be drawn from biology for the advancement of structural monitoring and control. First, biological sensory systems are extremely adept at sensor fusion (*i.e.*, integrating information from various types of sensors). While this has been implemented before within monitoring and control systems, it often requires setting a fusion strategy at the outset of systems implementation that cannot autonomously adapt to the collected signals. Therefore, one area of future work should focus on considering the mechanisms by which biological systems integrate information from various sources and mimicking these methods into

the current methods of data collection for structural monitoring systems. Second, biological systems are able to rapidly react to information through pattern recognition within spike trains and therefore, do not need to complete a full decoding process, thus resulting in valuable time savings across the system. Future work on bio-inspired sensing and control should focus on delving further into feature extraction using pattern recognition directly from spike trains so as to fully leverage the real-time capabilities of biological systems. In this way, by achieving sensor fusion and leveraging real-time feature extraction, a bio-inspired network of sensor nodes could be established that is capable of real-time processing while also possessing the ability to adapt and react to input stimulus. In this way, the human impact factor on the system would be removed and overall, the monitoring or control system would be more robust.

APPENDIX

The dynamic equation of motion for a four degree-of-freedom structure subject to the external forces of cart motion can be represented as

$$\boldsymbol{M}\ddot{\boldsymbol{x}}(t) + \boldsymbol{C_d}\dot{\boldsymbol{x}}(t) + \boldsymbol{K_s}\boldsymbol{x}(t) = -\boldsymbol{M\iota}\ddot{x}_g(t) + \boldsymbol{F_c}\boldsymbol{u}(t) \tag{A.1}$$

where

$$\boldsymbol{x} = [x_1 \quad x_2 \quad x_3 \quad x_4 \quad x_{c1} \quad x_{c2}]^{\mathrm{T}},$$

$$\boldsymbol{u} = [u_1 \quad u_2]^{\mathrm{T}},$$

$$\boldsymbol{M} = \begin{bmatrix} m_1 & 0 & 0 & 0 & 0 & 0 \\ 0 & m_2+m_{c1} & 0 & 0 & m_{c1} & 0 \\ 0 & 0 & m_3 & 0 & 0 & 0 \\ 0 & 0 & 0 & m_4+m_{c2} & 0 & m_{c2} \\ 0 & m_{c1} & 0 & 0 & m_{c1} + \frac{J_m {K_g}^2}{{r_{mp}}^2} & 0 \\ 0 & 0 & 0 & m_{c2} & 0 & m_{c2} + \frac{J_m {K_g}^2}{{r_{mp}}^2} \end{bmatrix},$$

$$\boldsymbol{C_d} = \begin{bmatrix} c_1 + c_2 & -c_2 & 0 & 0 & 0 & 0 \\ -c_2 & c_2 + c_3 & -c_3 & 0 & 0 & 0 \\ 0 & -c_3 & c_3 + c_4 & -c_4 & 0 & 0 \\ 0 & 0 & -c_4 & c_4 & 0 & 0 \\ 0 & 0 & 0 & 0 & B_{eq} + \frac{\eta_g \eta_m K_t K_m {K_g}^2}{R_m {r_{mp}}^2} & 0 \\ 0 & 0 & 0 & 0 & 0 & B_{eq} + \frac{\eta_g \eta_m K_t K_m {K_g}^2}{R_m {r_{mp}}^2} \end{bmatrix},$$

$$\boldsymbol{K_s} = \begin{bmatrix} k_1 + k_2 & -k_2 & 0 & 0 & 0 & 0 \\ -k_2 & k_2 + k_3 & -k_3 & 0 & 0 & 0 \\ 0 & -k_3 & k_3 + k_4 & -k_4 & 0 & 0 \\ 0 & 0 & -k_4 & k_4 & 0 & 0 \\ 0 & 0 & 0 & 0 & 0 & 0 \\ 0 & 0 & 0 & 0 & 0 & 0 \end{bmatrix},$$

$$\boldsymbol{\iota} = [1 \quad 1 \quad 1 \quad 1 \quad 0 \quad 0]^{\mathrm{T}},$$

$$\boldsymbol{F_c} = \begin{bmatrix} 0 & 0 \\ 0 & 0 \\ 0 & 0 \\ 0 & 0 \\ \frac{\eta_g \eta_m K_t K_g}{R_m r_{mp}} & 0 \\ 0 & \frac{\eta_g \eta_m K_t K_g}{R_m r_{mp}} \end{bmatrix},$$

x_i is the displacement of i^{th} degree of freedom (i = 1, ..., 4),
x_{ci} is the displacement of i^{th} cart (i = 1, 2),
u_i is the motor voltage of the i^{th} cart (i = 1, 2),
x_g is the ground motion,
m_i is the mass of i^{th} degree of freedom (i = 1, ..., 4),
c_i is the damping of i^{th} degree of freedom (i = 1, ..., 4),
k_i is the stiffness of i^{th} degree of freedom (i = 1, ..., 4),
I is the identity matrix,
m_{ci} is the mass of i^{th} actuator cart (i = 1, 2),
B_{eq} is the equivalent vicious damping coefficient in the motor pinion,
J_m is the rotor moment of inertia,
K_g is the planetary box gear ratio,
K_t is the motor torque constant,
K_m is the Back-Electromotive-Force (EMF) constant,
r_{mp} is the motor pinion radius,
R_m is the motor armature resistance,
η_g is the planetary gearbox efficiency, and
η_m is the motor efficiency.

This can be represented in state space and expanded to include the dynamics of the cochlea-inspired sensor nodes as

$$\dot{\boldsymbol{z}}\boldsymbol{z}(t) = \widetilde{\boldsymbol{A}}\boldsymbol{z}\boldsymbol{z}(t) + \widetilde{\boldsymbol{B}}\boldsymbol{u}(t) + \widetilde{\boldsymbol{E}}\ddot{\boldsymbol{x}}_{\boldsymbol{g}}(t) \tag{A.2}$$

$$\boldsymbol{y}\boldsymbol{y}(t) = \widetilde{\boldsymbol{C}}\boldsymbol{z}\boldsymbol{z}(t) + \widetilde{\boldsymbol{D}}\boldsymbol{u}(t) + \widetilde{\boldsymbol{F}}\ddot{x}_g(t) \tag{A.3}$$

where $\dot{\boldsymbol{z}}\boldsymbol{z}^{\mathrm{T}} = \begin{bmatrix}\boldsymbol{x}^{\mathrm{T}} & \boldsymbol{x_{cs}}^{\mathrm{T}} & \dot{\boldsymbol{x}}^{\mathrm{T}} & \dot{\boldsymbol{x}}_{\boldsymbol{cs}}{}^{\mathrm{T}}\end{bmatrix}$ such that the vector $\boldsymbol{x}$ includes the states representing the displacement of each degree-of-freedom as well as the displacement of each cart and x_{csi} is the state representing the output of the i^{th} filter board for $i = 1, \ldots, N$, where N is the total number of filter boards for all sensor node and equals n (the number of degrees of freedom and in this case equal to 4) multiplied by n_f (the number of filter boards per cochlea-inspired sensor node). The output states, $\boldsymbol{yy}$, are the outputs from each filter board on each cochlea-inspired sensor node. The system matrix is

$$\widetilde{\boldsymbol{A}} = \begin{bmatrix} \mathbf{0} & \mathbf{0} & \mathbf{I} & \mathbf{0} \\ \mathbf{0} & \mathbf{0} & \mathbf{0} & \mathbf{I} \\ -\mathbf{M}^{-1}\mathbf{K_s} & \mathbf{0} & -\mathbf{M}^{-1}\mathbf{C_d} & \mathbf{0} \\ \mathbf{0} & \boldsymbol{\Omega}^2 & \boldsymbol{\Psi} & \boldsymbol{\Upsilon} \end{bmatrix} \in \mathbb{R}^{2(6+4n_f)\mathrm{x}2(6+4n_f)} ,$$

where $\boldsymbol{M}$, $\boldsymbol{K_s}$, $\boldsymbol{C_d}$ remain unchanged from their previous definition,

$$\boldsymbol{\Omega^2} = \begin{bmatrix} {\omega_{1,1}}^2 & 0 & 0 & 0 & 0 & 0 \\ 0 & \ddots & 0 & 0 & 0 & 0 \\ 0 & 0 & {\omega_{1,n_f}}^2 & 0 & 0 & 0 \\ 0 & 0 & 0 & {\omega_{2,n_f}}^2 & 0 & 0 \\ 0 & 0 & 0 & 0 & \ddots & 0 \\ 0 & 0 & 0 & 0 & 0 & {\omega_{4,n_f}}^2 \end{bmatrix} \in \mathbb{R}^{4n_f \mathrm{x} 4n_f} ,$$

$\omega_{i,j}$ is the natural frequency of the j^{th} filter board within the cochlea-inspired sensor node at the i^{th} degree of freedom,

$\xi_{i,j}$ is the damping ratio of the j^{th} filter board within the cochlea-inspired sensor node at the i^{th} degree of freedom,

$$\boldsymbol{\Psi} = \begin{bmatrix} 2\xi_{1,1}\omega_{1,1} & 0 & 0 & 0 & 0 & 0 \\ \vdots & \vdots & \vdots & \vdots & \vdots & \vdots \\ 2\xi_{1,n_f}\omega_{1,n_f} & 0 & 0 & 0 & 0 & 0 \\ -2\xi_{1,1}\omega_{1,1} & 2\xi_{2,1}\omega_{2,1} & 0 & 0 & 0 & 0 \\ \vdots & \vdots & \vdots & \vdots & \vdots & \vdots \\ -2\xi_{1,n_f}\omega_{1,n_f} & 2\xi_{2,n_f}\omega_{2,n_f} & 0 & 0 & 0 & 0 \\ 0 & -2\xi_{2,1}\omega_{2,1} & 2\xi_{3,1}\omega_{3,1} & 0 & 0 & 0 \\ \vdots & \vdots & \vdots & \vdots & \vdots & \vdots \\ 0 & -2\xi_{2,n_f}\omega_{2,n_f} & 2\xi_{3,n_f}\omega_{3,n_f} & 0 & 0 & 0 \\ 0 & 0 & -2\xi_{3,1}\omega_{3,1} & 2\xi_{4,1}\omega_{4,1} & 0 & 0 \\ \vdots & \vdots & \vdots & \vdots & \vdots & \vdots \\ 0 & 0 & -2\xi_{3,n_f}\omega_{3,n_f} & 2\xi_{4,n_f}\omega_{4,n_f} & 0 & 0 \end{bmatrix} \in \mathbb{R}^{4n_f \text{x} 6},$$

and

$$\boldsymbol{\Upsilon} = \begin{bmatrix} 2\xi_{1,1}\omega_{1,1} & 0 & 0 & 0 & 0 & 0 \\ 0 & \ddots & 0 & 0 & 0 & 0 \\ 0 & 0 & 2\xi_{1,n_f}\omega_{1,n_f} & 0 & 0 & 0 \\ 0 & 0 & 0 & 2\xi_{2,1}\omega_{2,1} & 0 & 0 \\ 0 & 0 & 0 & 0 & \ddots & 0 \\ 0 & 0 & 0 & 0 & 0 & 2\xi_{4,n_f}\omega_{4,n_f} \end{bmatrix} \in \mathbb{R}^{4n_f \text{x} 4n_f}.$$

The input matrices, $\widetilde{\boldsymbol{B}}$ and $\widetilde{\boldsymbol{E}}$ become

$$\widetilde{\boldsymbol{B}} = \begin{bmatrix} \mathbf{0} & \mathbf{0} & \mathbf{M}^{-1}\mathbf{F_c} & \mathbf{0} \end{bmatrix}^{\mathrm{T}} \in \mathbb{R}^{2(4n_f+6)\text{x}2}$$

and

$$\widetilde{\boldsymbol{E}} = \begin{bmatrix} \mathbf{0} & \mathbf{0} & \text{-}\boldsymbol{\iota} & \mathbf{0} \end{bmatrix}^{\mathrm{T}} \in \mathbb{R}^{2(4n_f+6)}.$$

The output matrix, $\widetilde{\boldsymbol{C}}$, becomes

$$\widetilde{\boldsymbol{C}} = \begin{bmatrix} \mathbf{0}_{4n_f x 6} & \mathbf{I}_{4n_f x 4n_f} & \mathbf{0}_{4n_f x 6} & \mathbf{0}_{4n_f x 4n_f} \end{bmatrix} \in \mathbb{R}^{4n_f \text{x} 2(4n_f+6)}$$

while $\widetilde{\boldsymbol{D}} \in \mathbb{R}^{4n_f \text{x} 2}$ and $\widetilde{\boldsymbol{F}} \in \mathbb{R}^{4n_f}$ are both zero matrices.

REFERENCES

Ananthanarayanan, R., Esser, S. K., Simon, H. D., and Modha, D. S. "The cat is out of the bag: cortical simulations with 109 neurons, 1013 synapses." *Proc., Conference on High Performance Computing Networking, Storage and Analysis*, IEEE, Portland, OR.

ASCE (2013). "2013 report card for America's infrastructure." American Society of Civil Engineers, Washington D.C.

Averbeck, B. B., Latham, P. E., and Pouget, A. (2006). "Neural correlations, population coding and computation." *Nature*, 7, 358-366.

Avissar, M., Furman, A. C., Saunders, J. C., and Parsons, T. D. (2007). "Adaption reduces spike-count reliability, but not spike-timing precisions, of auditory nerves response." *Journal of Neuroscience*, 27(24), 6461-6472.

Ayers, J., and Witting, J. (2007). "Biomimetic approaches to the control of underwater walking machines." *Philosophical Transactions of the Royal Society of London, Series A: Mathematical, Physical and Engineering Sciences*, 365(1850), 273-295.

Bao, Y., Beck, J. L., and Li, H. (2011). "Compressive sampling for accelerometer signals in structural health monitoring." *International Journal of Structural Health Monitoring*, 10(3), 235-246.

Bialek, W., Rieke, F., de Ruyter Van Steveninck, R. R., and Warland, D. (1991). "Reading a neural code." *Science*, 252(5014), 1854-1857.

Bishop, C. M. (2006). *Pattern recognition and machine learning*, Springer, New York, NY.

Black, P. E. (2005). "Greedy algorithm." *Dictionary of algorithms and data structures*, < http://www.nist.gov/dads/HTML/greedyalgo.html>. (April 22, 2013).

Brownjohn, J. M. W. (2007). "Structural health monitoring of civil infrastructure." *Philosophical Transactions of the Royal Society of London, Series A: Mathematical, Physical, and Engineering Sciences*, 365(1851), 589-622.

Candès, E. J., Romberg, J., and Tao, T. (2006). "Robust uncertainty principles: exact signal reconstruction from highly incomplete frequency information." *IEEE Transactions on Information Theory*, 52(2), 489-509.

Candès, E. J., and Tao, T. (2005). "Decoding by linear programming." *IEEE Transactions on Information Theory*, 51(12), 4203-4215.

Candès, E. J., and Wakin, M. B. (2008). "An introduction to compressive sampling." *IEEE Signal Processing Magazine*, 25(2), 21-30.

Carter, B. (2000). "A single-supply op-amp circuit collection." Report No. SLOA058, Texas Instruments, Dallas, TX.

Celebi, M. (2002). "Seismic instrumentation of buildings (with emphasis on federal buildings)." Report No. 0-7460-68170, United States Geological Survey (USGS), Menlo Park, CA.

Chang-Siu, E., Libby, T., Tomizuka, M., and Full, R. J. (2011). "A lizard-inspired active tail enables rapid maneuvers and dynamic stabilization in terrestrial robot." *Proc., 2011 IEEE/RSJ International Conference on Intelligent Robots and Systems*, IEEE, San Francisco, CA, 1887-1894.

Chang, P. C., Flatau, A., and Liu, S. C. (2003). "Review paper: health monitoring of civil infrastructure." *International Journal of Structural Health Monitoring*, 2(3), 257-267.

Chintalapudi, K., Paek, J., Gnawali, O., Fu, T. S., Dantu, K., Caffrey, J., Govindan, R., Johnson, E., and Masri, S. (2006). "Structural damage detection and localization using NetSHM." *Proc., 5th International Conference on Information Processing in Sensor Networks*, Nashville, TN, 475-482.

Chopra, A. K. (2000). *Dynamics of Structures: Theory and Applications to Earthquake Engineering*, Prentice Hall, Upper Saddle River, NJ.

Chu, S. Y., Soong, T. T., and Reinhorn, A. M. (2005). *Active, hybrid, and semi-active structural control: a design and implementation handbook*, Wiley, New York, NY.

Constantinou, M. C., Soong, T. T., and Dargush, G. F. (1998). "Passive energy dissipation systems for structural design and retrofit." Report No. MCEER-98-MN01, Multidisciplinary Center for Earthquake Engineering Research, Buffalo, NY.

Cope, T. C., and Pinter, M. J. (1995). "The size principle: still working after all these years." *Physiology*, 10(6), 280-286.

Cybenko, G. (1989). "Approximation by superpositions of a sigmoidal function." *Mathematics of Control, Signals, and Systems*, 2, 303-314.

Dallos, P. (1992). "The active cochlea." *The Journal of Neuroscience*, 12(12), 4575-4585.

Dallos, P. (1996). "Overview: cochlear neurobiology." *The cochlea (Springer handbook of auditory research)*, P. Dallos, A. N. Popper, and R. R. Fay, eds., Springer-Verlag, New York, NY, 1-43.

Daubechies, I. (1988). "Orthonormal bases of compactly supported wavelets." *Communications on Pure and Applied Mathematics*, XLI, 909-996.

Daubechies, I. (1992). *Ten Lectures on Wavelets*, Society for Industrial and Applied Mathematics, Philadelphia, PA.

Dayan, P., and Abbott, L. F. (2005). *Theoretical neuroscience: computational and mathematical modeling of neural systems*, The MIT Press, Cambridge, MA.

De Boer, E. (1996). "Mechanics of the cochlea: modeling efforts." *The cochlea (Springer handbook of auditory research)*, P. Dallos, A. N. Popper, and R. R. Fay, eds., Springer-Verlag, New York, NY, 258-317.

Doebling, S. W., Farrar, C. R., and Prime, M. R. (1998). "A summary review of vibration-based damage identification methods." *Shock and Vibration Digest*, 30(2), 91-105.

Donoho, D. L. (2006). "Compressed sensing." *IEEE Transactions on Information Theory*, 52(4), 1289-1306.

Duda, R. O., Hart, P. E., and Stork, D. G. (2001). *Pattern classification*, John Wiley and Sons, New York, NY.

Dyke, S., Caicedo, J. M., Turan, G., Bergman, L., and Hague, S. (2003). "Phase I benchmark control problem for seismic response of cable-stayed bridges." *Journal of Structural Engineering*, 129(7), 857-872.

Dyke, S., Spencer, B. F., Quast, P., and Sain, M. K. (1995). "Role of control-structure interaction in protective system design." *ASCE Journal of Engineering Mechanics*, 121(2), 322-338.

Elliott, S. J., and Shera, C. A. (2012). "The cochlea as a smart structure." *Smart Materials and Structures*, 21(064001).

Emadi, G., Richter, C. P., and Dallos, P. (2004). "Stiffness of the gerbil basilar membrane: radial and longitudinal variations." *Journal of Neurophysiology*, 91(1), 474-488.

Farrar, C. R., and Worden, K. (2007). "An introduction to structural health monitoring." *Philosophical Transactions of the Royal Society of London, Series A: Mathematical, Physical and Engineering Sciences*, 365(1851), 303-315.

Farrar, C. R., and Worden, K. (2012). *Structural health monitoring: a machine learning perspective*, John Wiley and Sons, West Sussex, UK.

Feltrin, G., Meyer, J., Bischoff, R., and Motavalli, M. (2010). "Long-term monitoring of cable stays with a wireless sensor network." *Structure and Infrastructure Engineering: Maintenance, Management, Life-Cycle Design and Performance*, 6(5), 535-548.

Fettiplace, R., and Hackney, C. M. (2006). "The sensory and motor roles of auditory hair cells." *Nature Reviews: Neuroscience*, 7(1), 19-29.

FHWA (2011). "Bridge preservation: maintaining a state of good repair using cost effective investment strategies." Report No. FHWA-HIF-11042, Federal Highway Administration, U.S. Department of Transportation, Washington D.C.

Flock, A., and Cheung, H. C. (1977). "Actin filaments in sensory hairs of inner ear receptor cells." *Journal of Cell Biology*, 72(2), 339-343.

Fujino, Y., Murata, M., Okano, S., and Takeguchi, M. (2000). "Monitoring system of the Akashi Kaikyo bridge and displacement measurements using GPS." *Proc., SPIE 3995: Nondestructive evaluations of highways, utilities, and pipelines*, Newport Beach, CA.

Georgopoulos, A. P., Schwartz, A. B., and Kettner, R. E. (1986). "Neuronal population coding of movement direction." *Science*, 233(4771), 1416-1419.

Gray, J. M., Hill, J. J., and Bargmann, C. I. (2004). "A circuit for navigation in Caenorhabditis elegans." *Proceedings of the National Academy of Science*, 102(9), 3184-3191.

Grossberg, S. (1987). "Competitive learning: from interactive activation to adaptive resonance." *Cognitive Science*, 11(1), 23-63.

Harries, K. A. (2009). "Structural testing of prestressed concrete girders from the Lake View Drive bridge." *Journal of Bridge Engineering*, 14(2), 78-92.

Hassibi, B., and Stork, D. G. "Second order derivatives for network pruning: optimal brain surgeon." *Proc., Neural informaion processing systems: advances in neural information processing systems*, Denver, CO, 164-171.

Haykins, S. (1994). *Neural networks: a comprehensive foundation*, Prentice Hall, Upper Saddle River, NJ.

Hecht-Nielsen, R. (1989). "Theory of the backpropagation neural network." *Proc., International Joint Conference on Neural Networks (IJCNN)*, Washington D.C., 593-605.

Herz, A. V. M., Gollisch, T., Machens, C. K., and Jaeger, D. (2006). "Modeling single-neuron dynamics and computations: a balance of detail and abstraction." *Science*, 314(5796), 80-85.

Hornik, K., Stinchcombe, M., and White, H. (1989). "Multilayer feedforward networks are universal approximators." *Neural networks*, 2(5), 359-366.

Housner, G. W., Bergman, L. A., Caughey, T. K., Chassiakos, A. G., Claus, R. O., Masri, S. F., Skelton, R. E., Soong, T. T., Spencer, B. F., and Yao, J. T. P. (1997). "Structural control: past, present, and future." *Journal of Engineering Mechanics*, 123(9), 897-971.

Hudspeth, A. J. (1989). "How the ear's works work." *Nature*, 341(5), 397-404.

Jain, A. K., and Mao, J. (1996). "Artificial neural networks: a tutorial." *Computer*, 29(3), 31-44.

Jang, S. A., Jo, H., Cho, S., Mechitov, K. A., Rice, J. A., Sim, S. H., Jung, H.-J., Yun, C. B., Spencer, B. F., and Agha, G. (2010). "Structural health monitoring of a cable-stayed bridge using smart sensor technology: deployment and evaluation." *Smart Structures and Systems*, 6(5-6), 439-459.

Jenkins, C. (2012). *Bio-inspired engineering*, Momentum Press, New York, NY.

Ji, B., and Gao, H. (2004). "Mechanical properties of nanostructure of biological materials." *Journal of Mechanics and Physics of Solids*, 52(p), 1963-1990.

Kalman, R. E. (1960). "Contributions to the theory of optimal control." *Reprinted from Boletin de la Sociedad Matematica Mexicana*, 5, 102-119.

Kandel, E. R. (2000). "Nerve Cells and Behavior." *Principles of Neural Science*, E. R. Kandel, J. H. Schwartz, and T. M. Jessell, eds., McGraw-Hill, New York, NY, 19-35.

Kandel, E. R., Schwartz, J. H., and Jessell, T. M. (2000). *Principles of Neural Science*, McGraw Hill, New York, NY.

Kane, M. B. (2013). "Martlet: wireless decision maker." <http://www-personal.umich.edu/~jerlynch/Martlet_Datasheet.pdf>.

Kapoor, C. C., Graves-Abe, T. L., and Pei, J.-S. "Development of an off-the-shelf field programmable gate array-based wireless sensing unit for structural health monitoring." *Proc., SPIE 5765: Sensors and smart structures technologies for civil, mechanical, and aerospace systems*, San Diego, CA, 195-204.

Kennedy, J. (2010). "Particle swarm optimization." *Encyclopedia of machine learning*, C. Sammut, and G. I. Webb, eds., Springer, New York, NY, 760-766.

Kim, J., and Lynch, J. P. (2012). "Autonomous decentralized system identification by Markov parameter estimation using distributed smart wireless sensor networks." *Journal of Engineering Mechanics*, 138(5), 478-490.

Kim, J., Swartz, A., Lynch, J. P., Lee, J.-J., and Lee, C.-G. (2010). "Rapid-to-deploy reconfigurable wireless structural monitoring systems using extended-range wireless sensors." *Smart Structures and Systems*, 6(5-6), 505-524.

Kim, S., Pakzad, S., Culler, D., Demmel, J., Fenves, G., Glaser, S., and Turon, M. "Health monitoring of civil infrastructures using wireless sensor networks." *Proc., 6th International Conference on Information Processing in Sensor Networks*, ACM, Cambridge, MA.

Ko, J. M., and Ni, Y. Q. (2005). "Technology developments in structural health monitoring of large-scale bridges." *Engineering Structures*, 27(12), 1715-1725.

Kosmatopoulos, E. B. (1998). "Control of unknown nonlinear systems using output feedback." *Proc., 37th IEEE Conference on Decision and Control,* IEEE, Tampa, Florida, 1464-1469.

Kosmatopoulos, E. B., Smyth, A. W., Masri, S. F., and Chassiakos, A. G. (2001). "Robust adaptive neural estimation of restoring forces in nonlinear structures." *Journal of Applied Mechanics*, 68(6), 880-893.

Kristan, W. B., Calabrese, R. L., and Friesen, W. O. (2005). "Neuronal control of leech behavior." *Progress in Neurobiology*, 76(5), 279-327.

Kurata, M., Kim, J., Lynch, J. P., van der Linden, G. W., Sedarat, H., Thometz, E., Hipley, P., and Sheng, L.-H. (2013). "Internet-enabled wireless structural monitoring systems: development and permanent deployment at the New Carquinez suspension bridge." *Journal of Structural Engineering*, 139(10), 1688-1702.

Kurata, N., Spencer, B. F., Ruiz-Sandoval, M., Miyamoto, Y., and Sako, Y. (2003). "A study on building risk monitoring using wireless sensor network MICA-Mote." *Proc., First International Conference on Structural Health Monitoring and Intelligent Infrastructure,* Tokyo, Japan.

Le Cun, Y., Denker, J. S., and Solla, S. A. (1990). "Optimal brain damage." *Advances in neural information processing systems*, 2(1), 1990.

Lewis, F. L., and Syrmos, V. L. (1995). *Optimal Control*, Wiley, Hoboken, NJ.

Lewis, J. E., and Kristan, W. B. (1997). "A neuronal network for computing population vectors in the leech." *Nature*, 391, 76-79.

Loeb, G. E., and Ghez, C. (2000). "The motor unit and muscle action." *Principles of Neural Science*, E. R. Kandel, J. H. Schwartz, and T. M. Jessell, eds., McGraw-Hill, New York, NY.

Lynch, J. P. (2002). "Decentralization of wireless monitoring and control techniques for smart civil structures."Ph.D. dissertation, Stanford University, Stanford, CA.

Lynch, J. P. (2007). "An overview of wireless structural health monitoring for civil structures." *Philosophical Transactions of the Royal Society of London, Series A, Mathematical and Physical Sciences*, 365, 345-372.

Lynch, J. P., Law, K. H., Kiremidjian, A. S., Kenny, T. W., and Carryer, E. (2002). "A wireless modular monitoring system for civil structures." *Proc., Proceedings of the 20th International Modal Analysis Conference (IMAC XX)*, Los Angeles, CA.

Lynch, J. P., and Loh, K. J. (2006). "A summary review of wireless sensors and sensor networks for structural health monitoring." *The Shock and Vibration Digest*, 38(2), 91-128.

Lynch, J. P., Sundararajan, A., Law, K. H., Kiremidjian, A. S., and Carryer, E. (2004). "Embedding damage detection algorithms in a wireless sensing unit for operational power efficiency." *Smart Materials and Structures*, 13, 800-810.

Lynch, J. P., Sundararajan, A., Law, K. H., Kiremidjian, A. S., Kenny, T. W., and Carryer, E. (2003). "Embedment of structural monitoring algorithms in a wireless sensing unit." *Structural Engineering and Mechanics*, 15(3), 285-297.

Lynch, J. P., Wang, Y., Swartz, R. A., Lu, K.-C., and Loh, C.-H. (2008). "Implementation of a closed-loop structural control system using wireless sensor networks." *Journal of Structural Control and Health Monitoring*, 15(4), 518-539.

Lyon, R. F. "A computational model of filtering, detection, and compression in the cochlea." *Proc., IEEE International Conference on Acoustics, Speech, and Signal Processing*, Paris, France, 1282-1285.

Mallat, S. (1989). "A theory for multiresolution signal decomposition: the wavelet representation." *IEEE Transactions on Pattern Analysis and Machine Intelligence*, 11(7), 674-693.

Mallat, S. (2008). *A wavelet tour of signal processing: the sparse way*, Academic Press - Elsevier, Amsterdam, Holland.

Marin-Burgin, A., Kristan, W. B., and French, K. A. (2008). "From synapses to behavior: developement of a sensory-motor circuit in the leech." *Developmental Neurobiology*, 68(6), 779-787.

MathWorks. 2011. MATLAB, Version R2011b, Natick, MA.

McCulloch, W. S., and Pitts, W. (1943). "A logical calculus of the ideas immanent in nervous activity." *Bulletin of Mathematical Biophysics*, 5, 115-133.

Mead, C. (1990). "Neuromorphic electronic systems." *Proceedings of IEEE*, 78(10), 1629-1636.

Mehrotra, K., Mohan, C. K., and Ranka, S. (2000). *Elements of artificial neural networks*, The MIT Press, Cambridge, MA.

Menon, C., and Setti, M. (2006). "A biomimetic climbing robot based on the gecko." *Journal of Bionic Engineering*, 3(3), 115-125.

Minsky, M. (1961). "Steps toward artificial intelligence." *Proceedings of the Institute of Radio Engineers*, 49(1), 8-30.

Modha, D. S., Ananthanarayanan, R., Esser, S. K., Ndirango, A., Sherbondy, A. J., and Singh, R. (2011). "Cognitive computing." *Communications of the Association for Computing Machinery*, 54(8), 62-71.

Moore, M., Phares, B., Graybeal, B., Rolander, D., and Washer, G. (2001). "Reliability of visual inspection for highway bridges, volume I: final report." Report No. FHWA-RD-01-020, Federal Highway Administration, Washington D.C.

MTS Sensors (2012). "Temposonics: magnetostrictive, absolute, non-contact linear-position sensors." MTS Sensors, Eden Prairie, MN.

Nagayama, T., Spencer, B. F., and Rice, J. A. (2007). "Structural health monitoring utilizing Intel's Imote2 wireless sensor platform." *Proc., SPIE 6529: sensors and smart structures technologies for civil, mechanical, and aerospace systems*, San Diego, CA, 6592943.

Needell, D., and Tropp, J. A. (2009). "CoSaMP: Iterative signal recovery from incomplete and inaccurate samples." *Applied and Computational Harmonic Analysis*, 26(3), 301-321.

Nelson, R. (1962). "The link between science and invention: the case of the transistor." *The rate and direction of inventive activity: economic and social factors*, H. M. Groves, ed., National Bureau of Economic Research, Cambridge, MA.

Nicholls, J. G., Martin, A. R., Wallace, B. G., and Fuchs, P. A. (2001). *From neuron to brain*, Sinauer Associates, Incorporated, Sunderland, MA.

Nitta, Y., Nagayama, T., Spencer, B. F., and Nishitani, A. (2005). "Rapid damage assessment for the structures utilizing smart sensor MICA2 MOTE." *Proc., 5th International Workshop on Structural Health Monitoring*, Stanford, CA.

NTSB (2010). "Pipeline accident report: Pacific Gas and Electric Company pipeline rupture and fire." Report No. NTSB/PAR-11/01, National Transportation Safety Board, Washington D.C.

O'Connor, S., Lynch, J. P., and Gilbert, A. "A modal analysis application of compressed sensing for enhancing energy efficiency in wireless structural monitoring systems." *2012 Joint Conference of the Engineering Mechanics Institute and the 11th ASCE Joint Specialty Conference on Probabilistic Mechanics and Structural Reliability*, South Bend, IN.

Ohtori, Y., Christenson, R. E., Spencer, B. F., and Dyke, S. J. (2004). "Benchmark control problems for seismically excited nonlinear buildings." *Journal of Engineering Mechanics*, 130(4), 366-385.

Olson, E. S., and Mountain, D. C. (1991). "In vivo measurements of basilar membrane stiffness." *Journal of the Acoustical Society of America*, 89(3), 1262-1275.

Paik, B.-G., Cho, S.-R., Park, B.-J., Lee, D., Bae, B.-D., and Yun, J.-H. (2009). "Characteristics of wireless sensor network for full-scale ship application." *Journal of Marine Science and Technology*, 14(1), 115-126.

Pakzad, S. N., Fenves, G. L., Kim, S., and Culler, D. E. (2008). "Design and implementation of scalable wireless sensor network for structural monitoring." *Journal of Infrastructure Systems*, 14(1), 89-101.

Park, J. W., Cho, S., Jung, H.-J., Yun, C. B., Jang, S. A., Jo, H., Spencer, B. F., Nagayama, T., and Seo, J.-W. (2010). "Long-term structural health monitoring system of a cable-stayed bridge based on wireless smart sensor networks and energy harvesting techniques." *Proc., 5th World Conference on Structural Control and Monitoring*, Tokyo, Japan.

Peckens, C. A., and Lynch, J. P. "Cochlea-based signal decomposition and compression for structural monitoring applications." *2012 Joint Conference of the Engineering Mechanics Institute and the 11th ASCE Joint Specialty Conference on Probabilistic Mechanics and Structural Reliability*, South Bend, IN.

Peckens, C. A., and Lynch, J. P. (2013). "Utilizing the cochlea as a bio-inspired compressive sensing technique." *Smart Materials and Structures*, 22(105027).

Pei, J. S., Smyth, A. W., and Kosmatopoulos, E. B. (2004). "Analysis and modification of Volterra/Wiener neural networks for the adaptive identification of non-linear hysteretic dynamic systems." *Journal of Sound and Vibration*, 275(3-5), 693-718.

Pette, D., and Vrbova, G. (1985). "Invited review: neural control of phenotypic expression in mammalian muscle fibers." *Muscle and Nerve*, 8(8), 676-689.

Quanser "Linear motion servo plants: IP01 or IP02 user manual." <http://web.itu.edu.tr/~mutlui/IP01_2%20User%20Manual.pdf>. (January 7, 2014).

Raghavan, A., and Cesnik, C. E. S. (2007). "Review of guided-wave structural health monitoring." *The Shock and Vibration Digest*, 39(2), 91-114.

Reed, R. (1993). "Pruning alogrithms - a survey." *IEEE Transactions on Neural Networks*, 4(5), 740-747.

Reina, P. (2004). "Questions raised over steel roof struts–probe says steel tubes, not columns, are likely trigger for Paris airport's concourse collapse." *Engineering news record*, <http://enr.construction.com/news/buildings/archives/040712-1.asp>. (October 22, 2013).

Rice, J. A., Mechitov, K. A., Sim, S. H., Nagayama, T., Jang, S. A., Kim, R., Spencer, B. F., Agha, G., and Fujino, Y. (2010). "Flexible smart sensor framework for autonomous structural health monitoring." *Smart Structures and Systems*, 6(5-6), 423-438.

Rieke, F., Warland, D., de Ruyter van Steveninck, R., and Bialek, W. (1999). *Spikes: exploring the neural code*, The MIT Press, Cambridge, MA.

Robles, L., and Ruggero, M. A. (2001). "Mechanics of the mammalian cochlea." *Physiological Reviews*, 81(3), 1305-1352.

Rolfes, R., Zerbst, S., Haake, G., Reetz, J., and Lynch, J. P. (2007). "Integral SHM-system for offshore wind turbines using smart wireless sensors." *Proc., The 6th International Workshop on Structural Health Monitoring*, Stanford, CA.

Rosenblatt, F. (1962). *Principles of neurodynamics; perceptrons and the theory of brain mechanisms*, Spartan Books, Washington D.C.

Rumelhart, D. E., Hinton, G. E., and Williams, R. J. (1986). "Learning internal representations by error propagation." *Parallel distributed processing:*

explorations in the microstructure of cognition, D. E. Rumelhart, and J. L. McClellend, eds., MIT Press, Cambridge, MA, 318-362.

Sayood, K. (2006). *Introduction to data compression*, Morgan Kaufmann - Elsevier, San Francisco, CA.

Schultz, W., Dayan, P., and Montague, P. R. (1997). "A neural substrate of prediction and reward." *Science*, 275, 1593-1599.

Shapiro, J. (1993). "Embedded image coding using zerotrees of wavelet coefficients." *IEEE Transactions on Signal Processing*, 41(12), 3445-3462.

Sim, S. H., Spencer, B. F., Zhang, M., and Xie, H. (2010). "Automated decentralized modal analysis using smart sensors." *Structural Control and Health Monitoring*, 17(8), 872-894.

Sohn, H., Farrar, C. R., and Hemez, F. M. (2003). "A review of structural health monitoring literature 1996-2001." *Technical report annex to SAMCO summer acadamy*, Report No. LA-13976-MS, Los Alamos National Laboratory, Los Alamos, NM.

Song, S., Miller, K. D., and Abbott, L. F. (2000). "Competitive Hebbian learning through spike-timing-dependent synaptic plasticity." *Nature Neuroscience*, 3(9), 919-926.

Spanias, A. S., Jonsson, S. B., and Stearns, S. D. (1991). "Transform methods for seismic data compression." *IEEE Transactions on Geoscience and Remote Sensing*, 29(3), 407-416.

Spencer, B. F., Dyke, S. J., Sain, M. K., and Carlson, J. D. (1997). "Phenomenological model for magnetorheological dampers." *Journal of Engineering Mechanics*, 123(3), 230-238.

Spencer, B. F., and Nagarajaiah, S. (2003). "State of the art of structural control." *Journal of Structural Engineering*, 129(7), 845-856.

Spencer, B. F., Ruiz-Sandoval, M. E., and Kurata, N. (2004). "Smart sensing technology: opportunities and challenges." *Journal of Structural Control and Health Monitoring*, 11(4), 349-368.

Spencer, B. F., and Sain, M. K. (1997). "Controlling buildings: a new frontier in feedback." *IEEE Control Systems Magazine*, 17(6), 19-35.

Spencer , B. F., Suhardjo, J., and Sain, M. K. (1994). "Frequency domain optimal control strategies for aseismic protection." *Journal of Engineering Mechanics*, 120(1), 135-158.

Spencer, B. F., Yang, G., Carlson, J. D., and Sain, M. K. (1998). "Smart dampers for seismic protection of structures: a full-scale study." *Proc., Second World Conference on Structural Control*, Kyoto, Japan.

Straser, E., and Kiremidjian, A. S. (1998). "Modular, wireless damage monitoring system for structures." Report No. 128, John A. Blume Earthquake Engineering Center, Stanford, CA.

Straser, E. G., Kiremidjian, A. S., Meng, T. H., and Redlefsen, L. (1998). "Modular, wireless network platform for monitoring structures." *Proc., 16th International Modal Analysis Conference (IMAC)*, SEM, Santa Barbara, CA, 450-456.

Suhardjo, J., Spencer , B. F., and Kareem, A. (1992). "Frequency domain optimal control of wind-excited buildings." *Journal of Engineering Mechanics*, 118(12), 2463-2481.

Sun, Z., Li, B., Dyke, S., and Lu, C. (2012). "Evaluation of performance of structural control benchmark problem with time delays from wireless sensor network." *Proc., 2012 Joint Conference on Engineering Mechanics Institute and the 11th ASCE Joint Specialty Conference on Probabilistic Mechanics and Structural Reliability*, South Bend, IN.

Swartz, A., Lynch, J. P., Zerbst, S., Sweetman, B., and Rolfes, R. (2010). "Structural monitoring of wind turbines using wireless sensor networks." *Smart Structures and Systems*, 6(3), 183-196.

Swartz, A., Zimmerman, A. T., Lynch, J. P., Rosario, J., Brady, T., Salvino, L. W., and Law, K. H. (2012). "Hybrid wireless hull monitoring system for naval combat vessels." *Structure and Infrastructure Engineering*, 8(7), 621-638.

Swartz, R. A., Jung, D., Lynch, J. P., Wang, Y., Shi, D., and Flynn, M. P. (2005). "Design of a wireless sensor for scalable distributed in-network computation in a structural health monitoring system." *Proc., 5th International Workshop on Structural Health Monitoring*, Stanford, CA.

Swartz, R. A., and Lynch, J. P. (2009). "Strategic network utilization in a wireless structural control system for seismically excited structures." *Journal of Structural Engineering*, 135(5), 597-608.

Symans, M. D., and Constantinou, M. C. (1999). "Semi-active control systems for seismic protection of structures: a state-of-the-art review." *Engineering Structures*, 21(6), 469-487.

Texas Instruments (2007). "CC2520 2.4 GHz IEEE 802.15.4 / ZigBee-ready RF Transceiver." Texas Instruments, Inc., Dallas, TX.

Texas Instruments (2009). "CC2520EM reference design, rev. B." Texas Instruments, Inc., Dallas, TX.

Von Békésy, G. (1960). *Experiments in Hearing*, McGraw Hill, New York.

Walter, P. L. (2007). "The history of the accelerometer." *Sound and Vibration*, 40th Annual Issue, 84-92.

Wang, Y., Lynch, J., and Law, K. (2009). "Decentralized Hinf; controller design for large-scale civil structures." *Earthquake Engineering & Structural Dynamics*, 38(3), 377-401.

Wang, Y., Swartz, R. A., Lynch, J. P., Law, K. H., Lu, K.-C., and Loh, C.-H. (2007). "Decentralized civil structural control using real-time wireless sensing and embedded computing." *Smart Structures and Systems*, 3(3), 321-340.

Weiss, K. D., Carlson, J. D., and Nixon, D. A. (1994). "Viscoelastic properties of magneto- and electro-rheological fluids." *Journal of Intelligent Material Systems and Structures* 5(6), 772-775.

Welch, G., and Bishop, G. (1995). "An introduction to the Kalman filter." Report No. TR95-041, University of North Carolina, Chapel Hill, NC.

Werbos, P. (1974). "Beyond regression: new tools for prediction and analysis in the behavioral science." PhD dissertation, Harvard University, Cambridge, MA.

Whitley, D. (1994). "A genetic algorithm tutorial." *Statistics and Computing*, 4, 65-85.

Wolpert, D. M., and Ghahramani, Z. (2000). "Computational principles of movement neuroscience." *Nature Neuroscience*, 3, 1212-1217.

Wong, K. Y., Lau, C. K., and Flint, A. R. (2000). "Planning and implementation of the structural health monitoring systems for cable support bridges in Hong Kong."

Proc., SPIE 3995: Nondestructive evaluation of highways, utilities, and pipelines, Newport, CA, 266-275.

Xu, N., Rangwala, S., Chintalapudi, K., Ganesan, D., Broad, A., Govindan, R., and Estrin, D. (2004). "A wireless sensor network for structural monitoring." *Proc., SensSy '04 of 2nd International Conference on Embedded Embedded Networked Sensor Systems*, Baltimore, MD, 13-24.

Yang, J. N., Wu, J. C., Reinhorn, A. M., Riley, M., Schmitendorf, W. E., and Jabbari, F. (1996). "Experimental verifications of H-inf and sliding mode control for seismically excited buildings." *Journal of Structural Engineering*, 122(1), 69-75.

Yao, X., Song, Y., and Jiang, L. (2011). "Applications of bio-inspired special wettable surfaces." *Advanced Materials*, 23(6), 719-734.

Yates, G. K., Winter, I. M., and Robertson, D. (1990). "Basilar membrane nonlinearity determines auditory nerve rate-intensity functions and cochlear dynamic range." *Hearing Research*, 45(3), 203-219.

Yegnanarayana, B. (2004). *Artificial neural networks*, PHI Learning Pvt. Ltd., New Delhi, India.

Yost, W. A. (2007). *Fundamentals of hearing: an introduction*, Academic Press - Elsevier, San Diego, CA.

Zhang, Y., and Li, J. (2006). "Wavelet-based vibration sensor data compression technique for civil infrastructure condition monitoring." *Journal of Computing in Civil Engineering*, 20(6), 390-399.

Zhao, F., and Guibas, L. J. (2004). *Wireless sensor networks: an information processing approach*, Morgan Kaufmann Publishers, San Francisco, CA.

Zimmerman, A. T., and Lynch, J. P. (2009). "A parallel simulated annealing architecture for model updating in wireless sensor networks." *IEEE Sensors Journal*, 9(11), 1503-1510.

Zimmerman, A. T., Shiraishi, M., Swartz, R. A., and Lynch, J. P. (2008). "Automated modal parameter estimation by parallel processing within wireless monitoring systems." *ASCE Journal of Infrastructure Systems*, 14(1), 102-113.

Zweig, G., Lipes, R., and Pierce, J. R. (1976). "The cochlear compromise." *The Journal of Acoustical Society of America*, 59(4), 975-982.